University of Nevada, Reno

Laser Shock Processing Of Magnesium Alloys: Microstructure Evolution And Enhanced Mechanical Properties

A dissertation submitted in partial fulfillment of

the requirements for the degree of Doctor of

Philosophy in Mechanical Engineering

by

Bo Mao

Dr. Yiliang Liao/Thesis Advisor

May, 2020

N

We recommend that the dissertation
prepared under our supervision by

BO MAO

entitled

**Laser Shock Processing Of Magnesium Alloys: Microstructure
Evolution And Enhanced Mechanical Properties**

be accepted in partial fulfillment of the
requirements for the degree of

DOCTOR OF PHILOSOPHY

Yiliang Liao, Ph.D.,
Advisor

Bin Li, Ph.D.,
Committee Member

Pradeep L. Menezes, Ph.D.,
Committee Member

Guoping Xiong, Ph.D.,
Committee Member

Dhanesh Chandra, Ph.D.,
Graduate School Representative

David W. Zeh, Ph.D., Dean
Graduate School

May, 2020

Abstract

Laser shock peening (LSP) is an advanced laser-based surface processing technique which has been widely utilized to enhance the engineering performance of metallic materials. Among a variety of metallic materials, magnesium (Mg) and its alloys have attracted tremendous research interests due to their low density and high specific strength. However, the applications of Mg alloys is often restricted by their poor mechanical properties. Recently, LSP has been utilized to tailor the microstructure and crystallographic texture of Mg alloys for enhancing their surface hardness, wear resistance, corrosion resistance, fatigue durability, and stretch formability. Despite these promising experimental results of enhancing the engineering performance of Mg alloys by LSP, the fundamental processing-microstructure relationship has not been fully understood. Microstructure evolution of metallic materials during LSP is of great practically importance for the LSP process development and control for optimized mechanical performance. Moreover, the effectiveness and efficiency of LSP for enhancing the engineering performance of Mg alloys have not been fully explored, which is mainly due to a lack of fundamental understanding of the deformation mechanism of Mg alloys during LSP process. The complex deformation modes of Mg alloys render their microstructural and mechanical response to thermal-mechanical processing significantly different and complicated from their high symmetry counterparts, like steels and aluminum alloys with a cubic structure. Specific scientific knowledge gaps for the LSP processing of Mg alloy are: (1) how would the twinning behavior of Mg alloys subjected to LSP be different from

it is under quasi-static loading condition? (2) how do the activation and distribution of twins affect the mechanical properties of Mg alloys?

In this study, LSP experiments are conducted on a rolled AZ31b Mg alloy. The microstructure before and after laser processing are characterized. A focus is placed on understanding the deformation twinning mechanism. The effect of laser intensity on the twin volume fraction is investigated. The surface hardness as associated with the twin density is measured. The mechanism responsible for the formation of gradient twinning microstructure and the twinning-induced hardening effect are discussed. The anisotropic response to LSP in terms of microstructure and hardness improvement in Mg samples is discussed. Twin-twin interactions during LSP is examined and a non-dislocation based mechanism is proposed. Tribological testing and room temperature stretch-formability testing are carried out on the LSP processed Mg alloys to further explore the opportunities of using LSP for enhancing the mechanical properties.

Through this study, it has been found that: (1) Deformation twinning, in particular, the $\{10\bar{1}2\}\langle10\bar{1}\bar{1}\rangle$ tension twinning mode, plays a critical role during the LSP processing of Mg alloys. A gradient twinning microstructure in which the density of twins decreases with depth was introduced to an AZ31B Mg alloy plate by LSP. Gradient surface hardening effect was accompanied with the gradient twinning distribution. (2) Twin-twin interactions profusely exist in Mg alloys as processed by LSP. Interfaces between different tension twin variants shows that these interfaces present abnormal morphologies that cannot be accounted for by twinning dislocation theories. Patches of one variant can be completely surrounded by another variant. Such an abnormal behavior of twin-twin

interaction can only be explained by non-twinning-dislocation theories that fundamentally differ from the classical twinning theory. (3) The tribological performance of Mg alloys can be improved by LSP processing. Both the surface friction coefficient and wear rate decreases with the volume fraction of twins introduced by LSP. The improved tribo-performance of Mg alloys by LSP are attributed to the twinning-induced hardening effect, twin growth and saturation phenomenon, and twinning-induced surface crystallographic texture change during sliding.   (4) The room temperature-stretch formability of Mg alloys can be enhanced by LSP processing. A combination of texture weakening by extension twinning and grain refinement induced by LSP may account for the improved stretch formability of the Mg alloy.

Dedication

To my beloved family

Acknowledgements

At the moment this dissertation comes into final shape, I am looking back on my five years life at the University of Nevada-Reno and feeling so lucky to have so many great mentors and wonderful friends around. They stimulate my curiosity, refresh my mind, and inspire great ideas in my research. The completion of my dissertation is accompanied with invaluable help from them.

First of all, I would like to express my sincere gratitude, deepest respect and special thanks to my major professor, Dr. Yiliang Liao, for providing me the opportunity to conduct this research. His generous support, patient tutoring, and sustaining encouragement, make this dissertation possible and imprinted on my heart. In addition to being a creative and insightful researcher, Dr. Liao is also an excellent advisor and friend with whom I have shared so much joy of research.

My sincere thanks also go to Dr. Bin Li. I cannot forget the constructive discussion, insightful guidance, and every help that Dr. Li has provided me. His professional expertise and inspiring dedication impressed me and will benefit my future academic research. I would also like to thank Dr. Pradeep L Menzes for teaching me priceless knowledge in tribology and giving me invaluable suggestions on my research. My thanks also goes to Dr. Guoping Xiong and Dr. Dhanesh Chandra, for constant support and severing as my PhD committee members. I thank them for their valuable inputs and their good-natured support.

I would like to give my deepest thanks to Dr. Joel DesOrmeau for his kindness of supporting me on EBSD work. I am also grateful to Dr. Yufeng Zheng and Dr. Zac

Table of Contents

List of Tables

List of Figures

Chapter 1. Introduction

1.1. Laser shock peening

Laser shock peening (LSP) is an advanced laser-based surface engineering process that utilizes high energy laser pulses with a duration of nanoseconds or femtoseconds to improve the engineering performance of metallic materials [1-3]. It was firstly developed in 1972 by Fairand et al. [4] who utilized a laser induced shockwave to improve the mechanical properties of 7075 aluminum alloys. Later on, LSP was applied to improve the fatigue strength of turbine engine blade of military aircraft [5, 6]. With the advances of laser technology and theory of laser materials interaction, novel LSP technologies such as warm LSP and thermal engineering LSP were developed in recent years [7, 8]. Compared with other surface strengthening treatment technologies, such as shot peening [9] or deep rolling [10], LSP holds several advantages such as excellent controllability, high flexibility, and good uniformity with no heat affected zone [11]. LSP also stands out due to its capability to introduce greater depth and higher magnitude of compressive residual stress with good controllability and significant strengthening effect [12]. Therefore, LSP has been widely used to enhance the fatigue durability [13], wear resistance [3], corrosion resistance [2], and other mechanical properties of metallic materials in aerospace, military, and bio-medical applications.

1.2. Magnesium alloys

Magnesium (Mg) and its alloys are the lightest structural metallic materials, with a density of 1.74g/cm^3 which is only 22% as that of steels (7.87g/cm^3) and 64% of aluminum

(2.7g/cm^3) [14]. It is abundant in earth's crust (2.7% in mass percentage) and can be extracted from sea water [15]. Magnesium alloys possess some superior physical and mechanical properties such as high strength-to-weight ratio [16], good recyclability [17], excellent thermal conductivity[18], and desirable bio-compatibility [19]. All of these characteristics make magnesium and its alloys very promising in the applications of aircraft [20], automotive [21], bio-implants [22], and electronic devices [23].

Although Mg and its alloys offer significant potential for a variety of applications, they have not been widely utilized due to their undesirable mechanical properties. Unlike most engineering materials such as steels and aluminum alloys which have a cubic crystal structures, magnesium and it alloys have a hexagonal close-packed (HCP) structure with only two "easy" independent plastic deformation modes, $\{0001\}\langle11\bar{2}0\rangle$ basal slip and $\{10\bar{1}2\}\langle10\bar{1}\bar{1}\rangle$ tension twin deformation twinning, in ambient condition. Other slip systems such as prismatic slip and pyramidal slip which have the same slip direction in common but much larger critical resolved shear stress (CRSS) might be activated in high temperature [24]. Moreover, a strong basal texture in which most grains have their c-axes along the normal direction of rolled plates is often developed during the thermomechanical treatment process [25, 26]. Therefore, pyramidal $\langle c + a \rangle$ dislocations need to be activated to accommodate the plastic stain along crystallographic c direction. While several studies showed that pyramidal $\langle c + a \rangle$ has a much higher CRSS than basal slip and requires substantial thermal energy to be activated [27-29].

Deformation twinning is usually activated to maintain the compatibility of plastic deformation of magnesium alloys, especially the $\{10\bar{1}2\}\langle10\bar{1}\bar{1}\rangle$ tension twin and

$\{10\bar{1}1\}\langle10\bar{1}2\rangle$ contraction twin [30-32]. $\{10\bar{1}2\}\langle10\bar{1}\bar{1}\rangle$ tension twin is the most prevalent twinning mode in Mg alloys due to its low CRSS and invasive growth capability [33, 34]. It can be easily activated when a tensile load is applied to a Mg crystal along the [0002] direction [35]. $\{10\bar{1}1\}\langle10\bar{1}\bar{2}\rangle$ contraction twin, on the contrary, can be activated to accommodate the compression strain along [0002] direction with a much higher CRSS [36]. $\{10\bar{1}2\} - \{10\bar{1}1\}$ double twin (DTW), corresponding to the secondary $\{10\bar{1}2\}$ twinning within the primary $\{10\bar{1}1\}$ twins are sometimes observed and correlated with the onset of stress localization and fracture in Mg alloys [37].

The particular crystallographic characteristics and complex deformation modes endow Mg alloys some unique mechanical performances, such as anisotropic plastic hardening [38], low ductility [27], low yield strength [39], and tension-compression yielding asymmetry [40]. Therefore, their applications are restricted by their limited ductility, poor formability and low wear resistance at room temperature [21, 41]. However, the compelling need for lightweight, environmentally friendly, and energy-efficient materials continue to drive the research and development of Mg alloys that address the issue of strength, durability, and formability.

1.3. Significance and Motivation

Various metallurgical strategies including thermomechanical processing and alloying have been developed to enhance the engineering performance of Mg alloys [42-44], with particular focus on improving their ductility, formability, fatigue educability and tribological properties. These methods include micro-alloying [45], equal-channel angular processing (ECAP) [46], and surface mechanical attrition treatment (SMAT) [47]. For

instance, Amanov et al. [48] utilized an ultrasonic nanocrystalline surface modification method to process an AZ91D Mg alloy and showed that the surface wear rate and friction coefficient were reduced by about 23% and 30% respectively compared with the untreated samples. Homma et al. [49] showed that the strength of an Mg-1.8Gd-1.8Y-0.7Zn-0.2Zr alloy could reach to 542 MPa with an hot extrusion process followed by aging. Chen al. [50] carried out multi-pass rolling method to process a ZK61 Mg alloy and demonstrated the total elongation can be increased to 35% without sacrificing the strength.

In addition to these processing approaches, LSP is exceptional due to its high process efficiency, flexibility, and controllability [51, 52]. LSP is a surface processing process utilizing pulsed laser energy to introduce compressive residual stresses and a work-hardened layer to the surfaces of metallic materials for enhanced durability [11, 53]. Recent studies indicate that LSP is promising to improve the engineering performance of Mg alloys by enhancing their surface strength [54], biocompatibility [55], fatigue resistance [56], and anti-corrosion ability [57]. For instance, Ye et al. [54] showed that LSP resulted in the increase of surface hardness of AZ31B Mg alloy from 57 to 69 HV and the yield strength from 128 to 152 MPa. Vinodh [55] et al. reported that the corrosion rate of the Mg–calcium (Mg-Ca) alloy samples without laser processing was 2.5 times higher than that of the samples processed by LSP. In addition, laser processed samples exhibited a significantly improved biocompatibility. Ge et al. [58] investigated the effect of LSP on the stress corrosion cracking behavior of AZ31B Mg alloy and showed that the SCC susceptibility index of the LSP treated samples was decreased by 47.5% as compared to the as-received samples. Sealy et al. [59] studied the fatigue performance of Mg-Ca alloys

subjected to LSP and found that the rotating bending fatigue life of the laser peened samples was ten times higher than that of the untreated samples.

However, the effectiveness and efficiency of LSP for enhancing the engineering performance of Mg alloys have not been fully explored. This is attributed to the lack of in-depth understanding of microstructure evolution behaviors, particularly deformation twinning mechanism, of Mg alloys subjected to LSP processing. Mg alloys have a low symmetry HCP crystal structure and possess enormous deformation mechanisms, including dislocation slip and deformation twinning. The complex deformation modes render their microstructural and mechanical response to thermal-mechanical processing significantly different and complicated from their high symmetry counterparts, like steels and aluminum alloys with a cubic structure [60, 61]. Specific scientific knowledge gaps for the LSP processing of Mg alloy are: (1) how would the twinning behavior of Mg alloys subjected to LSP be different from it is under quasi-static loading condition? (2) how do the activation and distribution of twins affect the mechanical properties of Mg alloys?

Moreover, current challenges for the applications of Mg alloys offer an opportunity to explore the applicability of LSP to enhance the mechanical properties of Mg alloys, such as strength, wear resistance, and formability. The technology gaps for LSP processing of Mg alloy are: (1) could we extend the applications of LSP of Mg alloys to solve the bottlenecks that limited the performance of Mg alloys? (2) How to design and optimize the LSP processing parameters to enhance the mechanical properties of Mg alloys?

1.4. Research objectives and outlines

With the research motivation discussed above, the current research aims to investigate the microstructure evolution of Mg alloys during LSP process and therefore enhance the mechanical properties of Mg alloys by LSP. The following main objectives have been focused on and achieved throughout the course of this dissertation:

(1) The investigation of microstructure evolution of Mg alloys during LSP process. Emphases are place on the deformation twinning behavior, twin-twin interactions, and dynamic recrystallization in the LSP process.

(2) The study of anisotropic microstructural and mechanical response of magnesium alloys to LSP. The shock response behavior of Mg alloys in different loading directions will be studied.

(3) The analysis of the mechanism responsible for the enhanced mechanical properties, such as hardness, wear resistance and formability of Mg alloys processed by LSP. The relationship of processing parameters-microstructure-mechanical properties will be established.

To achieve these goals, research efforts will be put in three interrelated parts: LSP processing, microscopic characterization and mechanical properties testing. LSP experiments will be conducted first, with optimal processing parameters such as laser intensity, beam size, and overlapping ratio. The microstructure evolution as affected by these parameters will be characterized by optical microcopy (OM), 3-D surface profilometer, scanning electron microscopy (SEM), and electron backscattered diffraction (EBSD) techniques. To investigate the mechanical properties of Mg alloys processed by

LSP, surface micro-hardness tests, tribological test, as well as stretch formability test will be carried out. With detailed microstructural analysis and mechanical properties evaluation, the mechanism responsible for the microstructure evolution and mechanical properties enhancement of Mg alloys processed by LSP will be enlighten.

According to the research objectives and outline listed above, the current study will contribute to the following intellectual merits and broaden impacts to the research and development of Mg alloys for better industrial applications.

(1) Understand the effect of LSP process on Mg alloys in terms of the relationship among the process, property and microstructure.

(2) Understand the ultra-high-strain rate (10^5-10^7/s) deformation behavior of Mg alloys, with focus on the twinning mechanism, twin-twin interactions, dynamic recrystallization process, and plastic anisotropy behavior.

(3) Develop a novel surface approach with optimized processing parameters for enhancing mechanical properties, such as, surface hardness, wear resistance, and stretch formability of Mg alloys.

Chapter 2. Literature review

2.1. LSP

2.1.1. Mechanism of LSP

A schematic illustration of LSP process is shown in Figure 2.1. During LSP process, the target is typically covered by an ablative coating and a transparent confinement layer. As the laser pulse passes through the confinement and interacts with the ablative coating, the ablative coating the ablative coating layer is quickly evaporated and ionized by laser-matter interaction, leading to the formation of laser-induced plasma [62]. The hydrodynamic expansion of plasma is restricted by the transparent confinement, generating a shockwave with a high peak pressure (on the order of GPa). The laser-induced shockwave propagates into the target. When the pressure of the shockwave exceeds the dynamic yield strength of the target material, plastic deformation with an ultra-high strain rate ($10^5 \sim 10^6$/s) is induced in the near surface [63, 64].
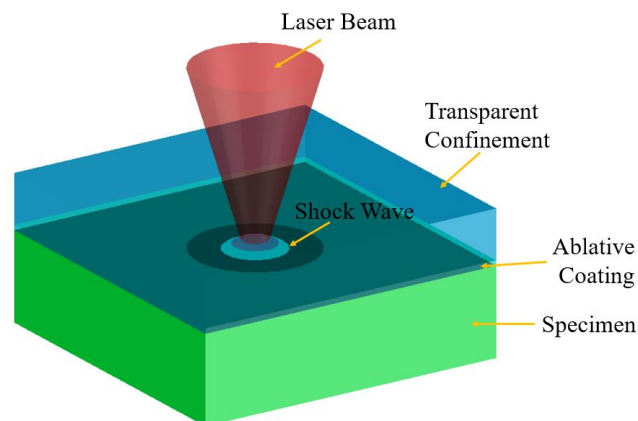
Figure 2.1. Schematic illustration of the LSP configuration.

2.1.2. Effects of LSP on the microstructure evolution of metallic materials

Microstructure evolution of metallic materials during LSP is of great practical importance for the LSP process development and control for optimized mechanical performance [53]. The formation or activities of dislocations [60, 61], shear bands [65, 66], phase transformation [67, 68] and surface nanocrystallization [69, 70] of several commonly used metallic materials processed by LSP have been extensively studied. In particular, LSP can bring a significant grain refinement effect on the surface of processed materials. It is typically assumed that this grain refinement effect is highly related to the dislocation activities during the high-strain-rate deformation process induced by LSP [61, 70]. For instance, Trdan et al. [66] showed that a layer with ultra-fine (60-200 nm) grains were produced in an Al-Mg-Si alloy by LSP. They attributed the grain refinement effect to the exceptional increase of dislocation density by ultra-high strain rate plastic deformation induced by LSP. The grain refinement in AISI 304 stainless steels and LY2 aluminum alloys processed by LSP has been studied by Lu et al. [69, 71]. They proposed that dislocation walls and dislocation tangles were produced on the top surface layer of processed materials during LSP. The original grains were divided into subgrains by these dislocations and then turned into refined grains through dynamic recrystallization.

2.1.3. Effects of LSP on the mechanical properties of metallic materials

LSP can effectively improve the mechanical properties such as surface hardness, fatigue limit, stress corrosion resistance, and wear resistance of most metallic materials due to the surface plastic deformation and compressive residual stress introduced in this process. It is generally accepted that LSP can bring a strengthening effect and a compressive residual

stress to the surface of metallic materials. A variety of studies have been carried out to investigate the effects of LSP on the mechanical properties of materials. For instance, Zhang et al. [72] showed that the fatigue life of a LY2 aluminum alloy can be improved from 12000 cycles for the untreated samples to 26000 cycles for the samples processed by LSP. Sanchez-Santana et al. [3] reported that the wear resistance of an AA6061 aluminum alloys can be enhanced by 2-3 times with the LSP processing. Lu et al. [73] demonstrated that the nano-hardness of a Fe-Ni alloy can be improved from 1.99 GPa to 2.41 GPa after LSP process.

2.2. Mg alloys and their mechanical behavior

2.2.1. Plastic deformation modes in Mg
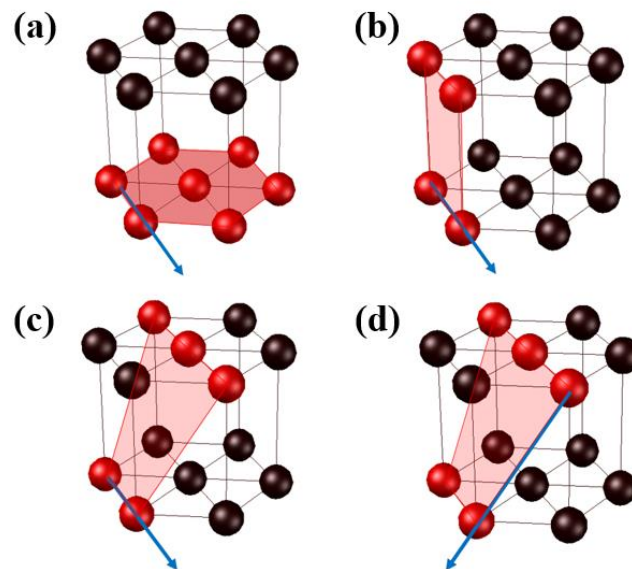
Figure 2.2. Slip modes in Mg and its alloys. (a) Basal slip, (b) prismatic slip, (c) pyramidal slip along $\langle a \rangle$, and (d) pyramidal slip along $\langle c + a \rangle$.

A number of experimental observations and numerical works have been carried out to obtain information regarding the activated slip system in Mg and its alloys [28, 74-76]. Generally, slip modes in Mg and its alloys include the $\{0001\}\langle11\bar{2}0\rangle$ basal slip, $\{10\bar{1}0\}\langle11\bar{2}0\rangle$ prismatic slip, $\{10\bar{1}1\}\langle11\bar{2}0\rangle$ pyramidal slip, and $\{10\bar{1}1\}\langle11\bar{2}3\rangle$ second order-pyramidal slip systems. The crystallographic schematics and the CRSS in room temperature of each slip system are shown in Figure 2.2 and summarized in Table 1.

Table 1. Slip systems in Mg alloys.

Slip system	Slip plane	Slip direction	Number of independent slip systems	CRSS at room temperature	Reference
Basal slip	$\{0001\}$	$\langle11\bar{2}0\rangle$	2	1.07	[77]
Prismatic slip	$\{10\bar{1}0\}$	$\langle11\bar{2}0\rangle$	2	8	[78]
Pyramidal slip along $\langle a \rangle$	$\{10\bar{1}1\}$	$\langle11\bar{2}0\rangle$	4	0.51	[79]
Pyramidal slip along $\langle c + a \rangle$	$\{10\bar{1}1\}$	$\langle11\bar{2}3\rangle$	5	40	[80]

In addition to dislocation slip, magnesium exhibits a strong propensity for deformation twinning, especially the $\{10\bar{1}2\}\langle10\bar{1}\bar{1}\rangle$ tension twin and $\{10\bar{1}1\}\langle10\bar{1}\bar{2}\rangle$ contraction twin. Tension twins and compression twins are typically activated to accommodate extension and compression strain along $\langle c \rangle$ axis, respectively. According to the classical twinning

theory, deformation twin was defined as "a region of a crystalline body which has undergoes a homogenous shape deformation in such a way that the crystal of the resulting product is identical with that of the parent, but oriented differently" [81]. Therefore, the boundary plane, also known as the twinning plane, must remain invariant during twinning. In deformation twinning, the crystallographic relationship between the parent and twin lattice can be described by a set of four parameters, $\{K_1, K_2, \eta_1, \eta_2\}$, where K_1 refers to the invariant plane of the shear, η_1 is the shear direction, and K_2, represents the conjugate twinning plane and η_2 conjugate twinning direction, respectively. The twinning elements as well as their CRSS for tension twin and contraction twin are listed in Table 2.
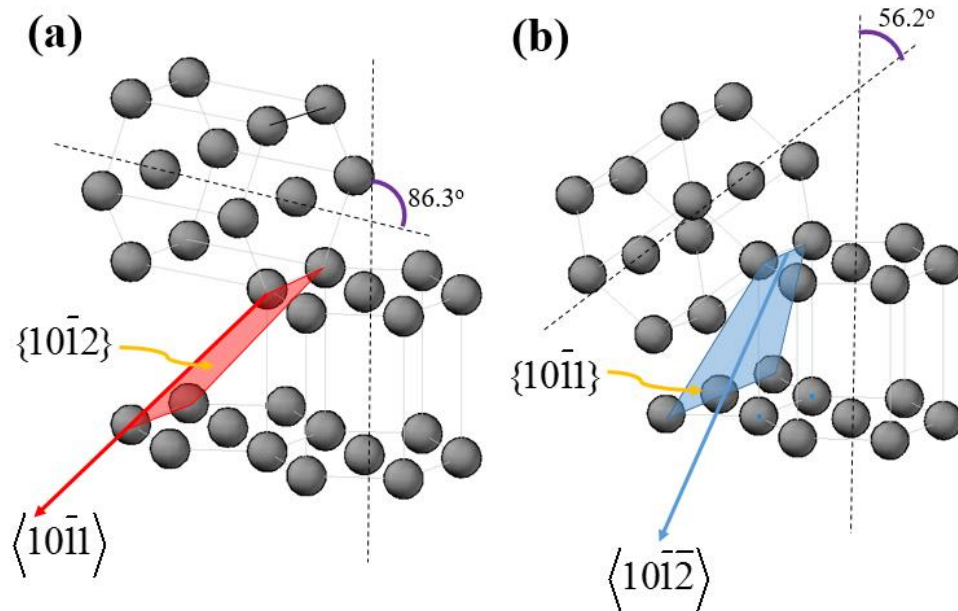
Figure 2.3 Twinning modes in Mg alloys: (a) $\{10\bar{1}2\}\langle10\bar{1}\bar{1}\rangle$ tension twin and (b) $\{10\bar{1}1\}\langle10\bar{1}\bar{2}\rangle$ contraction twin.

Table 2. Twinning elements and CRSS values for tension twin and compression twin.

Twinning mode	K_1	η_1	K_2	η_2	Twinning shear	CRSS (MPa)	Reference
Tension twinning	$\{10\bar{1}2\}$	$\langle\bar{1}011\rangle$	$\{10\bar{1}\bar{2}\}$	$\langle10\bar{1}1\rangle$	0.129	1.71	[82]
Contraction twinning	$\{10\bar{1}1\}$	$\langle10\bar{1}\bar{2}\rangle$	$\{10\bar{1}\bar{3}\}$	$\langle303\bar{2}\rangle$	0.138	110	[74]

$\{10\bar{1}2\}\langle10\bar{1}1\rangle$ tension twin is the most commonly observed deformation twinning mode in Mg alloys and therefore has received much more attention than others. According to the classical twinning theory, it is assumed that a finite twinning shear is involved and twinning dislocations are needed in mediating the twin boundary migration [30]. Since the interplanar spacing of $\{10\bar{1}2\}$ plane is 0.19 nm and the magnitude of twinning shear is around 0.129, the Burgers vector of a hypothesized "elementary twinning dislocation" is only 0.025 nm, which only of 1/31 of the lattice vector of the $\langle10\bar{1}1\rangle$ direction. As a result, the growth of twin boundary may need a "zonal dislocation" instead of any partial dislocations [83]. However, numerous experimental observations show that $\{10\bar{1}2\}\langle10\bar{1}1\rangle$ twinning mode exhibit some unique features which cannot be explained by the classical twinning theory. These unique features include extremely incoherent twin boundary [84], large deviation of twinning plane to the twin boundary [85], negligible twin-

precipitates interaction [86], non-Schmid behavior [87], and twinning-detwinning phenomenon [88].

In recent years, Li and Ma proposed that $\{10\bar{1}2\}\langle10\bar{1}1\rangle$ twinning mode is accommodated by pure atomic shuffling [89]. In their model, the lattice conversion between twin and parent is accomplished by atomic shuffling that converts the basal planes of parent to the prismatic planes of twin, and the prismatic planes of the parent to the basal planes of the twin. As shown in Fig. 3, the parent and twin are shown in red and blue lattice, respectively. The shaded $\{10\bar{1}2\}$ plane is shared by the parent and the distorted twin lattice. A homogeneous shear cannot occurs on the $\{10\bar{1}2\}$ plane and atomic shuffling is needed to accomplish the lattice transformation. Since shuffling alone is sufficient to accomplish the lattice transformation, the twinning shear cannot be any finite value but zero [90].
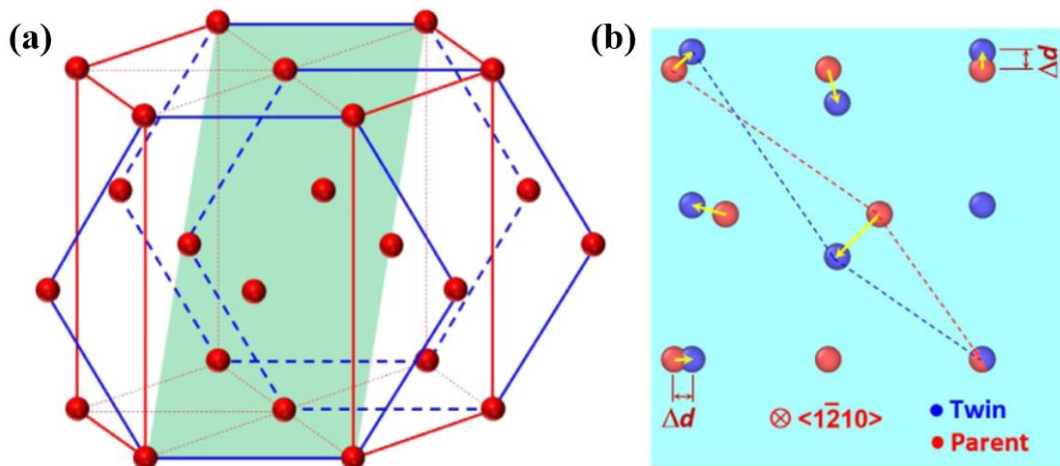
Figure 2.4. Lattice correspondence showing the crystallographic relationship between parent and twins according to Li and Ma's deformation twinning theory. (a) 3-D analysis of the lattice transformation and (b) shuffles in projection view along the $\langle1\bar{2}10\rangle$ zone axis. Adapted with permission from [90].

2.2.2. Mechanical properties of Mg alloys

Plastic anisotropy

It has been widely accepted that metallic materials with a HCP crystal structure exhibit a strong plastic anisotropy [91, 92]. Plastic anisotropy is an intrinsic property of Mg and its alloys and rooted from their HCP crystal structure which has a low symmetry [79]. In lattice scale, the CRSS for basal slip is much lower than $\langle c + a \rangle$ slip [27]. In bulk scale, Mg and its alloys often develop a strong basal texture in which most of grains are oriented such that their basal planes are perpendicular to the normal direction (ND) [93]. These characteristics give rise to their directional dependence of mechanical properties.

Plastic anisotropy has been a long standing issue in the research and applications of Mg alloys. Recent studies show that the plastic anisotropy has a significant impact on their monotonic tension [26, 94] and compression response [92, 95], fatigue endurance [96-98], tribological performance [99, 100], and processing behavior, like drawing and rolling [101]. For instance, Park et al. [95] reported that the magnitude of stress of an extrude AZ31 Mg alloys during monotonic compression tests along ND are 1.7 times higher than it is along RD at a strain of 0.04. Xiong et al. [102] showed that an AZ80 Mg alloy exhibit lowest fatigue resistance when the cyclic loading is applied along ND at a given strain amplitude. Guo et al. [103] measured the stress-strain curves of an rolled AZ31B Mg alloy for different tilt angles between ND and loading direction (LD) under uniaxial compression. The result is shown in Figure 2.3. It is found that the Mg alloys behave a very pronounced orientation-dependence of deformation behavior. When the compressive loading is along ND, the stress-strain curve exhibit a typical slip dominated plastic deformation. While the

compressive loading is along TD, the flow curve is characterized by a S-shape, indicating the role of twinning during the plastic deformation process. As the angle between the LD and ND increases from 0° to 90°, the deformation process change from a mode where twinning is negligible to a case dominated by twinning.
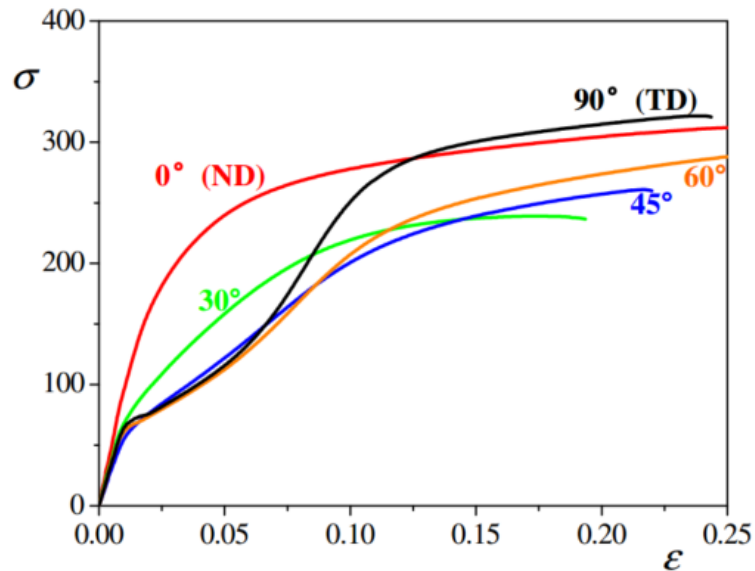
Figure 2.4 Stress-strain curves under uniaxial compression for different tilt angles between ND and LD, adapted with permission from [103].

Friction and wear behavior

In many applications, such as pistons, valves, bearing, sliding seals and gears, Mg alloys are subjected to sliding motion that can cause severe wear problem [104, 105]. Moreover, sliding wear is an important consideration in the forming process of Mg alloys, such as rolling, extrusion and forging [106]. Recent studies show that Mg and its alloys often exhibit very poor wear resistance. Therefore, understanding and improving the tribological properties of Mg alloys is of critical importance for expanding their applications.

Several strategies have been developed to improve the tribological performance of Mg alloys, either by fabricating a hard surface coating or introducing a nano-crystallization surface layer. For instance, Yu et al. [107] utilized a plasma electrolytic oxidation method to fabricate SiC based coatings on the surface of an AZ31 Mg alloy. The wear rates of the coated Mg alloy samples were reduced by 75% as compared with the untreated ones. Wang et al. [108] developed a laser cladding approach to fabricate Al-Si coatings on the surface of an AZ91 Mg alloy. The results showed that the wear rate can be significantly decreased by laser cladding. Sun et al. [109] carried out a surface mechanical attrition treatment on an AZ91D Mg alloy and found that the coefficient of friction (COF) of the processed samples can be reduced by 15% with the presence of nano-grains.

Stretch formability

It is widely accepted that Mg alloys exhibit very poor formability in ambient conditions [110]. The poor room temperature formability of Mg alloys has been a long standing issue in the applications and research of Mg alloys [43]. It is widely accepted that this drawback is associated with their HCP structure which possesses insufficient independent slip systems, together with their strong basal texture with most basal planes aligned perpendicular to the normal direction (ND) [27]. Several strategies have been developed to enhance the room-temperature formability of Mg alloys, either through alloying or processing. The addition of rare earth (RE) alloying elements, such as Ce [111] , Gd [112], Y [113], and Ca [114], has been proved to be efficient in improving the formability [115, 116]. However, the addition of rare earth elements renders the Mg alloys expensive and incompatible with recycling constraints [117]. On the other hand, processing-oriented

options, such as pre-compression [118], high temperature rolling [119], differential speed rolling [120], electo-plastic differential speed rolling [121], cross-wavy bending [122], and equal channel angular processing [123], provide effective alternatives with advantages of bulk processing, high controllability, and large scale manufacturing. From a metallurgical perspective, the formability of Mg alloys can be improved either by basal texture weakening or grain refinement. A weakened basal texture allows more homogeneous plastic deformation and refined grains promotes grain boundary sliding (GBS) which provides additional deformation mode [124, 125].

2.2.3. Dynamic recrystallization in Mg alloys

Due to their due to their poor formability at ambient environment, metallurgical processing of Mg and its alloys such as rolling, extrusion, and sheet forming are typically performed at elevated temperature [42]. Dynamic recrystallization (DRX) plays an important role during the hot processing of Mg alloys and significantly affect their microstructure and mechanical behavior, such as grain size [126], texture evolution [127], plasticity [128] and brittle-ductile transition [129].

Recent studies showed that the DRX can be exploited to refine the grain size and weaken the texture of Mg alloys and therefore enhance the mechanical properties of Mg alloys [128, 130-132]. For instance, Mohri et al. [128] showed that a rolled AZ91 Mg alloy could deform to a elongation of 604% at a temperature of 573K and strain rate of $1.5\times10^{-3}\,/\,s$ through DRX which resulted in a fine grain structure. Fatemi-Varzaneh et al. [133] reported that the average grain size of an AZ31 Mg alloy can be reduced from 7 μm to 2 μm by accumulative back extrusion (ABE) process. The DRX fraction increases while the

grain size decreases with the increasing number of ABE passes. Zhu et al. [134] carried out research on the microstructure evolution of ZK60 Mg alloys in the high strain-rate ($50/s$) rolling process, the results showed that an enhanced DRX behavior occurred with increased strain rate and resulted in an weakened texture and improved mechanical properties.

Due to its scientific importance, extensive investigations have been carried out to study the mechanism of DRX of Mg and its alloy. To date, three DRX mechanisms have been proposed. They are : (1) continuous DRX (CDRX), where new grains gradually form from the low-angle grain boundaries without nucleation [135, 136]; (2) discontinuous DRX (DDRX) [137], which involves the nucleation and growth of the new grains; and (3) twinning induced DRX (TDRX) [138], which new grains occur in twins and twin-twin boundaries. Moreover, the relationship between the DRX behavior with temperature [139, 140], grain size [141, 142], and initial texture [93, 143] of Mg alloys have been experimentally and numerically studied.

Chapter 3. Characterization and testing techniques

3.1. Microstructure characterization

3.1.1. Optical and scanning electron microcopy

The microstructure of Mg alloys processed before and after LSP are characterized using Leica DM2700 optical microscopy (OM), JEOL-7100FT field emission scanning electron microscope (FESEM). Samples for OM and FESEM characterization were prepared by sectioning, mounting, polishing, and chemical etching. The solution used for etching was a mixed acetic picral solution (10 ml acetic acid + 4.2 g picric acid + 10 ml distilled water + 70 ml ethanol). The well-polished samples were immersed into the solution for 10 seconds and then washed by ethanol and dried by a heater fan [144].

3.1.2. Electron backscattered diffraction

Electron Backscatter Diffraction (EBSD) is a SEM-based technique that gives crystallographic information about the microstructure of a sample. In EBSD, a stationary electron beam interacts with a tilted crystalline sample and the diffracted electrons form a pattern that can be detected with a fluorescent screen. In this study, EBSD analysis was carried out to investigate microstructure and crystallographic texture evolution. EBSD characterization was performed at an operating voltage of 25 kV, a working distance of 25 mm and a sample tilt angle of 70°. The data acquisition was performed with Channel 5 software with a different step size ranging from 0.1-3.0 μm.

3.2. Mechanical property testing

3.2.1. Hardness test

The surface micro-hardness of Mg alloys before and after laser processing were measured using a Wilson Hardness tester with a 500 g load and 10 s holding time. To get the in-depth hardness distribution, an electrolytic polisher was used to remove the material layer by layer for in-depth hardness testing. At each depth, the hardness values were measured 5 times.

3.2.2. Tribological test

The tribological properties, such as friction, and transfer layer formation of Mg alloys were investigated using a scratch test. The scratch tests were performed as per ASTM G133 on the samples. The scratch tests were performed using an Rtec multi-function tribometer 5000 which is equipped with a high-resolution 1D normal force load cell (15 mN resolution) and a 1D friction force load cell (6 mN resolution). Before each test, the pin and sample surface were thoroughly cleaned in an aqueous soap solution followed by ultrasonic cleaning in acetone. The repeatability and consistency of the results was verified by performing each scratch test three times.

3.2.3. Tensile test

To investigate the effect of LSP on the mechanical properties of Mg alloys, tensile tests were carried out using the "dog-bone" samples with a gauge area of 16 mm (RD) by 6 mm (TD) and a thickness of 2 mm (ND) machined from the Mg block. The strain rates were set as 0.0005/s in the tensile tests.

3.2.4. Stretch formability test

The room-temperature stretch formability of the Mg alloys are evaluated by the Erichsen tests. An Instron testing machine was used to control the forming speed and record the load vs. displacement behavior. The forming load was applied on a hemispherical shape punch with a diameter of 10 mm at a constant speed of 0.01 mm/s. The movement of the punch stopped as cracks initiated (indicated by a 10% drop of the maximum load) on the lower surface of the sample. The values of limit dome height (LDH), i.e., stretch formability, defined as the depth of the punch at fracture initiation, were then measured.

Chapter 4. Gradient twinning microstructure generated by LSP in Mg alloys

4.1. Introduction

Despite extensive experimental efforts has been put on understanding the effect of LSP on enhancing performance of Mg alloys, little attention has been paid to study the surface microstructure evolution during LSP. Although surface grain refinement of Mg alloys during LSP was reported in [145, 146], no particular investigation has been focused on elucidating the formation of high density deformation twins as a result of surface plastic deformation with an ultrahigh strain rate of $10^6 \sim 10^7$/s in the LSP process. Deformation twinning in HCP structure plays a fundamental role in enhancing mechanical performance of Mg alloys [30, 147]. In addition, the microstructural anisotropic response to LSP should be considered. A better understanding of twining mechanisms in Mg alloys as subjected to LSP may lead to improved process development and control for optimized mechanical performance.

This chapter is to establish the process-microstructure relationship of Mg alloys as processed by LSP. A focus is placed on understanding deformation twinning mechanism. LSP experiments are conducted on a rolled AZ31b Mg alloy. The microstructures before and after laser processing are characterized using optical microscopy, EBSD, and SEM. The effect of laser intensity on the twin volume fraction is investigated. The surface hardness as associated with the twin density is measured. The mechanisms responsible for the formation of gradient twinning microstructures and the twinning-induced strain hardening effect are discussed. The anisotropic response to LSP in terms of microstructure

and hardness improvement in Mg samples are compared and discussed. Notably, this part of content is basically adapted from [148] (with permission from publisher).

4.2. Experiments

Rolled AZ31B Mg alloy block (3.0 wt% Al, 1.0 wt% Zn, Mg balance) purchased from Metalmart.com was used for experiments. Cubic samples with a dimension of 1 inch by 1 inch were machined from the block for LSP processing. Prior to laser processing, the samples were grinded using SiC sandpapers with different grit numbers (from 320 to 1200), followed by fine polishing using 3 micron diamond suspension. Afterwards, the samples were ultrasonically cleaned in an ethanol solution.

Figure 4.1a shows a schematic view of the LSP configuration. In this work, a Q-switched Nd-YAG laser (Surelite III from Continuum, Inc.), operating at a wavelength of 1064 nm and a pulse width of 5 ns (full width at half maximum), was used to deliver the laser energy. The laser beam diameter was 2 mm. The laser power intensity was adjusted by adjusting the Q-switched delay time. Black tape with a thickness of 100 μm was used as the ablative coating material. BK7 glass with a high shock impedance was used as the transparent confinement. LSP experiments were performed along the rolling direction (RD) of the specimen (Figure 4.1b).
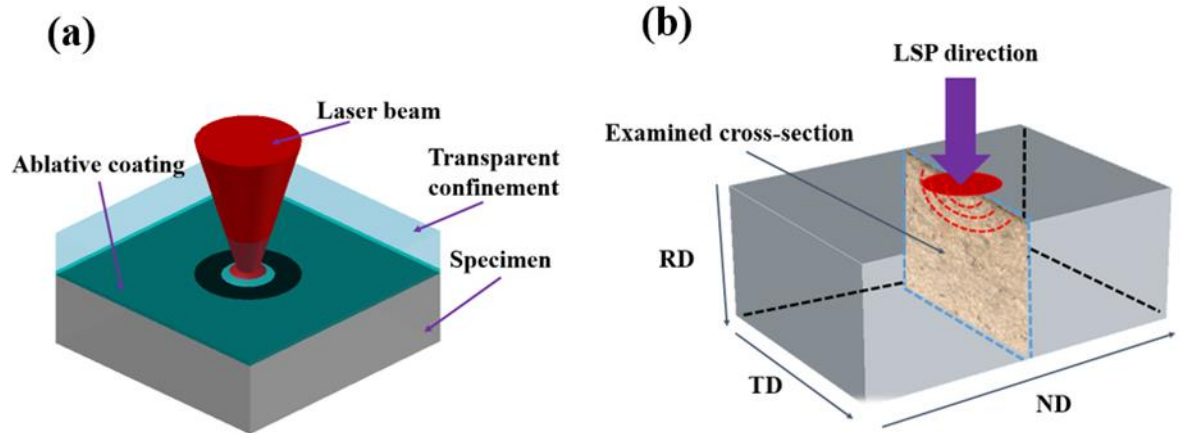
Figure 4.1. Schematic illustrations of: (a) LSP experimental set up, and (b) LSP direction and examined cross-section of the processed specimen, where the RD, TD, and ND are rolling, transverse, and normal direction, respectively.

The microstructure before and after LSP was characterized using OM, SEM and EBSD. EBSD characterization was performed in the stage control model with TSL data acquisition software on an area of 200 μm by 200 μm with a step size of 0.5 μm. All the microstructure characterization was performed on a cross-section perpendicular to the ND.

The surface micro-hardness of samples before and after laser processing were measured using a Wilson Hardness tester with a 500 g load and 10 s holding time. In order to study the effect of the gradient twinning microstructure on the material strength, in-depth hardness was measured from the top surface to a depth of 2300 μm on TD-ND planes in Figure 4.1b. An electrolytic polisher was used to remove the material layer by layer for in-depth hardness testing. At each depth, the hardness values were measured 5 times.

4.3. Results and discussion

4.3.1. Laser-induced shockwave pressure and propagation

In order to understand the process-microstructure relationship, the shockwave pressure during LSP is theoretically estimated. According to the widely accepted Fabbro's laser shock processing mode (Eq. 1-3) [11, 149], the magnitude of shockwave pressure $P(t)$ can be estimated as a function of the shock impedance Z (confining media Z_1 and target material Z_2) and the laser intensity $I(t)$, where $L(t)$ is the layer thickness of laser-induced plasma, α is the efficiency of the interaction (≈ 0.1), and t is the time.

$$\frac{2}{Z} = \frac{1}{Z_1} + \frac{1}{Z_2} \tag{1}$$

$$\frac{dL(t)}{dt} = \frac{2}{Z} P(t) \tag{2}$$

$$I(t) = P(t)\frac{dL(t)}{dt} + \frac{3}{2\alpha}\frac{d}{dt}\left[P(t)L(t)\right] \tag{3}$$

In this work, $Z_1 = Z_{glass} = 1.44 \times 10^6 g / cm^2 \bullet s$, $Z_2 = Z_{AZ31b} = 1.01 \times 10^6 g / cm^2 \bullet s$ [150], and $I(t)$ is given by Eq. 4 and 5 [151]:

$$I_0 = \frac{Q}{\pi(d/2)^2 \Delta t} \tag{4}$$

$$I(t) = I_0 \frac{1}{\sigma\sqrt{2\pi}} e^{-\frac{1}{2}(\frac{t-\mu}{\sigma})^2} \tag{5}$$

where I_0 is the maximum laser intensity, Q is the pulse laser energy, d is the beam diameter,

and Δt is the laser pulse duration. The value of σ and μ can be estimated from the effective

laser duration FWHM (full width at half maximum), $FWHM = 2\sqrt{2\ln 2}\sigma \approx 2.355\sigma = 5\text{ns}$

and $\mu = 6\sigma$.

Based on Eq. 1-5, the temporal evolution of shockwave pressure for various laser

intensities is calculated as shown in Figure 4.2. It can be seen that the shockwave pressure

in LSP experiments increases to their peak values within 20 ns and then decays gradually

with time. As the shockwave propagates into the Mg block, the effective pressure decays

with the increase of depth [152, 153].
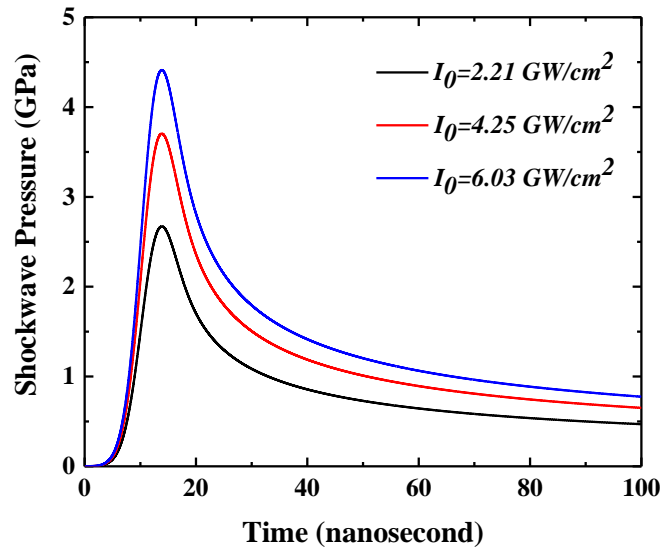
Figure 4.2. The temporal evolution of laser shockwave pressure as affected by the laser intensity in LSP experiments, estimated by Fabbro's model.

It is typically assumed that shock pressure follows a Gaussian spatial distribution, the spatially uniform shock pressure $P(t)$ relates to the spatially non-uniform shock pressure as [154] :

$$P(r,t) = P(t)\exp\left(-\frac{r^2}{2r_0^2}\right),$$
<div align="right">(6)</div>

where r_0 is the laser beam radius, and r is the distance from the center of the laser beam.

4.3.2. Gradient twinning microstructure

Figure 4.3 shows the initial microstructure of the specimen. It can be seen that the material has a twin-free equiaxed grain structure with an average grain size of 25 μm (Fig 3a and 3c). The EBSD phase mapping indicates a strong basal texture where most basal planes align parallel to the rolling direction (Figure 4.3b and d).
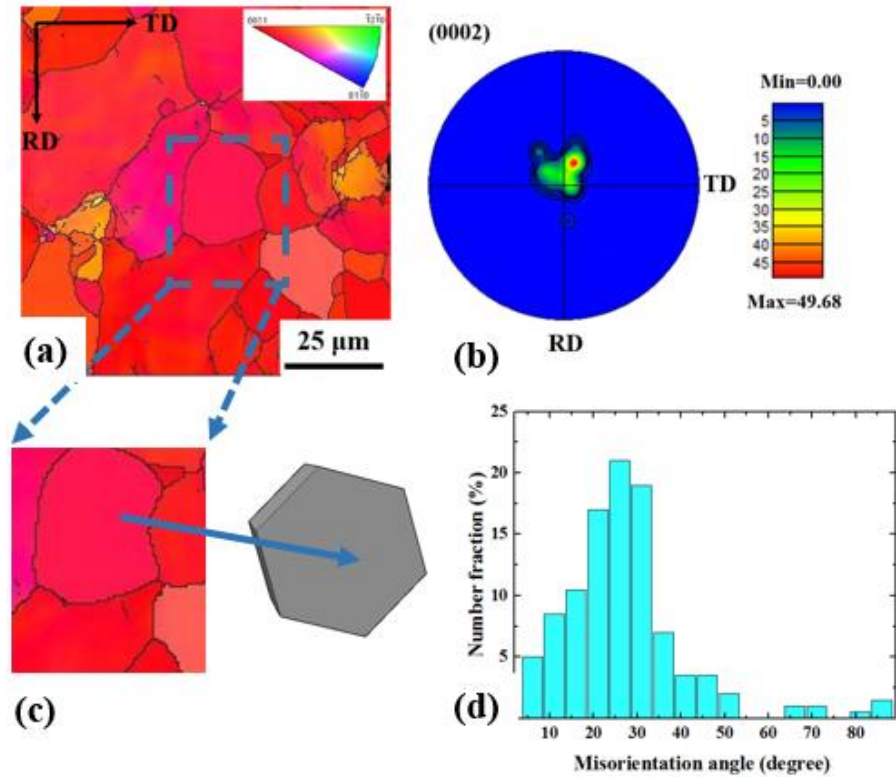
Figure 4.3. Initial microstructure of the cross-section perpendicular to ND of the as-received rolled AZ31b Mg alloys. (a) Inverse pole figure map, (b) (0002) pole figure, (c) a crystallographic orientation map, and (d) point to point misorientation angle distribution for grain boundaries.

Optical microscopy images in Figure 4.4 show the microstructure of the specimen processed by single pulse LSP with laser intensities of 2.21, 4.25, and 6.03 GW/cm^2. It can be seen that a depth-dependent microstructure in the specimens is generated by LSP. In Figure 4.4a, surface micro-indentations are observed on the top surfaces. A hemispherical distribution of twins can be identified and is marked by the red dashed lines in Figure 4.4b, c, and d. With the increase of laser intensity, the depth of LSP affected zone increases. For instance, the depth of the twinned area is about 850 μm in the specimen processed by LSP with a laser intensity of 2.21 GW/cm^2, while for the specimen processed

by LSP with a laser intensity of 6.03 GW/cm^2, the twinned area reaches to around 1650 μm. Moreover, a twin saturation or exhausted zone (i.e. the matrix is almost totally twinned) can be observed and marked by the blue dashed lines in Figure 4.4c and d. The saturated and unsaturated twinning areas can be easily identified, since after etching with acetic picral solution, the twin exhausted area (Figure 4.4e) exhibits a different color as compared to the unsaturated twin area (Fig. 4.4f).
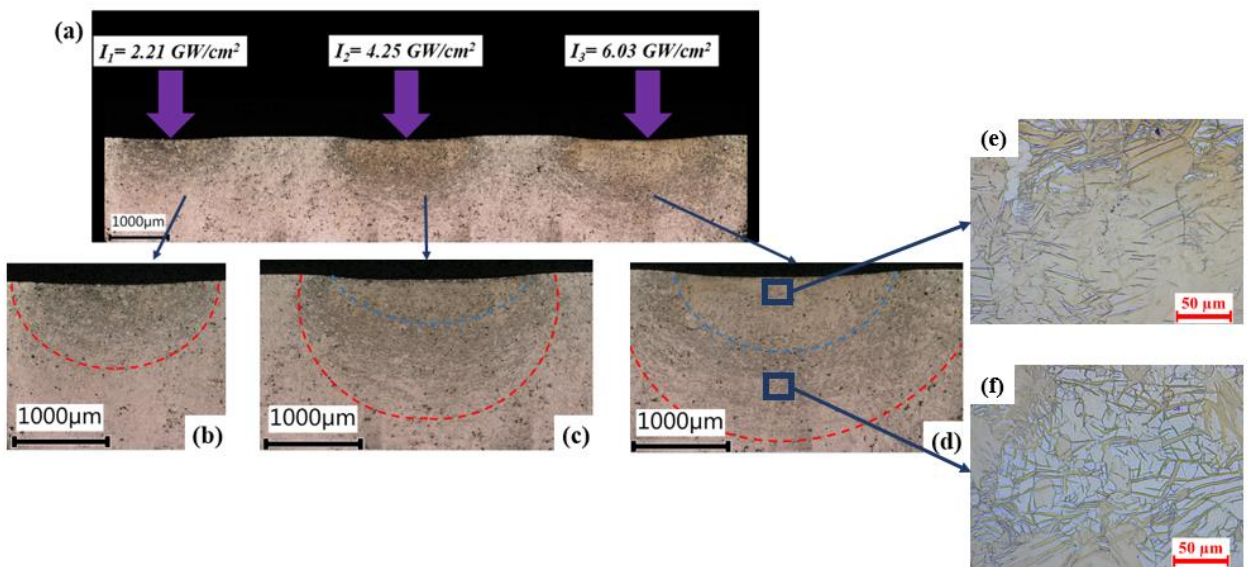
Figure 4.4. Optical microscopy images showing microstructure of AZ31b Mg alloy processed by single pulse LSP: (a) An overview of the cross-section of laser processed samples with surface micro-indentations; (b), (c), and (d) microstructure of the specimen processed by LSP with a laser intensity of 2.21, 4.25, and 6.03 GW/cm^2, respectively; (e) twinning exhausted area and (f) twinning unsaturated area.

EBSD analysis was conducted to characterize the gradient twinning microstructure generated by LSP. In Figure 4.5, the three inverse pole figure (IPF) maps at different depths are picked from the examined cross-section of Mg alloy samples processed by LSP with a laser intensity of 6.03 GW/cm^2. Compared with the initial microstructure, the

texture and crystallographic orientation distribution are dramatically changed by LSP, owing to the growth of deformation twinning. At a depth of 500 μm within the twin exhausted area, the parent grains are almost totally twinned. As the depth increases to 1000 μm, twins in green and blue can be seen but remaining parent grains can be identified. Moreover, some refined grains can be observed. At the depth of 1500 μm, needle-like twins with a low density can be observed and the majority of the parent grains remain are not twinned.
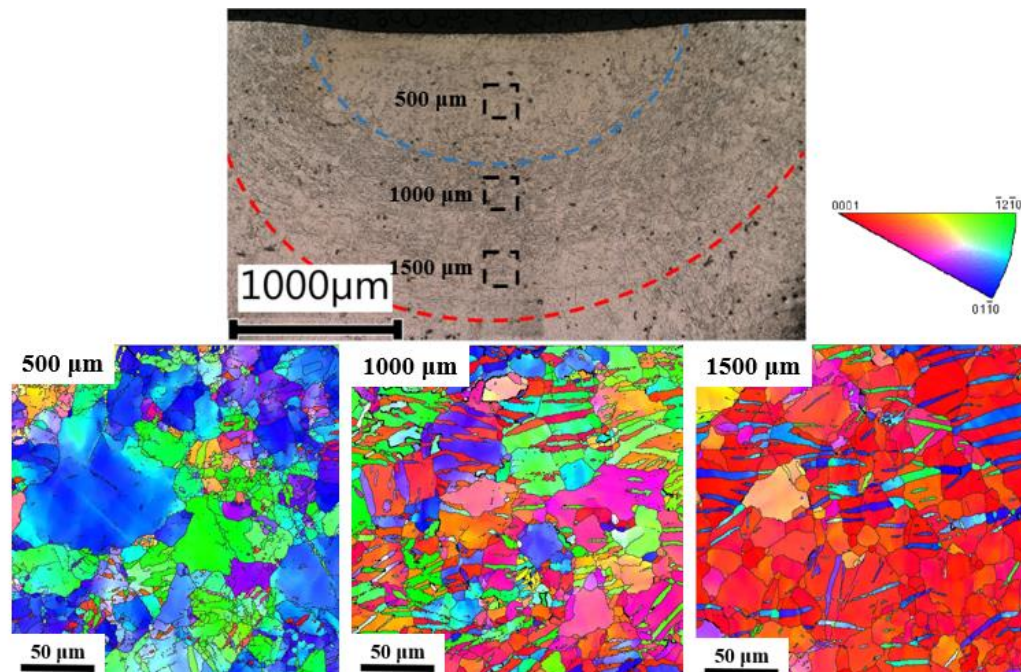
Figure 4.5. EBSD analysis of the detailed microstructure in three different depths of sample processed by LSP with a laser intensity of 6.03 GW/cm^2.

Figure 4.6 shows a detailed EBSD analysis of the microstructure of sample processed by LSP with a laser intensity of 6.03 GW/cm^2 at a depth of 500 μm. Figure 4.6a shows a very non-uniform grain size distribution, with both large grains and refined grains. Moreover, very few parent grains can be seen, indicating it is a twin saturated area. Figure

4.6b and 6c show some local areas which contain small patches of remaining parent grains. The point to point misorientation line profiles show that the misorientations between the parent grain and twin bands are about 86° (Figure 4.6d and e). This indicates that all the twin bands were generated by $\{10\bar{1}2\}$ twinning [30].
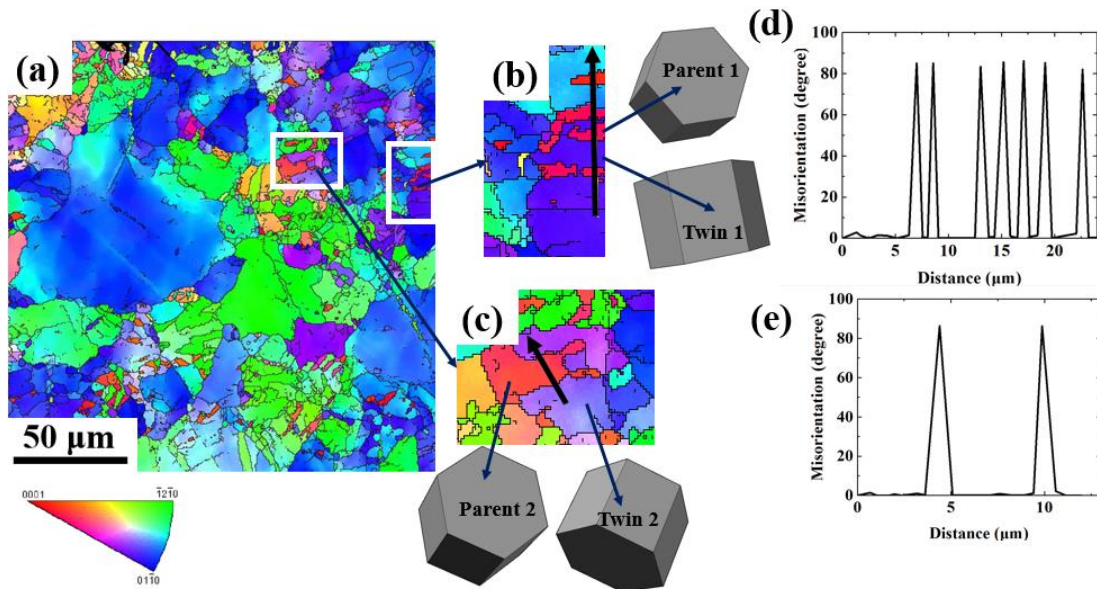
Figure 4.6. Inverse pole figure maps and crystallographic orientation analysis of microstructure of sample processed by LSP with a laser intensity of 6.03 GW/cm^2 at a depth of 500 μm. (a) Inverse pole figure map; (b) and (c) crystallographic orientation maps obtained from (a); (d) and (e) point to point misorientation line profiles along the direction indicated as an arrow in (b) and (c), respectively.

The effect of LSP on surface grain refinement of metallic materials has been extensively reported in literature [69, 71]. Ge et al. [56] reported that nano-grains with an average size of 17.5 nm can be generated in the top surface of AZ31b Mg alloy through LSP, and the thickness of the nanostructured layer is around 20 μm. Ren et al. [155] also demonstrated nano-structured surface layer can be fabricated in AZ91D Mg alloy by LSP.

In Figure 4.6, some very small untwinned grains are observed, showing the grain refinement effect. However, the grain refinement in the AZ31B Mg alloys subjected to LSP along RD is not as conspicuous as in metals in which dislocations dominate the plastic deformation. In addition to small grains, large grains can also be observed in Figure 4.6a. Hong et al. [156] investigated the twin morphology and texture evolution of AZ31B Mg alloys subjected to compression along TD. It was found that with a small deformation strain, the effective grain size tended to become smaller due to the grain refinement caused by twin nucleation. However, given a relatively large deformation strain, a grain coarsening effect was observed, leading to an increased grain size. The large grains observed in Figure 4.6a could be attributed to the relatively large strain at the near-surface region. On the other hand, no large grains can be found at the depth of 1500 μm (Fig. 7). The presence of large grains in Figure 4.6a is a unique phenomenon on Mg alloy samples subjected to LSP since most other metallic materials only exhibit grain refinement behavior after LSP [69, 157, 158]. These abnormally large grains might be related to one of the dynamic recrystallization (DRX) mechanisms-discontinuous DRX by grain boundaries migration [144, 159], or the twins coalescence in which the mechanism have been discussed in [156]. However, the presence of the large grains is not a general phenomenon and only occasionally observed in some areas.

Most of the investigation as mentioned above attributed the surface nano-crystallization to the dislocation glide driven by laser shockwave. However, these pioneer studies did not take into consideration the highly anisotropic mechanical behavior of Mg alloys. It is well known that for rolled Mg alloys, when the tensile stress is applied along the *c*-axis or the compression stress is applied perpendicular to the *c*-axis, as the case of LSP experiments

in this paper, deformation twinning is the dominant mechanism responsible for the plastic deformation [91]. In fact, as the critical resolved shear stress for $\{10\bar{1}2\}$ twinning is so small (comparable to basal slip and much lower than prismatic slip [160]), the plastic strain is accommodated by deformation twinning rather than the dislocation slip. Therefore, in the LSP process, if the laser shock loading is along RD or TD direction, the deformation twinning plays a dominant role in the microstructure-property relationship.

Figure 4.7 shows the EBSD analysis of the microstructure of the specimen processed by LSP with a laser intensity of 6.03 GW/cm^2 at a depth of 1500 μm. It can be seen that the majority of the grains exhibit the initial basal texture, indicating a low twin density. Figure 4.7a shows that the twins appear as thin needle-shape, which have a different morphology as compared with the twins in Figure 4.6a. Figure 4.7b shows a local grain which contains four twin laths, and the misorientation profiles in Figure 4.7c shows that those four twin laths have the same crystal orientation. Although $\{10\bar{1}2\}$ twinning has six possible twin variants, it can be seen that in most grains only one dominant twin variant is activated, as shown in Figure 4.7b. However, some grains do have more than one variants, as the twin 2-1 and twin 2-2 in Figure 4.7c. The activation of a twinning system depends on the initial crystal texture and shockwave pressure [161, 162].
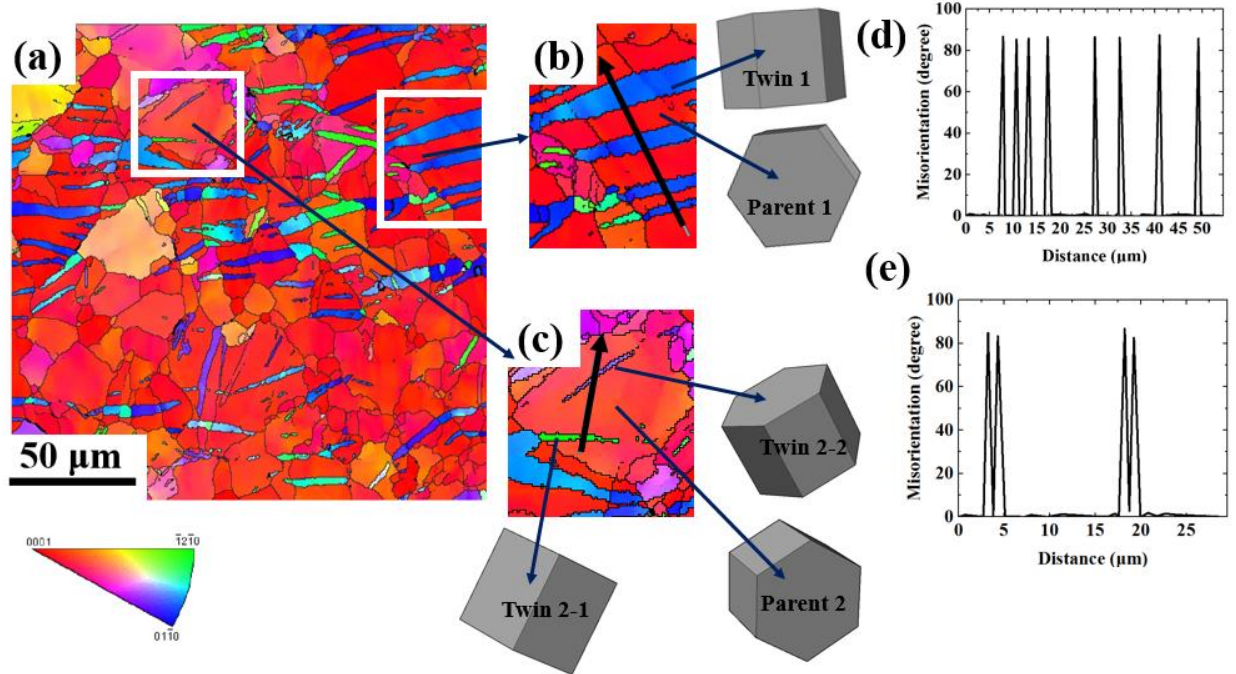
Figure 4.7. Inverse pole figure maps and crystallographic orientation analysis of the microstructure of sample processed by LSP with a laser intensity of 6.03 GW/cm^2 at a depth of 1500 μm. (a) Inverse pole figure map; (b) and (c) crystallographic orientation maps obtained from (a); (d) and (e) point to point misorientation line profiles along the direction indicated as an arrow in (b) and (c), respectively.

The evolution of the twin density and morphology with depth of the samples processed by LSP are presented in Figure 4.8. Figure 4.8a shows the effect of laser intensity on the gradient twinning microstructure of AZ31B Mg alloys generated by LSP. The value of *d* on each micrograph indicates the depth from the top surface where the microstructure is characterized. Each micrograph has a dimension of 250 by 180 μm. The twin volume fraction (TVF) at each depth is summarized in Fig. 8b. The optical microscopy analysis (Figure 4.8a) indicates a gradually decrease of twin density with increasing depth, which is consistent with the overall microstructure in Fig. 4.4. For example, at the depth of 90

µm, all the microstructures show a very high twin density, which are 82.3, 96.0, and 96.5% for the samples processed by LSP with a laser intensity of 2.21, 4.25, and 6.03 GW/cm^2, respectively. As the depth reaches 1530 µm, twins can barely be observed in the sample processed with a laser intensity of 2.21 GW/cm^2, and the twin densities for the samples processed with a laser intensity of 4.25 and 6.03 GW/cm^2 are 40.2 % and 78.3%, respectively. Moreover, a higher laser intensity leads to a higher TVF at the same depth. For instance, at the depth of 1170 µm, the sample processed with a laser intensity of 6.03 GW/cm^2 shows a saturated twinning zone, while much fewer twins can be identified for the specimen processed with a laser intensity of 4.25 and 2.21 GW/cm^2. At the depth of 2250 µm, there is a small amount of twins (11.4%) for the sample processed with a laser intensity of 6.03 GW/cm^2, while no twins can be observed in the other two samples processed with a lower laser intensity.
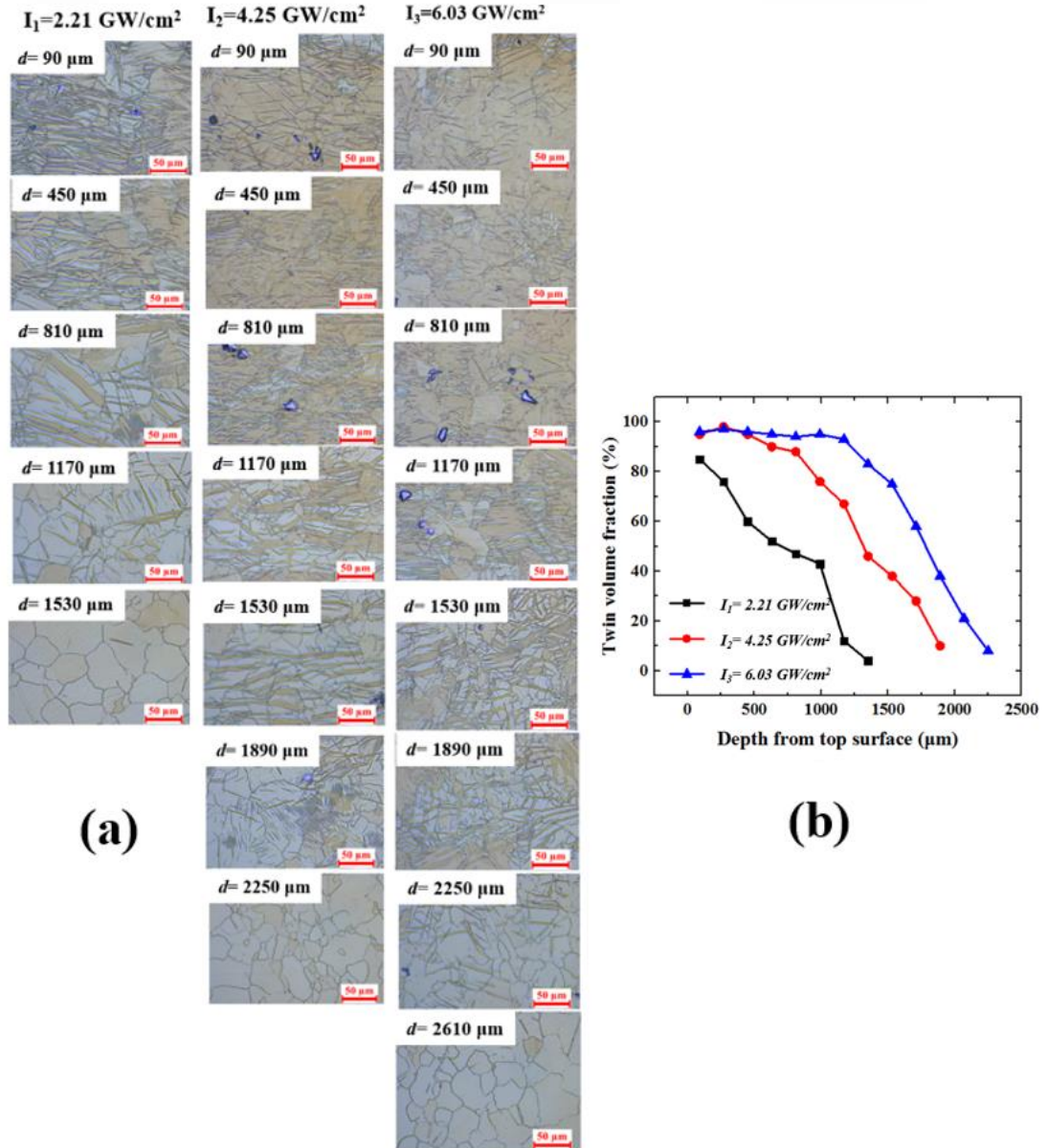
Figure 4.8. (a) Optical microscopy images of the in-depth microstructure of AZ31b Mg alloy samples processed by LSP with various laser intensities, and (b) variation of twin volume fraction with depth in AZ31b Mg alloy processed by LSP with different laser intensities.

In the LSP process, the amount of twin volume fraction in Mg alloys is related to the plastic strain that needs to be accommodated. The quantitative expression for the contribution of deformation twinning to plastic strain can be given as [156, 163].

$$\varepsilon_{twin} = f_{twin} \times \gamma_{twin} \times m \tag{7}$$

where ε_{twin} denotes the macroscopic strain, f_{twin} is the twin volume fraction, γ_{twin} is the magnitude of twinning shear, and m is the average Schmid factor of the twinning systems. Eq. 7 explains the gradient twinning microstructure of Mg alloys generated by LSP. With an increase of depth, the laser shock pressure decays [164], and thus the value of ε_{twin} decreases, leading to the decrease of twin volume fraction. Moreover, since the shockwave peak pressure for laser intensities used in this study is much higher than the dynamic yield strength of the AZ31B Mg alloys, a high plastic strain is expected at the near-surface area, resulting in the saturated twining zone.
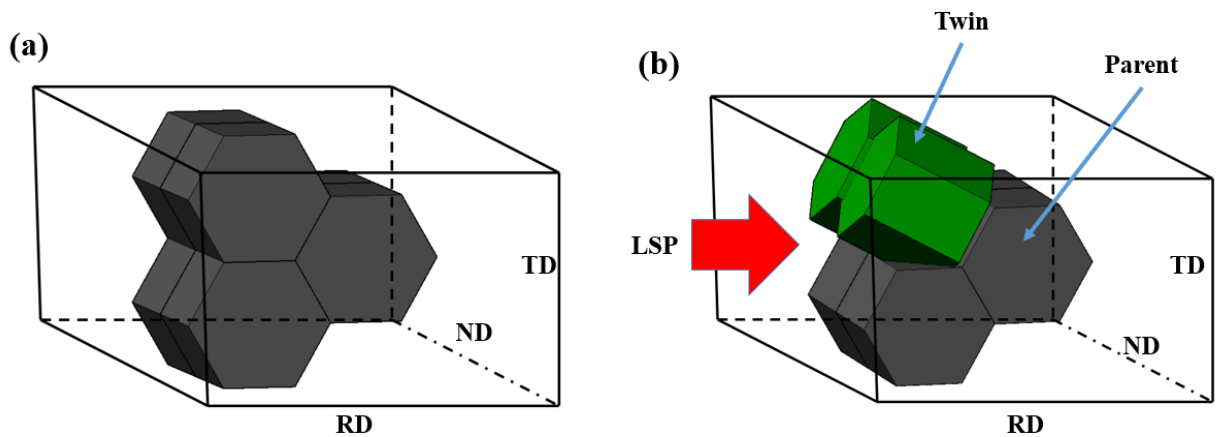
Figure 4.9. A schematic view of deformation mechanism of Mg alloys by LSP. (a) Initial crystal configuration, and (b) crystal configuration after LSP.

The deformation mechanism of the AZ31B Mg alloys processed by LSP along RD is illustrated in Figure 4.9. Figure 4.9a shows the initial crystal configuration for the as-received specimen, where the material exhibits the basal texture with *a*-axis parallel to the RD. Figure 4.9b shows the crystal configuration when the material is subjected to laser shock loading along *a*-axis direction. Noted that although several different twin variants might be activated in one grain, the variant with the highest Schmid factor value dominates, which agrees with the analysis by Hong et al. [156]. As shown in Figure 4.9b, due to the laser shock loading, the initial crystals (marked by dark color) with *c*-axis parallel to ND are transferred to twin crystals (marked by green color) with *c*-axis perpendicular to ND with a crystallographic lattice orientation of 86.3°. This crystal reorientation is attributed to the generation of $\{10\bar{1}2\}$ extension twins [30].

4.3.3. Gradient strain hardening mechanism

To investigate the effect of gradient twinning microstructure on the mechanical properties of the AZ31B Mg alloy, micro-hardness tests at various depths were conducted as shown in Figure 4.10. It can be noted that Vickers hardness numbers (VHN) of the specimen processed by LSP decrease with increasing depth till 60 VHN, which is the hardness of the base materials. The maximum VHNs for three different laser processing intensities are all around 74 VHN, indicating a saturation point for hardness improvement by LSP. The saturation of surface strength by LSP has also been reported for other metallic materials [53]. It is also observed in Figure 4.10 that a higher laser intensity leads to a larger hardening depth. For example, by increasing laser intensity from 2.21 to 6.03

GW/cm^2, the depth of full-hardened layer (72 VHN) increases from around 500 to 1500 μm.
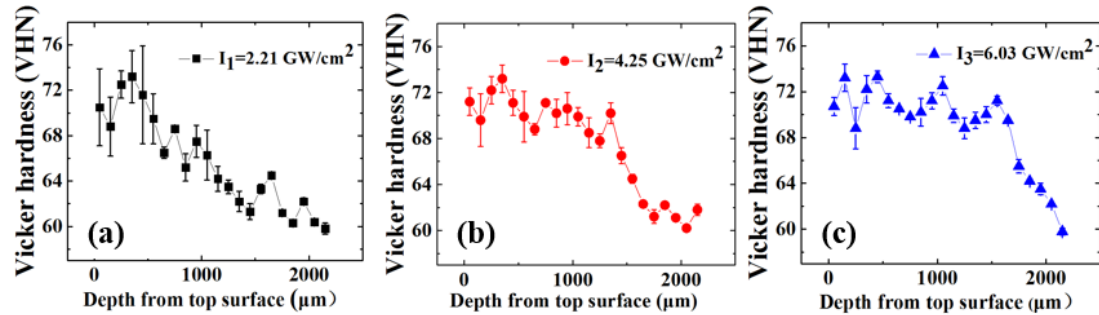
Figure 4.10. In-depth hardness distribution of AZ31b Mg alloys processed by LSP with various laser intensities of: (a) 2.21, (b) 4.25, and (c) 6.03 GW/cm^2.

Surface hardening effect induced by LSP on metallic materials has been extensively studied. It is well accepted that the improved hardness is due to the grain refinement [69, 71] for the metallic materials with a BCC or FCC crystal structure, like steels and aluminum alloys [8, 63], in which the plastic deformation is accommodated by dislocation slip. However, for Mg alloys with a HCP crystal structure, in addition to grain refinement, deformation twinning is another important factor contributing to the surface hardening by LSP. Texture change by deformation twinning will change the deformation modes and thus affect the surface hardness. If an external compressive stress is applied along the *a*-axis, {$10\bar{1}2$} twinning dominated deformation will induce a relatively lower flow stress, while if the compressive stress is applied along the *c*-axis, the deformation mode is highly favorable for slip or contraction twinning, which have a higher CRSS (critical resolved shear stress), and thus induce a higher flow stress [156, 162]. Knezevic et al. [165] proposed that the main contribution of extension twining to the strain hardening in TD-RD

compressed samples is texturing hardening. In this study, the crystal reorientation by LSP will change the deformation mode from an easy-to-deform direction (compression along *a*-axis) to a difficult-to-deform direction (compression along *c*-axis). As a result, both grain refinement and texture change are expected to contribute to the surface hardening of Mg alloys processed by LSP.

4.3.4. Anisotropic microstructural and mechanical response to LSP

For Mg alloys, their anisotropic mechanical properties may lead to an anisotropic microstructural response to LSP. To study this effect, LSP experiments with a laser intensity of 2.21 GW/cm^2 were carried out both along ND and RD. As the SEM images shown in Figure 4.11, high density twins can be observed when LSP is along the RD, while almost no twins can be observed when LSP is along the ND. This result is consistent with observation of the microstructure evolution under static compression along ND conducted by previous researchers [103, 166]. When a compressive stress is applied along ND, the plastic deformation is mostly accommodated by dislocation slip on the basal and pyramidal planes [167]. Thus twinning microstructure cannot be achieved by LSP along ND. However, some refined grains can be identified in the near surface area in Figure 4.11b, as marked by the yellow circle. Since the plastic deformation of Mg alloys is dominated by dislocation activities instead of twinning in compression along ND [38, 168], the grain refinement in AZ31B magnesium alloy processed by LSP along ND should be attributed to the formation of dislocation walls and cells as in the cases of other metallic materials subjected to LSP, like steels [71], aluminum alloys [69] , and titanium alloys [158]. When the Mg alloys are subjected to plastic deformation induced by LSP along ND, dislocations

accumulate and rearrange for minimizing the total energy state, resulting the formation of dense dislocation walls and cells. These dislocation walls and cells subdivide the original grains and finally lead to the formation of refined grains.
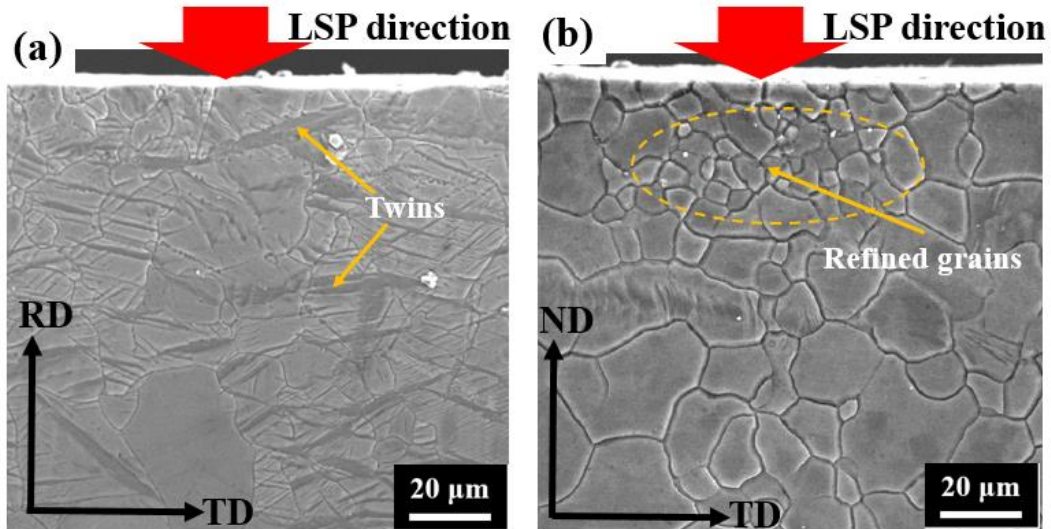
Figure 4.11. SEM images of microstructure of the AZ31B Mg alloys processed by LSP along (a) RD, and (b) ND. Red arrow indicates the direction of laser shock loading.

The surface (RD-TD plane) hardness tests of the AZ31B Mg alloys processed by LSP along ND with different laser intensities were also conducted and the results were compared with those of samples processed by LSP along RD. As shown in Figure 4.12, it can be seen that the surface hardness value of AZ31B Mg alloy increases from 63.2 VHN for the untreated specimen to 72.3 VHN for the sample processed by LSP along ND with a laser intensity of 2.21 GW/cm^2, corresponding to a 14.4% increase. The surface hardness improvement is mainly attributed to the grain refinement generated by LSP. As the laser intensity increases from 2.21 GW/cm^2 to 6.03 GW/cm^2, the surface hardness value only increases from 72.3 to 74.1 VHN, which is due to the plastic deformation saturation effect

[51]. Moreover, it should be noted that the surface hardness values of the AZ31B Mg alloy before and after LSP along ND are all slightly higher than those of samples processed by LSP along RD regardless of laser intensity. This difference is mainly attributed to the fact the strain hardening effect induced by dislocation (LSP along ND and hardness tests on RD-TD plane) is typically more prominent than it is induced by twinning (LSP along RD and hardness tests on TD-ND plane) [165]. Nevertheless, LSP along ND and RD can both efficiently improve the surface hardness.
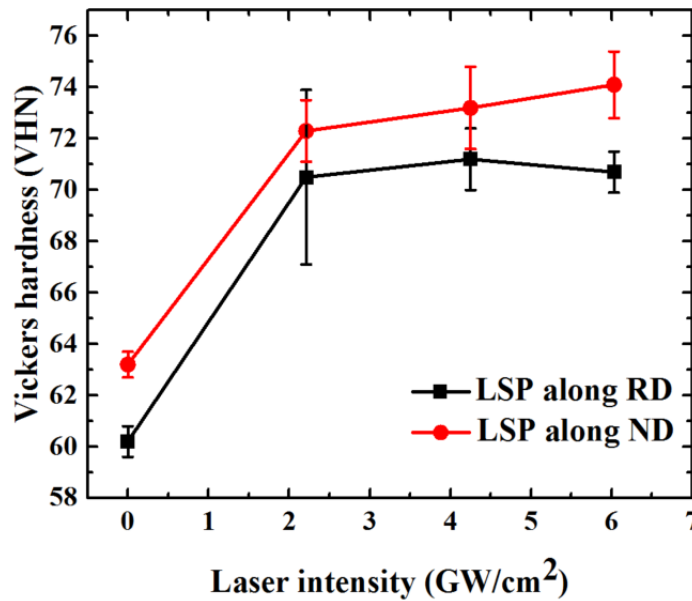
Figure 4.12. Anisotropy in hardness improvement of the AZ31B Mg alloy processed by LSP with different laser intensities.

4.4. Summary

In this chapter, a systematic study is carried out on the process-microstructure relationship of Mg alloys as processed by LSP. A focus is placed on understanding the deformation twinning mechanism and twinning-induced strain hardening effect during

LSP. The twinning type, morphology, variation in TVF vs depth, and corresponding in-depth hardening effect are analyzed. Following conclusions can be drawn:

(1) When LSP is along RD, a gradient twinning microstructure is generated. The twins are identified as $\{10\bar{1}2\}$ extension twins. The density of twins decreases with increasing depth, and a higher laser intensity results in a deeper twinned zone.

(2) A gradient hardness distribution well corresponds to the gradient twinning microstructure. The hardness of laser-processed samples decreases with an increase of depth from the saturation value of 74 VHN to the base value of 60 VHN. The LSP-induced strain hardening is attributed to the grain refinement and the texture change induced by nucleation and propagation of twinning structures.

 (3) Anisotropic microstructural and mechanical response to LSP is observed. High density twins can be observed when LSP is along the RD, whereas some refined grains can be observed when LSP is along the ND. LSP treatment of AZ31B Mg alloys along ND and RD can both enhance the surface hardness.

Chapter 5. Twin-twin interaction in Mg alloys processed by LSP

5.1. Introduction

$\{10\bar{1}2\}\langle10\bar{1}\bar{1}\rangle$ twinning plays an important role during plastic deformation of Mg alloys and has been extensively studied in the past decades [30, 34, 169]. It can be easily activated when a Mg crystal is subjected to tensile stress along the c-axis and results in a lattice orientation of 86.3° around $\langle1\bar{2}10\rangle$ zone axis [35]. Under some loading circumstances, multiple twin variants can be activated simultaneously and interact with each other, leading to twin-twin interaction. Recent studies show that twin-twin interaction has an important impact on twin propagation, de-twining, and twinning-induced strain hardening effect of Mg alloys [170-173].

Due to its scientific significance, experimental and numerical studies have been carried out to investigate twin-twin interactions of Mg alloys. For instance, Yu et al. [174] proposed that when two twin crystals with large misorientation angles interact with each other, their slip transmission is difficult. Chen et al. [175] reported that when a twin variant propagates and impinges on another, its growth will be retarded at the location of impingement, but the retardation depends on the angle between the sides of the intersecting twins. Gong et al. [176] studied the non-co-zone twin-twin interactions via atomistic simulations and showed that the growth of both twins are impeded upon interaction.

Despite these works, little efforts have been made to investigate twin-twin interaction in Mg alloys under ultra-high strain rate deformation (~10^6/s). The twinning behavior might be affected by the strain rate [177, 178] and additional twinning modes could be activated and interact with each other with a higher strain rate [179]. Thus, it is of

importance to explore twin-twin interaction in Mg alloys under extreme deformation conditions.

LSP a surface treatment technique that has been widely used to study high strain-rate response of metallic materials [11, 63, 180]. During LSP, pulsed laser with an ultra-short duration (on an order of nanosecond) is delivered to an ablative coating, forming a high-temperature plasma and generating a high shockwave pressure (on the order of GPa) on the sample being processed. As the shockwave propagates into the target materials, the near surface layer (typically 0~2000 μm) undergoes an ultra-high strain rate plastic deformation [11, 148, 181]. In this work, twin-twin interaction in an AZ31B Mg alloy under ultra-high strain rate compression introduced by LSP was studied. The morphology of twin variants was characterized by EBSD characterization. Notably, this part of content is basically adapted from [182] (with permission from publisher).

5.2. Experiments

Samples for LSP experiments were cut from a rolled AZ31B Mg block (3.0 wt% Al, 1.0 wt% Zn, Mg balance) purchased from Metalmart.com. Prior to LSP, the surface containing the ND and the TD of the sample was mechanically grinded with a series of sand papers (down to 1200 grit number) followed by a final polishing using 3 micron diamond suspension. The examined RD-TD cross section was cut along the diameter direction of the laser beam spot by a low-speed diamond saw and then prepared for EBSD characterization.

5.3. Results and discussion

5.3.1. Abnormal twin-twin interactions

The initial microstructure and texture of the RD-TD cross-section of the as-received Mg alloy sample before LSP is shown in Figure 5.1a. It can be seen that, before LSP, the material has a twin-free, equiaxed grain structure with a strong basal texture. After LSP, EBSD analysis was performed at the depths of 500, 700, 900 and 1100 μm from the processed surface and the results are shown in Figure 5.1b-e. From the inverse pole figure (IPF) maps and the (0002) pole figures, it can be seen that $\{10\bar{1}2\}$ extension twinning was activated. Close to the surface, the parent grains were nearly all twinned (Figure 5.1b), because the loading condition strongly favors $\{10\bar{1}2\}\langle10\bar{1}\bar{1}\rangle$ twinning [34]. Due to the attenuation of the laser intensity [183], the twin volume fraction decreases with depth. To characterize the nature of interfaces, we highlight different types of grain boundaries with different colors in the image quality maps: the blue lines represent twin boundaries (TBs) of $86.3\pm5°\langle11\bar{2}0\rangle$, characteristic of $\{10\bar{1}2\}$ extension twins; the yellow lines represent TBs of $56\pm5°\langle11\bar{2}0\rangle$ from $\{10\bar{1}1\}$ contraction twins which have a very low density; a few green lines of $38\pm5°\langle11\bar{2}0\rangle$ can also be seen, which represent $\{10\bar{1}1\} + \langle10\bar{1}2\rangle$ double twins. Notably, a quite high density of red boundaries can be identified in the LSP affected areas. These are $60\pm5°\langle10\bar{1}0\rangle$ boundaries formed when different $\{10\bar{1}2\}$ twin variants impinge [174]. The density of $60\pm5°\langle10\bar{1}0\rangle$ boundaries decreases with increasing depth, indicating that multiple $\{10\bar{1}2\}$ twin variants were activated and strongly interacted with each other during LSP processing. More detailed analysis of the twin variants their orientations are provided below.
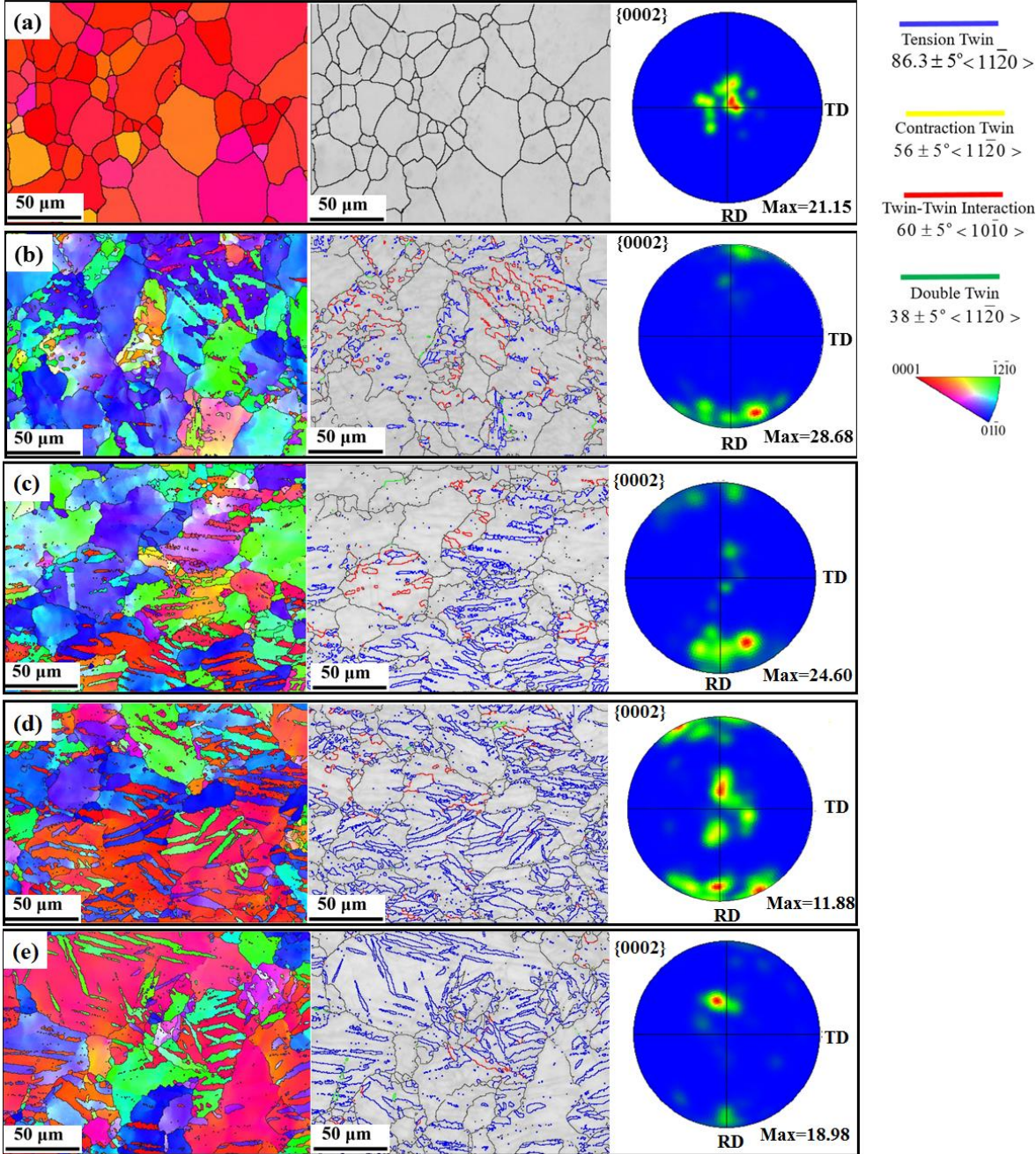
Figure 5.1. (a) Microstructure and texture of the as-received AZ31B Mg alloy. (b-e) Evolution of microstructure and texture at various depths from the laser processed surface: (b) 500 μm; (c) 700 μm; (d) 900 μm; (e) 1100 μm. The twin volume fraction decreases with increasing depth. The density of $60\pm5°\langle10\bar{1}0\rangle$ boundaries (in red) also decreases with increasing depth.

EBSD scans with a higher resolution were then performed in selected areas which contain multiple twin variants such that details of twin-twin interaction can be better revealed. The red patches, marked as M, are the leftover of parent grains that are not totally twinned. These parent grains contain two twin variants: T_1 and T_2 (Figure 5.2a). The image quality map (Figure 5.2b) and crystallographic orientation analysis (Figure 5.2c-d) indicate that the interfaces between T_1 and T_2 are $60\pm5°\langle10\bar{1}0\rangle$ type, which result from twin-twin interaction. Secondary twins can also be observed. For example, T_3 is another primary twin variant and this variant was transformed to secondary twins T_4 and T_5. Note that the boundary between T_4 and T_5 also satisfies $60\pm5°\langle10\bar{1}0\rangle$. The unit cells and crystallographic relationship among M, T_3, T_4, and T_5 is shown in Figure 5.2e.
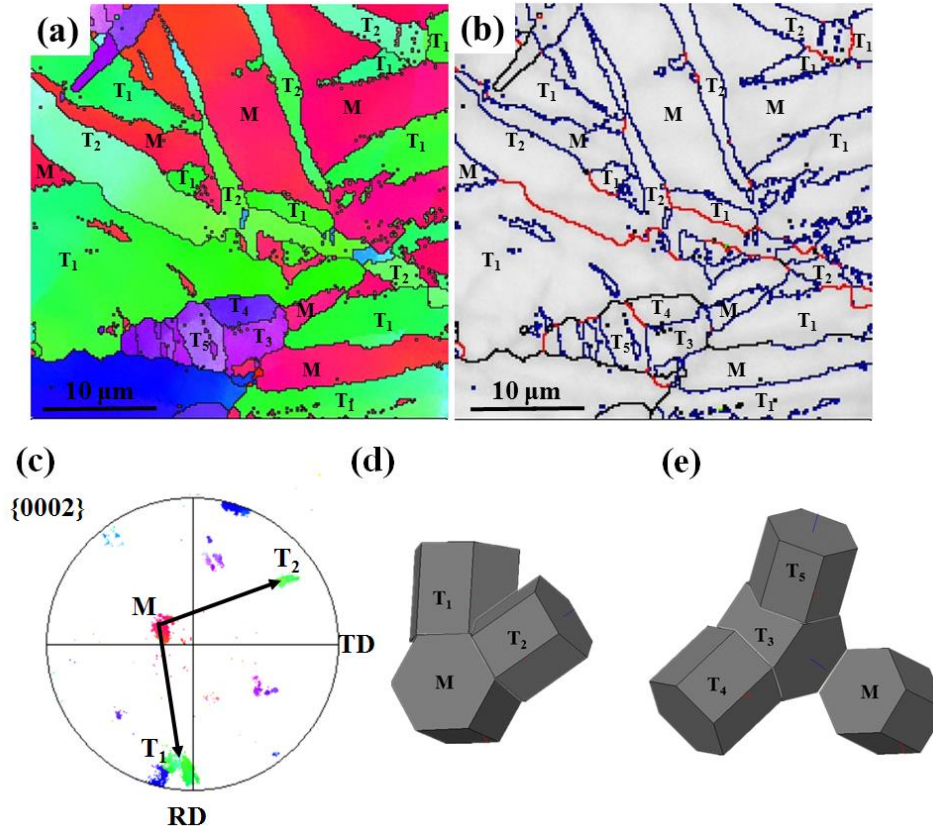
Figure 5.2. (a) IPF map of a selected area. Two twin variants T_1 and T_2 are activated in the parent M. (b) Image quality map. The yellow lines are the interfaces between T_1 and T_2. (c) Corresponding (0002) pole figure. (d) Unit cells of the parent M, and the two twin variants T_1 and T_2. (e) Unit cells of parent M, primary twin variant T_3, and two secondary twin variants T_4 and T_5.

A salient feature of the boundaries resulting from twin-twin interaction induced by ultra-high strain rate deformation is the closed, circular interfaces, as shown in Figure 5.3. Highly irregular interfaces between $\{10\bar{1}2\}$ twin variants were only recently reported by Chen et al. in an AZ31 Mg alloys with very coarse grains (~120 μm). Figure 5.3a-b show several isolated twin variants of T_2 that are surrounded by variant T_1. The misorientation angle between variant T_1 and T_2 satisfies $60\pm5°\langle10\bar{1}0\rangle$, as shown in the image quality map

in Figure 5.3b. The parent grain has almost been totally twinned into variant T_1. However, some variants T_2 are completely surrounded by variant T_1. It is likely that during twin growth, variant T_1 outgrew the twin lamella of T_2 and then totally enclosed T_2 inside. As the interaction continued, part of the T_2 may have been transformed to T_1, leading to the disconnected, abnormal morphology. A similar scenario is shown in Figure 5.3c-d in which some disconnected islands can be observed. These disconnected islands belong to the same twin variant T_4.
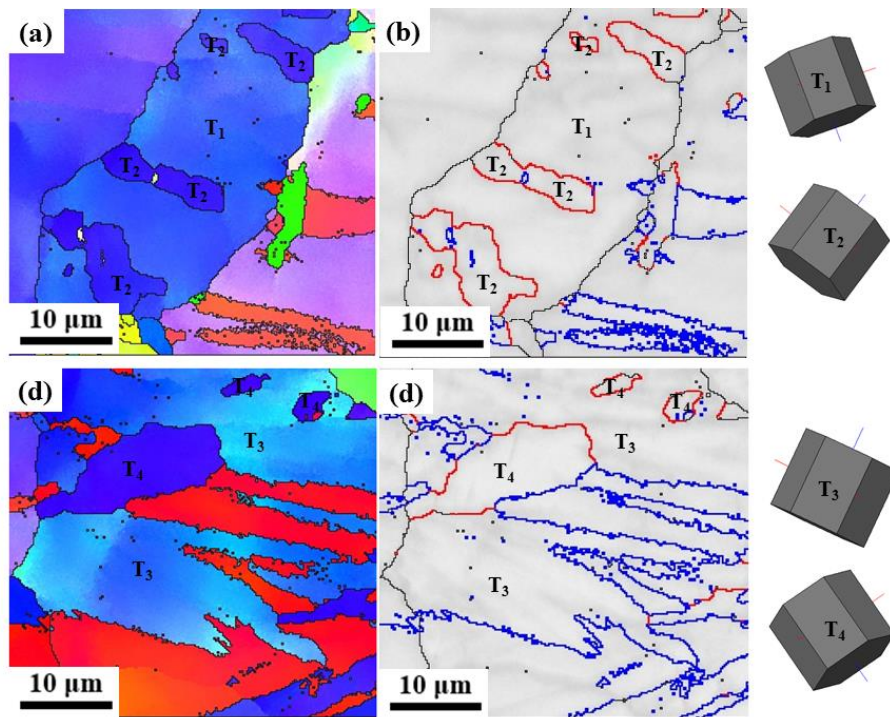
Figure 5.3. (a) Twin variant T2 is surronded by twin variant T1, leading to the isolated T2 islands in a parent grain. (b) Image quality map of (a). (c) Twin variants T4 is surronded by twin variant T3, leading to isolated T4 islands in another grain. (d) Image quality map of (c).

5.3.2. The mechanism of twin-twin interactions

The abnormal morphology of the interface between different twin variants simply cannot be explained by any twinning dislocation theories because, by definition, a twinning dislocation can only glide on the twinning plane and produce a simple shear. When two or more variants approach each other, the stress field of the twinning dislocations of one twin variant will repel the twinning dislocations of the other twin variants, if we assume the interfaces between a twin variant and the matrix are composed of a multitude of twinning dislocation loops on consecutive twinning planes and lateral growth of the twin is controlled by the expansion of the loops [30]. Thus, it is unlikely that, as one variant impinges on a different variant, the growth front of the incident variant branches out and changes the habit plane. This is exactly the case in twinning in FCC and BCC metals, as schematically demonstrated in Figure 5.4a. The expansion of twins has to halt when two variants approach close to each other because the twinning dislocations cannot penetrate the twin boundaries. As a result, the parent grains cannot be twinned by 100%. To account for the fact that parent grains can be totally twinned by $\{10\bar{1}2\}$ twinning in HCP metals, Song and Gray [184] first questioned the twinning dislocation theories in which $\{10\bar{1}2\}$ is mediated by twinning dislocations just like other twinning modes. They proposed that the growth of $\{10\bar{1}2\}$ twins was controlled by coordinated movements of a large number of atoms rather than by twinning dislocations gliding on the twinning plane.

Recently, Li and Ma [185] proposed that $\{10\bar{1}2\}$ twinning is mediated purely by atomic shuffling, not by twinning dislocations. The atomic shuffles transform the parent basal plane to the twin prismatic plane and vice versa, without involving any twinning

dislocations. More recently, Li and Zhang [90] proved that the $\{10\bar{1}2\}$ twinning plane is not an invariant plane. Consequently, no twinning shear can occur on the twinning plane. As such, $\{10\bar{1}2\}$ twin boundaries can be extremely incoherent, as confirmed by numerous experimental studies [85, 138, 186-189]. The abnormal interfacial structure between different $\{10\bar{1}2\}$ twin variants can be well explained by these non-twinning-dislocation models. As shown in Figure 5.4b, two or more twin variants are activated inside a parent grain. As observed in extensive transmission electron microscopy (TEM) experiments, the twin boundaries can be extremely incoherent, although microscopically the twin variants still assume a lamellar shape [85, 190-192]. As the twin variants approach each other, one variant may impinge on the other. However, the twin growth is not halted by the impingement. Instead, one variant can branch out and change the habit plane because no twinning dislocations are gliding on the twin boundary which should coincide with the twinning plane according to classical twinning theory. As a result of such non-classical twin growth, a parent grain can be twinned 100% and a twin variant can be totally surrounded by another variant.

Based on atomistic simulations, Serra et al. [193, 194] proposed that $\{10\bar{1}2\}$ twinning is mediated by "disconnections" rather than zonal twinning dislocations. However, as analyzed in recent work [191] the lattice correspondence in the reports of "disconnections" is exactly the same as the Li-Ma shuffling model [89]. In fact, the "basal to prismatic and prismatic to basal" lattice transformation can be readily identified in most of the atomistic simulations in the literature. Such a transformation must distort the structure of the twinning plane and thus no twinning shear should occur on the twinning plane [90].

The abnormal interaction between different twin variants provide new insight on the non-classical twinning behavior that has been observed extensively in experimental studies. For example, Li et al. [195] observed in TEM that a twin variant was able to penetrate a grain boundary and extend into the neighboring grain. It is well known that a twinning dislocation cannot penetrate a grain boundary. The well-observed "apparent crossing" during twin-twin interaction [171-174, 196] in Mg alloys and other HCP metals can now be well explained. Shi et al. [171] showed that when one twin impinges on another twin lamella, it looks like that a new twin with the same crystallographic orientation emerges on the other side of the impinged lamella. Mokdad et al. [172] also observed that impinging twins were linked on each side of twin lamella. Similar observation is also found in Figure 5.2a-b, in which two twin variants T_1 are linked on each side of T_2. A schematic explanation of these phenomena is shown in Figure 5.4c, when two $\{10\bar{1}2\}$ twin variants impinge, one variant can spread laterally and grow around the other variant. When a cross-sectional view is made, it looks like that one variant crosses the other.
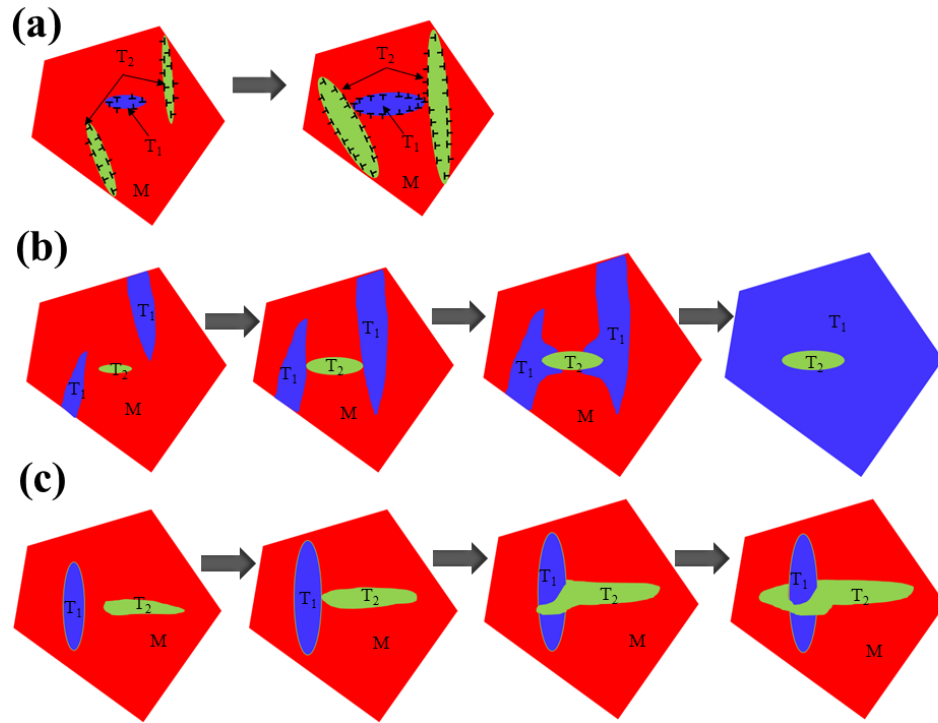
Figure 5.4. (a) Twin-twin interaction when growth of the twin variants is controlled by twinning dislocations on the twin boundaries. The growth of the twin variants will be impeded as the variants approach close to each other because the twinning dislocations are unable to penetrate the twin boundaries. (b) Non-dislocation mediated twin growth. A twin variant can branch out by changing the habit plane and surround the other variant. Eventually, the parent grain can be totally twinned. (c) Non-dislocation mediated twin growth. A twin variant can spread laterally and grow around the other variant, forming an "apparent crossing" structure.

5.4. Summary

In this chapter, the twin-twin interactions in an AZ31B magnesium alloy subjected LSP was investigated. EBSD characterization of the interfaces between different $\{10\bar{1}2\}$ twin variants shows that these interfaces present abnormal morphologies that cannot be accounted for by twinning dislocation theories. Patches of one variant can be completely

surrounded by another variant. Such an abnormal behavior of twin-twin interaction can only be explained by non-twinning-dislocation theories that fundamentally differ from the classical twinning theory.

Chapter 6. Enhanced tribological properties of Mg alloys processed by LSP

6.1. Introduction

Mg its alloys offer lightweight alternatives to conventional metallic materials due to their good strength-to-weight ratio, machinability and recyclability [14, 197]. However, their potential applications are currently restricted due to their poor formability, limited ductility and low wear resistance at room temperature [15, 46, 198]. New alloy design and processing strategies have been developed in recent years in order to overcome these barriers [122, 199, 200], while most of them aim to improve the ductility and/or strength of Mg alloys. In some applications, such as pistons, valves, bearing, sliding seals and gears, Mg alloys are subjected to sliding motion where friction and wear performance is of specific importance [104, 201]. Moreover, sliding wear is an important consideration in the forming process of Mg alloys, such as drawing, extrusion and forging [106]. Therefore, improving the tribological properties of Mg alloys is of critical importance for expanding their engineering applications.

Several studies have been conducted to investigate the tribological properties of Mg alloys as affected by various tribological conditions including applied load, sliding speed, temperature and lubricated conditions [106, 109, 202-207]. For instance, Anbu et al. [203] studied the wear mechanism of a casted ZE41A Mg alloy. Five wear mechanisms were proposed including abrasion, oxidation, delamination, plastic deformation, and melting. Taltavull et al. [204] investigated the effects of applied load and sliding speed on the wear behavior of an AM50 Mg alloy. It was found that the wear behavior transitioned from

abrasion and adhesion to severe plastic deformation with increasing applied load and sliding velocity. Liang et al. [208] explored the correlation between friction-induced microstructural evolution and tribological properties of AZ31 Mg alloys. It was found that a solidified layer formed beneath the worn surface followed by a dynamic recrystallization zone and a deformed zone.

Despite the aforementioned studies, little attention has been placed on investigating how the tribo-performance of Mg alloys is affected by deformation twinning, which is the prevalent plastic deformation mechanism in Mg alloys due to their limited slip systems at ambient temperature [89]. Twins are lenticular grains with a different but well-defined crystallographic orientation from the parent grain activated typically by a homogeneous simple shear [30]. Among the multiple modes, $\{10\bar{1}2\}\langle10\bar{1}\bar{1}\rangle$ extension twinning is the most commonly observed twinning mode in Mg alloys. Recent studies show that the pre-existing $\{10\bar{1}2\}\langle10\bar{1}\bar{1}\rangle$ twins can effectively improve the surface hardness [148] , tensile strength [209], and stretch formability [210] of Mg alloy. It is of specific scientific and technical importance to investigate the effect of surface pre-twinning on the friction and wear performance of Mg alloys processed by LSP.

This research aims to understand the friction and wear properties of Mg alloys as affect by deformation twinning introduced by LSP. AZ31B Mg alloy samples with various twin volume fraction (TVF) are prepared by LSP. Sliding tests under dry condition are conducted for friction and wear testing. The COF values and wear tracks are measured and analyzed. The relationship among the TVF, COF, and wear resistance are discussed. A possible mechanism responsible for the effect of TVF on the tribo-performance of Mg

alloys is proposed. We envision the results in the present study can offer new insights on designing and developing Mg alloys towards enhanced tribological performance. Notably, this part of content is basically adapted from [211] (with permission from publisher).

6.2. Experiments

Rolled AZ31B Mg alloy plate purchased from Metalmart International Inc. was used for our experiments. Square plate samples with a width of 25 mm and a thickness of 10 mm were cut and then processed by LSP to prepare samples with various TVFs. Prior to LSP, sample surfaces were grinded using SiC sandpapers with different grit numbers (from 320 to 1200), followed by fine polishing using 3 micron diamond suspension. LSP experiments were conducted with a laser intensity of 1.5 GW/cm^2 along the RD of the sample. The schematic view of LSP configuration is shown in Figure 6.1a. In this study, a Q-switched Nd-YAG laser operating at a wavelength of 1064 nm and a pulse width of 7 ns (full width at half maximum), was used to deliver the laser energy. A black tape was used as the ablative coating and BK7 glass was used as the transparent confinement.

Note that in addition to high density of deformation twinning, nano-sized grains might be produced in the very top surface layer of Mg alloys by LSP [145, 212, 213]. In order to eliminate the effect of grain refinement on tribological properties, the LSP-processed samples were electrochemically polished to remove the top layer with a thickness of 50 μm. This will also eliminate the surface roughening effect induced by LSP [64]. Mg alloy samples with various TVFs were prepared by electrochemical polishing of laser-processed samples to remove the top layer with a series of thickness from 50-450 μm, as shown in

Figure 6.1b. All the samples subjected to tribological tests were polished to reach a surface roughness less than 100 nm and then ultrasonically cleaned by acetone.
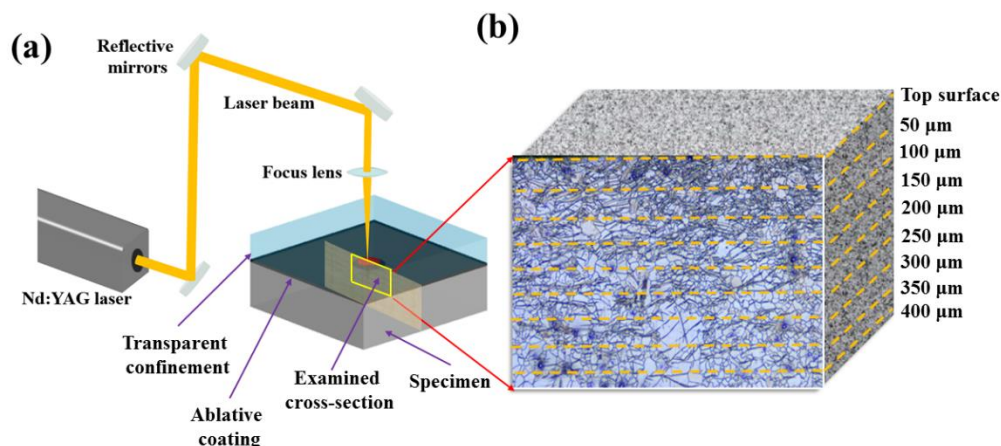
Figure 6.1. Schematic illustrations of (a) the LSP process and (b) preparation of Mg alloy samples with different TVFs.

Tribological properties of the Mg alloy samples were tested using a pin-on-plate sliding configuration using an R-Tech Muti-Functional Tribometer at room temperature in air with a relative humidity of about 20%. The experimental setup is schematically illustrated in Figure 6.2. The cylindrical pin with a hemispherical tip (a diameter of 0.25 inch) was made of an aluminum alloy 6061 (AA6061) with a Vickers hardness of 110 VHN. Dry sliding tests were conducted on the surface of Mg alloy samples with different TVFs. Applied loads of 10, 20, 30, 50 N and a sliding velocity of 2 mm/s were used in the tests. The variation of COF values with sliding distance for each specimen was recorded. After sliding tests, the worn surface morphologies of both the Mg alloy substrate and AA6061 pin were characterized using three-dimensional (3-D) optical profilometer, SEM, and energy dispersive spectroscopy (EDS).
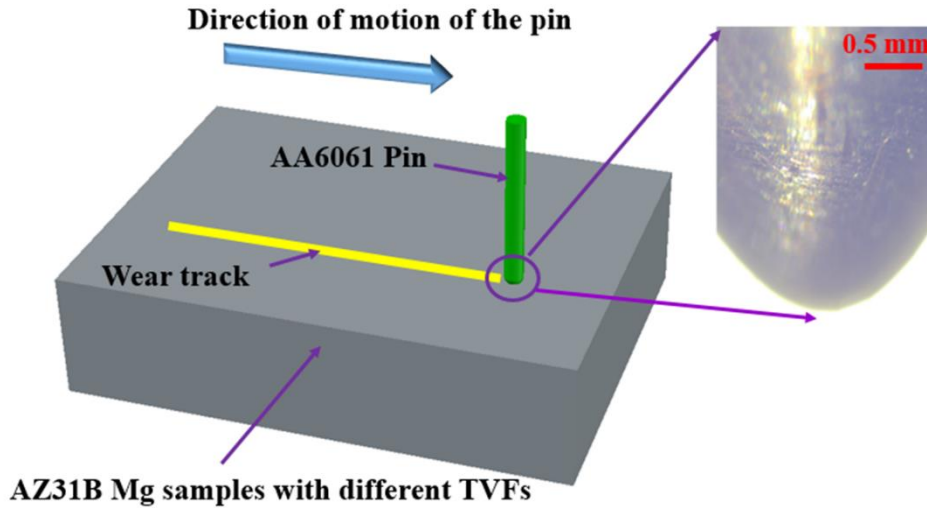
Figure 6.2. Schematic illustration of the pin-on-plate test.

6.3. Results

6.3.1 Gradient twinning microstructure generated by LSP

Figure 6.3a shows gradient twinning microstructure in an AZ31B Mg alloy generated by LSP. The originally equiaxed grains with a strong basal texture now contain a high density of deformation twins that are in a gradient distribution through the thickness can be observed in the top surface layer of the laser-processed sample (as shown in Figure 6.3a). A number of needle-like twin lamellas (with a dark brown color after etching) can be identified in the OM images showing microstructure at a depth of 0, 100, and 150 μm (Figure 6.3b). With the increase of depth, fewer twins can be observed. At the depth of 350 μm, most of the grains contain almost no twins. The TVF can be measured by dividing the area of twins to the overall area by ImageJ software based on color difference between

twins and parents [35]. Figure 6.3c shows TVF vs. depth from the top surface. It can be seen that the TVF decreases from 38% at a depth of 50 μm to 0% at a depth of 350 μm.
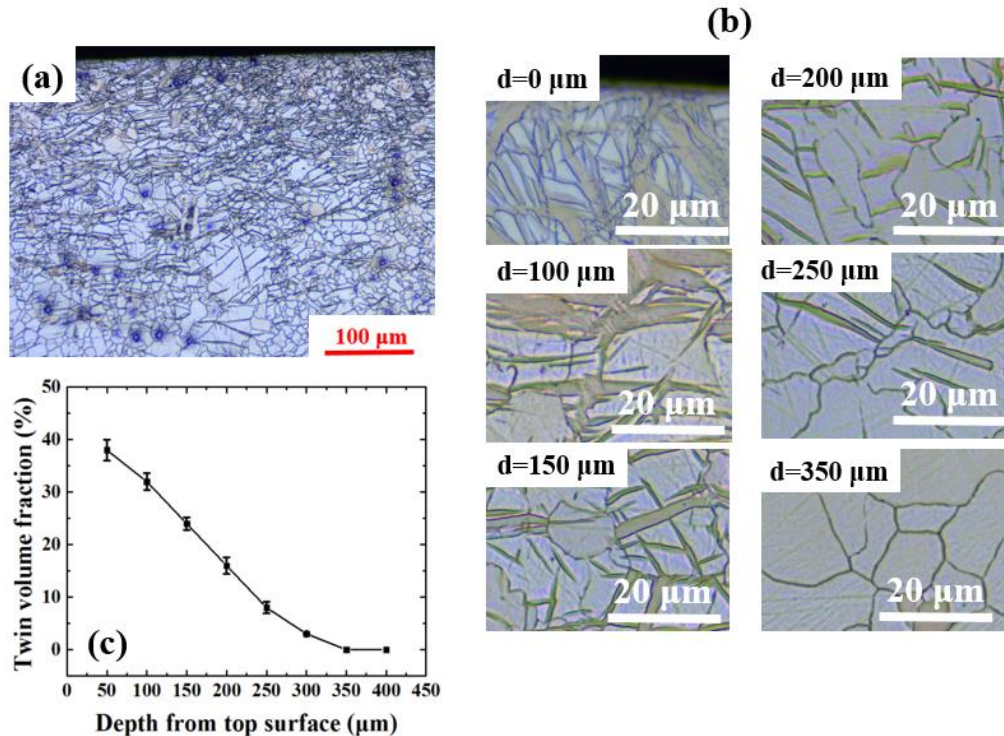
Figure 6.3. Twinning microstructure in an AZ31B Mg alloy generated by LSP: (a) an OM image showing gradient twinning microstructure, (b) OM images showing various TVFs at different depths, and (c) TVF vs. depth from top surface.

EBSD analysis was performed to study the twinning microstructure of laser-processed sample at a depth of 100 μm. The inverse pole figure map in Figure 6.4a shows that a large number of twin lamellas are formed in the parent grains which exhibit a basal texture. The crystallographic orientation of one twin variant and the parent grain in Figure 6.4b shows the misorientation between twin and parent is about 86°, indicating that the twinning type is $\{10\bar{1}2\}\langle10\bar{1}\bar{1}\rangle$ tension twin [90]. Different types of twin boundaries with specific misorientation angles are highlighted by different colors in the image quality map as shown

in Figure 6.4c. The dominant twin boundaries are $86\pm5°\langle11\bar{2}0\rangle$ (in blue) representing $\{10\bar{1}2\}\langle10\bar{1}\bar{1}\rangle$ extension twins. The red twin boundaries (only very few) are $56\pm5°\langle11\bar{2}0\rangle$, representing $\{10\bar{1}1\}\langle10\bar{1}\bar{2}\rangle$ contraction twins. The yellow boundaries are $60\pm5°\langle10\bar{1}0\rangle$, which are generated when different extension twin variants interact. The green boundaries are $38\pm5°\langle11\bar{2}0\rangle$, representing the $\{10\bar{1}1\}+\langle10\bar{1}2\rangle$ double twins. Obviously, the extension twins is the dominant twinning mode. Moreover, $\{0002\}$ pole figure map in Figure 6.4d shows that several twin variants have been activated, which is consistent with results in the previous studies which state that several twin variants could be activated under ultra-high strain-rate deformation [178, 214].
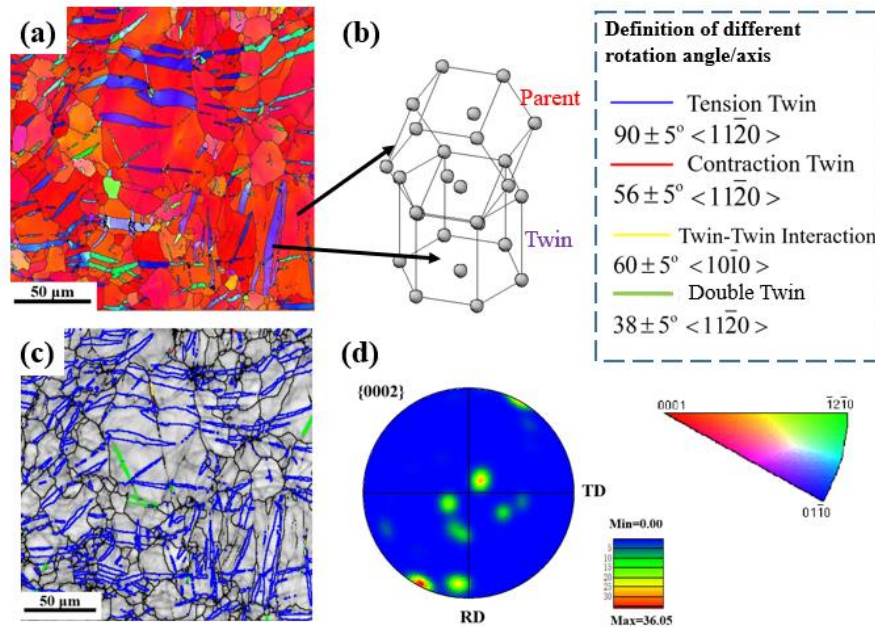
Figure 6.4. EBSD analysis of the microstructure of laser-processed Mg alloy at a depth of 100 μm with a TVF of 30%. (a) Inverse pole figure map; (b) the misorientation between the parent and the twin crystals; (c) Quality map in which different types of twin boundaries are highlighted; (d) $\{0002\}$ pole figure.

6.3.2 Effect of TVF on friction coefficient

Figure 6.5 shows the effect of TVF on the COF as measured by the sliding tests with a load of 20 N and a sliding velocity of 2 mm/s. Figure 6.5a and b show COFs with sliding distance for the samples with a TVF of 0% and 38%, respectively. It is found that the value of COF more or less remains constant with sliding distance for both samples. Moreover, with an increase of TVF from 0% to 38%, the mean value of COF is decreased by around 50% from 0.148 to 0.072. Figure 6.5c shows that the friction value gradually decreases with the increase of TVF. For instance, the COF values for the samples with a TVF of 8% and 24% are 0.135 and 0.112, respectively. The experimental results in Figure 6.5 indicate that the friction performance of Mg alloy is highly affected by the twinning microstructure in terms of TVF.
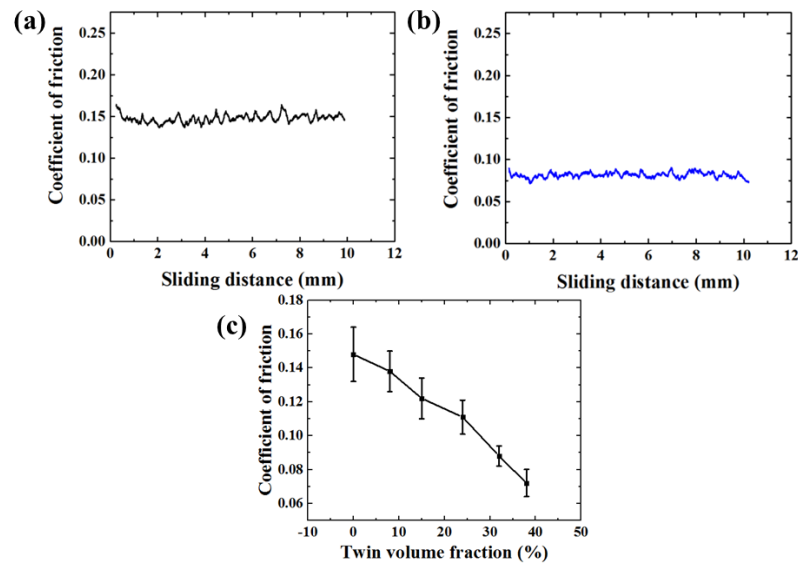
Figure 6.5. Effect of TVF on the COF of Mg alloy samples in sliding tests under the load of 20 N. (a) and (b), COFs of samples with TVF of 0% and 38%, respectively; and (c) COF vs. TVF.

6.3.3 Effect of TVF on wear performance

The 3-D profiles of the worn surface of the AZ31B Mg alloy with different TVFs after sliding tests under an applied load of 20 N are presented in Figure 6.6a-d. It can be seen the wear tracks are composed of grooves along the sliding direction. Material is displaced to the two sides of the wear tracks due to the plowing effect during dry sliding. To quantitatively compare the effect of TVF on the wear performance of AZ31B Mg alloys, cross-sectional profiles of the worn surfaces of the samples with different TVFs are summarized in Figure 6.6e. It is found that the average wear track depth decreases with the increase of TVF. For instance, the wear track depths are around 1.76 and 0.55 μm for the sample with a TVF of 0% (free of twins) and 38%, respectively. This indicates the wear volume has been significantly reduced by the presence of high density extension twins. Moreover, it is found that the height of the material displaced to the sides of wear track for the sample with a TVF of 0% (0.4 μm) is much larger than that of the sample with a TVF of 38% (0.15 μm), demonstrating a stronger plowing effect during the sliding test for the sample with a lower TVF.
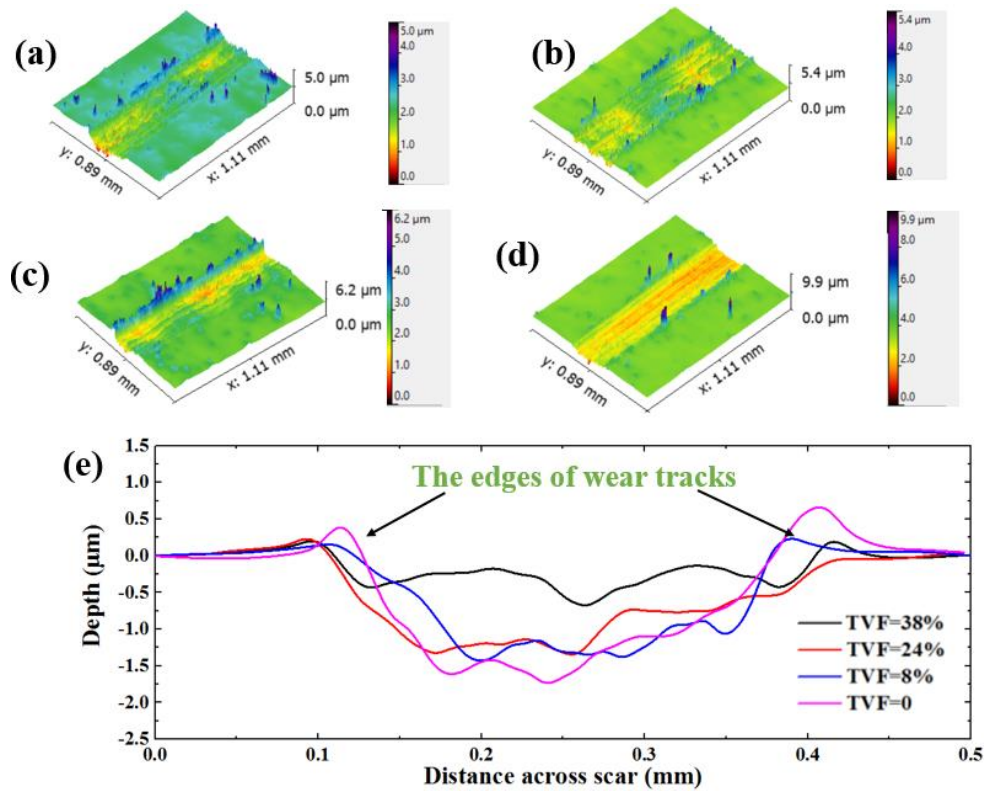
Figure 6.6. Surface profiles of wear tracks of the samples with different TVFs subjected to sliding tests under an applied load of 20 N: (a) TVF=38%, (b) TVF=24%, (c) TVF=8%, and (d) TVF=0 (free of twins); and (e) cross-sectional profiles of the worn surfaces of the samples with different TVFs.

Wear rates of samples with different TVFs as affected by applied loading in the sliding tests are shown in Figure 6.7. It can be seen that the wear rate increases with the increase of applied loading for all samples. For instance, as the load increases from 10 to 50 N, the wear rate increases from 9.24×10^{-5} to 82.15×10^{-5} mm^3/cm·N for the sample with a TVF of 0%. Since AA6061 pin has a much higher surface micro-hardness as compared to Mg alloys, increasing applied load causes a higher degree of plowing of softer counterpart [198]. Moreover, the wear rate decreases as the TVF increases at all loading circumstances. For example, given the applied loading of 50 N, the wear rate is reduced by 58% from

82.15×10^{-5} to 31.32×10^{-5} $mm^3/cm·N$ as the TVF increases from 0% to 38%. Figure 6.6

and 6.7 demonstrate the effect of TVF on the enhanced wear resistance of Mg alloy.
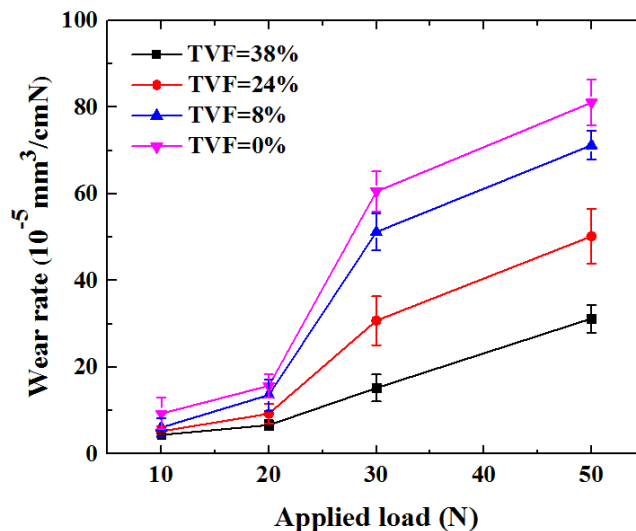
Figure 6.7. Wear rates of samples with different TVFs as affected by applied loading in
the sliding tests.

6.4. Discussion

6.4.1. Effect of deformation twinning on friction

The COF has two components, i.e. the adhesion component and the plowing component.
The adhesion component depends on the material pair, lubrication and also on the real area
of contact, while the plowing component depends on the "degree of plastic deformation"
taking place at the asperity level [215-217]. The twin-induced surface hardening effect is
expected to change the real area of contact and the degree of plastic deformation and thus
influence the COF between the AA6061 pin and Mg alloy as a function of TVF [218].

To understand the effect of deformation twinning on the COF, Vickers micro-hardness
tests were conducted on the surface of Mg alloy samples with different TVFs, as shown in

Figure 6.8. The hardness value of the AA6061 pin is also indicated in the figure for comparison. It can be seen that the micro-hardness value of Mg sample gradually increases with the TVF. For instance, the Vickers hardness number (VHN) increases from 62 to 72 VHN as the TVF increases from 8% to 38%. The twinning-induced hardening of Mg alloys has been reported by several studies [162, 219, 220] and two mechanisms are assumed to be responsible for the improved hardness. The first mechanism is dynamic Hall-Petch effect. Twins subdivide the parent grains and induce a grain refinement effect [219]. The other is texture hardening. The presence of twins can change the surface crystallographic texture as $\{10\bar{1}2\}\langle10\bar{1}\bar{1}\rangle$ twinning reorients the parent lattice by nearly 90° (Fig. 4). Thus, the orientation of the parent grains is changed from an easy-to-deform direction to a difficult-to-deform direction [165]. As the surface hardness of Mg alloy increases with the increase of TVF, the hardness difference between the tribo-pair of AA6061 pin and Mg alloy substrate decreases. This means that the plowing of AA6061 pin (and thus the frictional force) in the Mg sample decreases with the increase of TVF. Therefore, a higher TVF in Mg alloys lead to a lower COF.
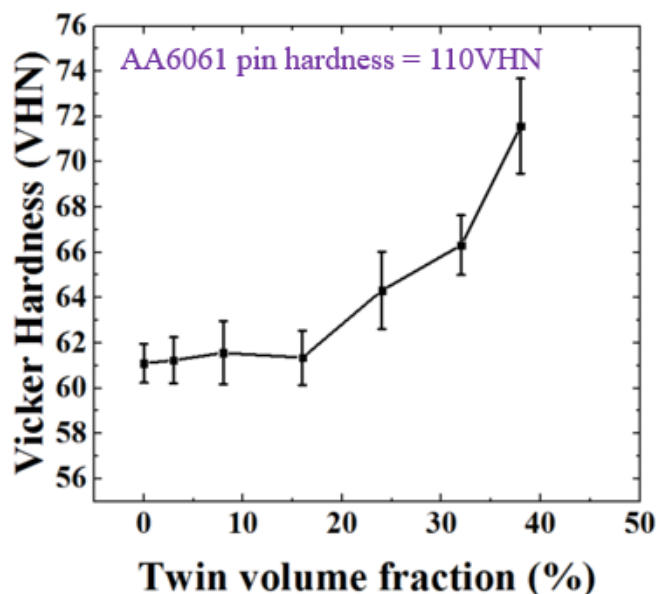
Figure 6.8. Variation of surface micro-hardness values of Mg alloy samples with TVF. The hardness value of AA6061 pin is also indicated in the figure for comparison.

6.4.2. Effect of deformation twinning on wear

To study the effect of deformation twinning on the wear behavior of Mg alloys, the worn surfaces after sliding tests were analyzed by SEM. Figure 6.9 shows micrographs and EDS analysis of the worn surfaces for the samples with a TVF of 0% or 38% after sliding tests under the load of 20 N. Large numbers of grooves on the wear tracks along the scratch direction can be observed in Figure 6.9a and c. The width of the wear track for the sample with a TVF of 0% is around 297 μm, which is wider than that of the sample with a TVF of 38% (253 μm in width). Moreover, the higher magnification image (Figure 6.9c) of the sample with 0% TVF indicates that there are coarse wear debris and delamination damage on the worn surfaces. In contrast, the size of wear debris on the worn surface of the sample with 38% TVF is much finer as shown in Figure 6.9d, and no apparent

delamination can be observed. The EDS analysis shows that the chemical compositions of the wear debris in both samples are mainly magnesium and oxygen. According to the wear mechanism of Mg alloys as discussed in [106, 202, 204, 221, 222], the dominant wear mechanisms in the current study are abrasion together with delamination and oxidation. When the aluminum pin slides against the Mg alloy substrate, the softer counterpart (Mg alloy) is subjected to wear and oxidation due to the plowing and frictional heating [221, 223]. More importantly, by comparing the width of wear tracks (Figure 6.9a and c) and the size of wear debris (Figure 6.9b and d), it can be concluded that both the abrasive wear and delamination wear in AZ31B Mg alloy have been significantly reduced by increasing the TVF.
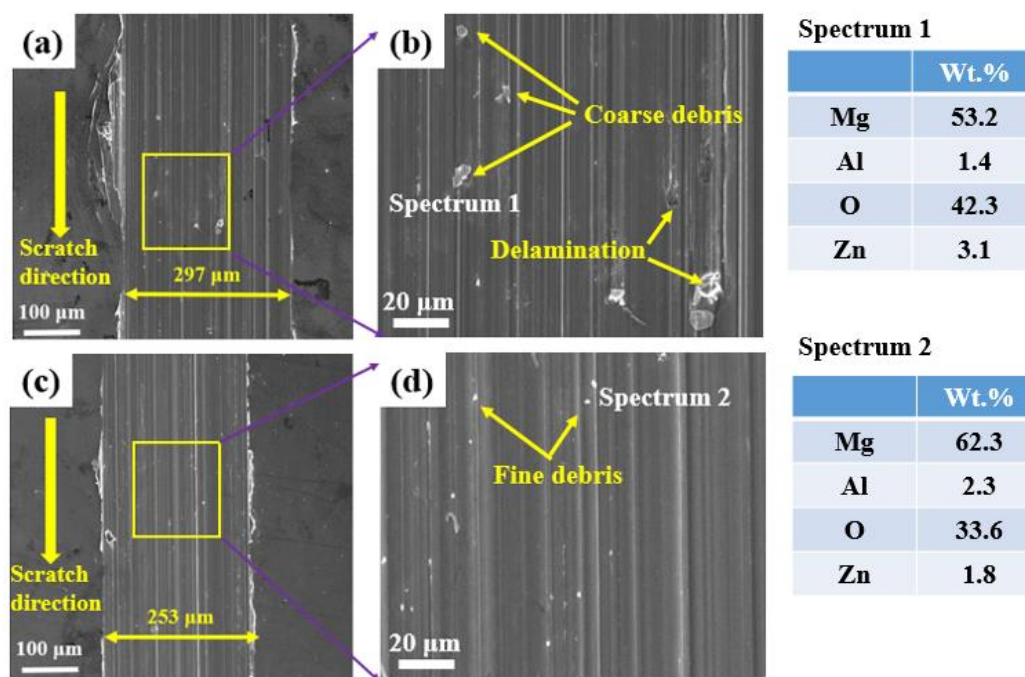
Figure 6.9. SEM images and EDS analysis of worn surfaces of samples with a TVF of (a) 0% and (c) 38%; images (b) and (d) correspond to the locally enlarged figures for (a) and (c) ; and spectrum 1 and 2 correspond to the wear debris in (b) and (d), respectively.

The contact surfaces of the AA6061 pins were also examined by EDS phase mapping. Figure 6.10a-c and Figure 6.10d-f show the results for the Al, Mg, and O signals on the tip surfaces of the AA6061 pins after sliding against the Mg alloy substrates with TVF of 0% and 38%, respectively.   The scratching tests were conducted with a normal load of 20 N. It can be seen that a substantial amount of Mg was transferred to the AA6061 pin surfaces in both cases, and the contact area of Mg is consistent with the width of the wear tracks in Figure 6.9. Moreover, oxidation is involved during the sliding process, as shown in Figure 6.10 c and f. The amount of Mg and O elements observed in Fig. 10e and 10f are lower than that in Figure 6.10b and c, indicating the sample with a TVF of 38% exhibits a greater wear resistance (less plowing) as compared to the sample with free of twins.
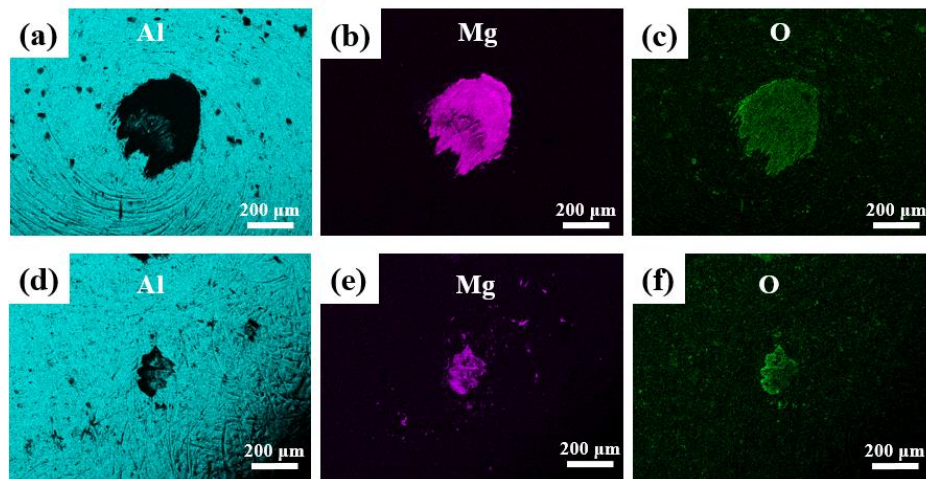
Figure 6.10. EDS phase mapping results of the (a, d) Al signal, (b, e) Mg signal, and (c, f) O signal for the tip surface of the Al pins after sliding against the Mg alloy substrates with free of twins (a, b, c) and with a TVF of 38% (d, e, f).

According to the Archard's law [224], the relationship between the hardness of the wear volume can be described as: $V = \dfrac{LkW}{H}$, where V is the wear volume, L is the sliding

distance, W is the normal load, H is the hardness of the softer material in the contacting pair, and k is the wear coefficient. Given the twinning-induced hardening effect, the wear volume is expected to be reduced substantially by the presence of twins. It can be seen that although the wear depth is more than three times for the surface with free of twins as compared to the surface with a TVF of 38%, the hardness is improved only by 16.1%. This indicates that apart from the improved surface hardness by the presence of twins, other factors such as twinning-induced surface crystallographic texture change [165] might also contribute to the enhanced wear resistance.

6.4.3. The mechanism of improved tribological properties of Mg alloys by LSP

To reveal the mechanism of the effect of TVF on the tribological behavior of Mg alloys, the subsurface microstructure of Mg alloy samples (TVF= 0% and 38%) before and after sliding tests were characterized using SEM and EBSD. As shown in Figure 6.11, the sample free of twins exhibits the microstructure prior to deformation in which no twin can be identified. After the sliding test, a wear track is generated on the sample surface (Figure 6.11c). Figure 6.11b shows the microstructure of sample with TVF of 38%. After the sliding test, a wear track is also observed (Figure 6.11d). EBSD analysis was carried out to study the microstructure beneath the wear tracks of the samples after sliding tests. The inverse pole figure maps for samples TVF of 0% and 38% are shown Figure 6.11e and f, respectively. The corresponding {0002} pole figure maps are shown in Figure 6.11g and h. For the sample without twins, it can be observed in Figure 6.11e that an area with high density twins (TVF is estimated to be around 80%) beneath the wear track is revealed after sliding tests. The nucleation and growth of the twins beneath the wear track is caused by

the plastic deformation induced by the penetration of the AA 6061 pin to the Mg alloy substrate. Similar observations were reported by Liang et al. [208]. For the sample with a TVF of 38%, TVF dramatically increases to almost 100% after sliding tests (Figure 6.11f), indicating that the occurrence of extensive twin-growth activities till twin saturation. Note that the samples free of twins exhibit a strong basal texture as shown in our previous study [148]. The {0002} pole figures in Figure 6.11g and h imply that the crystallographic texture of the microstructure has been significantly changed with the growth and saturation of twins during sliding tests. This twin growth and saturation and twinning-induced surface crystallographic texture change during sliding motion of Mg alloys might contribute to the change of COF and wear resistance.
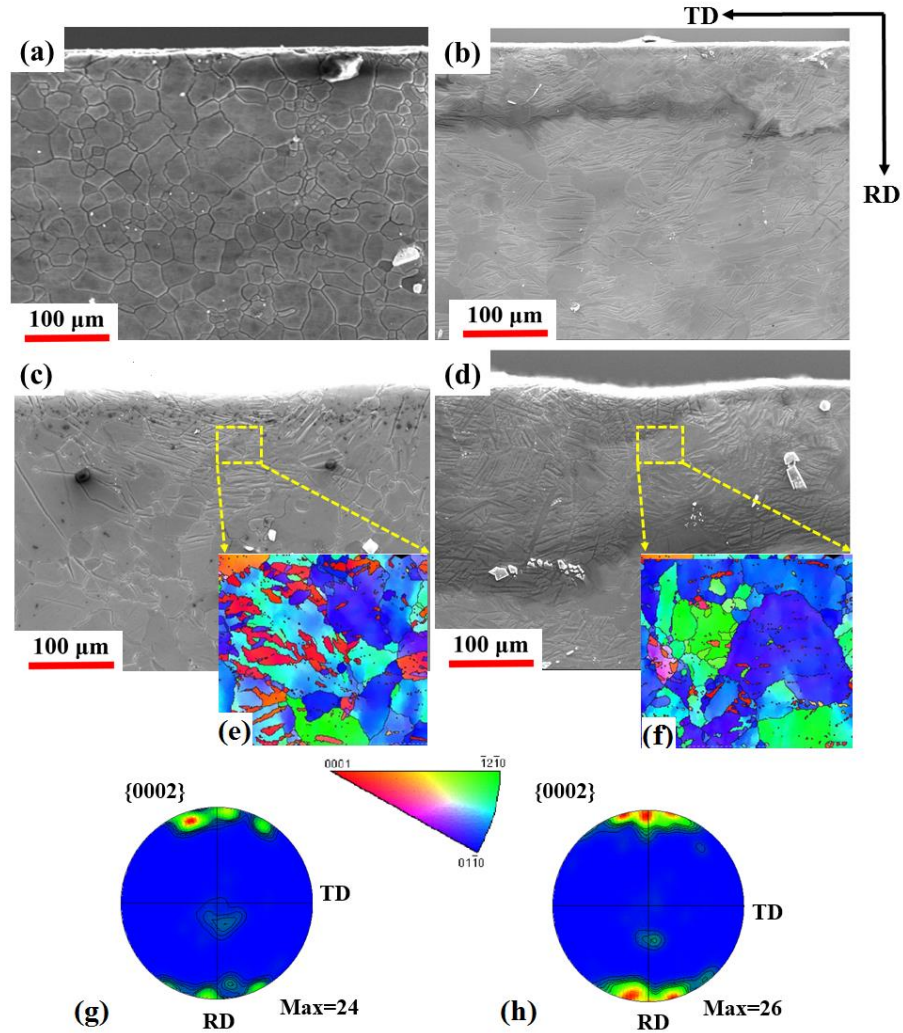
Figure 6.11. SEM images of microstructure of samples with a TVF of 0% and 38% before (a and b) and after (c and d) sliding tests, respectively; EBSD analysis of the microstructure beneath the wear track: inverse pole figure maps and {0002} pole figure maps of samples with a TVF of 0% (e and g) and 38% (f and h) after sliding tests, respectively.

Based on the above analysis and discussion, the mechanism responsible for the influence of TVFs on COF and wear resistance of Mg alloy is proposed and schematically illustrated in Figure 6.12. Figure 6.12a-b and c-d show the contacting and sliding conditions between tribo-pair of AA6061 pin and AZ31 substrate with a low TVF and a

high TVF, respectively. The red hexagons represent the grains prior to deformation (Figure 6.12a) which have a strong basal texture, and the blue lamellas (Figure 6.12c) represent the pre-existing twins introduced by LSP processing before sliding. The blue hexagons (Figure 6.12d) and green lamellas (Figure 6.12b and d) represent the fully twinned grains and newly developed twins in the sliding tests, respectively. As shown in Figure 6.12b, twinning is responsible for the plastic deformation of the substrate when the AA6061 pin is penetrated into it. However, for the sample with a high TVF (Figure 6.12c), subsequent twinning (growth of pre-existing twins and nucleation of new twins) occurs until the microstructure near the wear track is fully twinned (Figure 6.12d). Non-basal slip systems with higher critical resolved shear stresses need to be activated to accommodate further plastic deformation during sliding (Figure 6.12d) [225, 226]. Therefore, the penetration depth and the contacting area of the aluminum pin against the substrate in Figure 6.12d are smaller than those in Figure 6.12b. As a result, the plowing effect in Mg alloy samples with a high TVF (Figure 6.12d) is weaker than that in samples with a low TVF (Figure 6.12b), resulting in a lower COF and reduced wear volume [63, 227, 228]. Similarly, for samples with a higher TVF, saturation of twinning and activation of non-basal slip should occur earlier than that for samples with a lower TVF, leading to a more prominent effect in reducing the COF and enhancing the wear resistance.
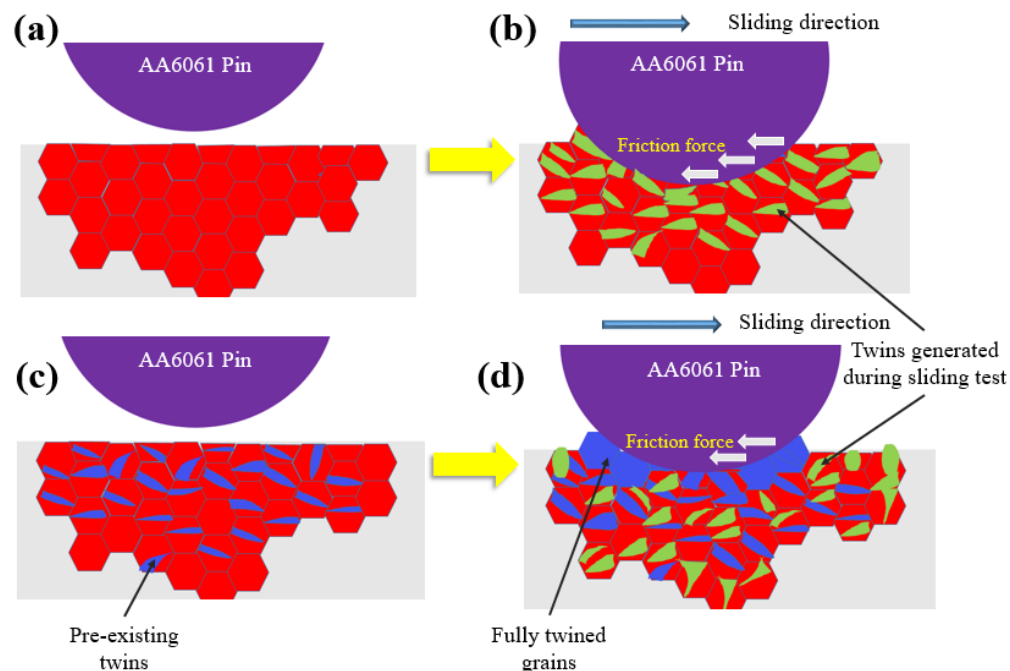
Figure 6.12. Schematic illustration of proposed mechanism responsible for the influence of TVFs on COF and wear resistance of Mg alloy: AA6061 pins sliding against the surfaces of Mg alloy with (a, b) a low TVF and (c, d) a high TVF.

6.5. Summary

In this chapter, the influence of surface pre-twinning induced by LSP on the tribological performance of an AZ31B Mg alloy is investigated. Sliding tests are performed on surfaces with different TVFs under dry condition. The microstructure of the worn surface and subsurface of Mg alloy samples after sliding tests are characterized and analyzed. The relationships among the TVF, COF, and wear resistance are discussed. Following conclusions can be drawn:

(1) Pre-twinning introduced by LSP on Mg alloys can bring a surface hardening effect. A higher TVF results in a greater surface hardness number due to the twinning-induced hardening effect.

(2) The COF decreases with the increase of TVF in Mg alloy samples.

(3) The wear resistance increases with the increase of TVF in Mg alloys.

(4) Twin growth/saturation and twinning-induced crystallographic texture change are observed beneath the wear track of Mg alloy samples after sliding tests.

(5) The mechanism responsible for the influence of pre-twinning on COF and wear resistance of Mg alloy is proposed. It is discussed that the reduced COF and enhanced wear resistance of Mg alloy with increase of TVF are attributed to the twinning-induced hardening effect, twin growth and saturation phenomenon, and twinning-induced surface crystallographic texture change during the sliding.

Chapter 7. Enhanced room temperature stretch formability of Mg alloys by LSP

7.1. Introduction

In recent years, LSP emerges as a promising technology to improve the engineering performance of Mg alloys by enhancing their surface strength [148] , biocompatibility [229], fatigue life [56], tribological performance [211] and corrosion resistance [57]. Compared with processing methods mentioned above, LSP is exceptional due to its capability of processing samples with complex geometries and generating deep plastic deformation without degrading the surface quality [11, 53]. The previous chapters indicate that LSP of Mg alloys leads to the generation of a high density of $\{10\bar{1}2\}$ extension twins, leading to a crystallographic lattice orientation of 86.3° around $\langle 1\bar{2}10 \rangle$ zone axis [35, 182]. The lattice reorientation induced by pre-twinning provides an approach to tailor the basal texture of Mg alloys [210, 230]. In addition, grain refinement by LSP of metallic materials has been extensively reported [56, 155, 212]. All these findings indicate that LSP could potentially enhance the formability of Mg alloys.

In this study the applicability of LSP to improve the room-temperature stretch formability of Mg alloy sheet is investigated. LSP experiments were conducted on an AZ31B Mg alloy. The microstructure was characterized using optical microscopy (OM) and EBSD microscopy. Erichsen tests were carried out to evaluate the stretch formability. The results show that LSP can provide a combined texture weakening and grain refinement, leading to improved room-temperature stretch formability of the Mg alloy sheet. Notably, this part of content is basically adapted from [231] (with permission from publisher).

7.2. Experiments

A schematic of the setup of the LSP process is shown in Figure 7.1a. A Q-switched Nd-YAG laser (1064 nm wavelength and 7 ns pulse width), was used to deliver the laser energy. The laser beam diameter was 2 mm. Black tape with a thickness of 100 μm and BK7 glass were used as the ablative coating and transparent confinement, respectively. The LSP scan path is schematically illustrated in Fig. 1b. The distance between two neighboring spots is 1 mm and the overlapping ratio is 39%. LSP was performed along ND to process the whole surfaces of samples. During LSP, the nanosecond pulsed laser energy is absorbed by ablative coating, leading to the generation of a high shockwave pressure (~GPa) propagating into the sample [64, 232]. The temporal evolution of laser shockwave pressure as affected by the laser intensity can be estimated by Fabbro's model [233] (Figure 7.1c). For instance, given a laser intensity of 4GW/cm^2, the peak shock pressure reaches 3.5 GPa.

The room-temperature stretch formability of laser processed samples was evaluated by the Erichsen tests. A schematic configuration of Erichsen test is illustrated in Figure 7.1d. The diameter of the lower mold and upper mold were 15 and 17 mm, respectively. An Instron testing machine was used to control the forming speed and record the load vs. displacement behavior. The forming load was applied on a hemispherical shape punch with a diameter of 10 mm at a constant speed of 0.01 mm/s. The movement of the punch stopped as cracks initiated (indicated by a 10% drop of the maximum load) on the lower surface (LSP processed surface) of the sample. The values of limit dome height (LDH), i.e., stretch formability, defined as the depth of the punch at fracture initiation, were then measured. To investigate the effect of LSP on the mechanical properties of Mg alloys,

tensile tests were carried out using the "dog-bone" samples with a gauge area of 16 mm (RD) by 6 mm (TD) and a thickness of 2 mm (ND) machined from the Mg block, as shown in Figure 7.1e. Both sides of the gauge area of the samples subjected to tensile tests were LSP processed. The strain rates were set as 0.0005/s in the tensile tests.
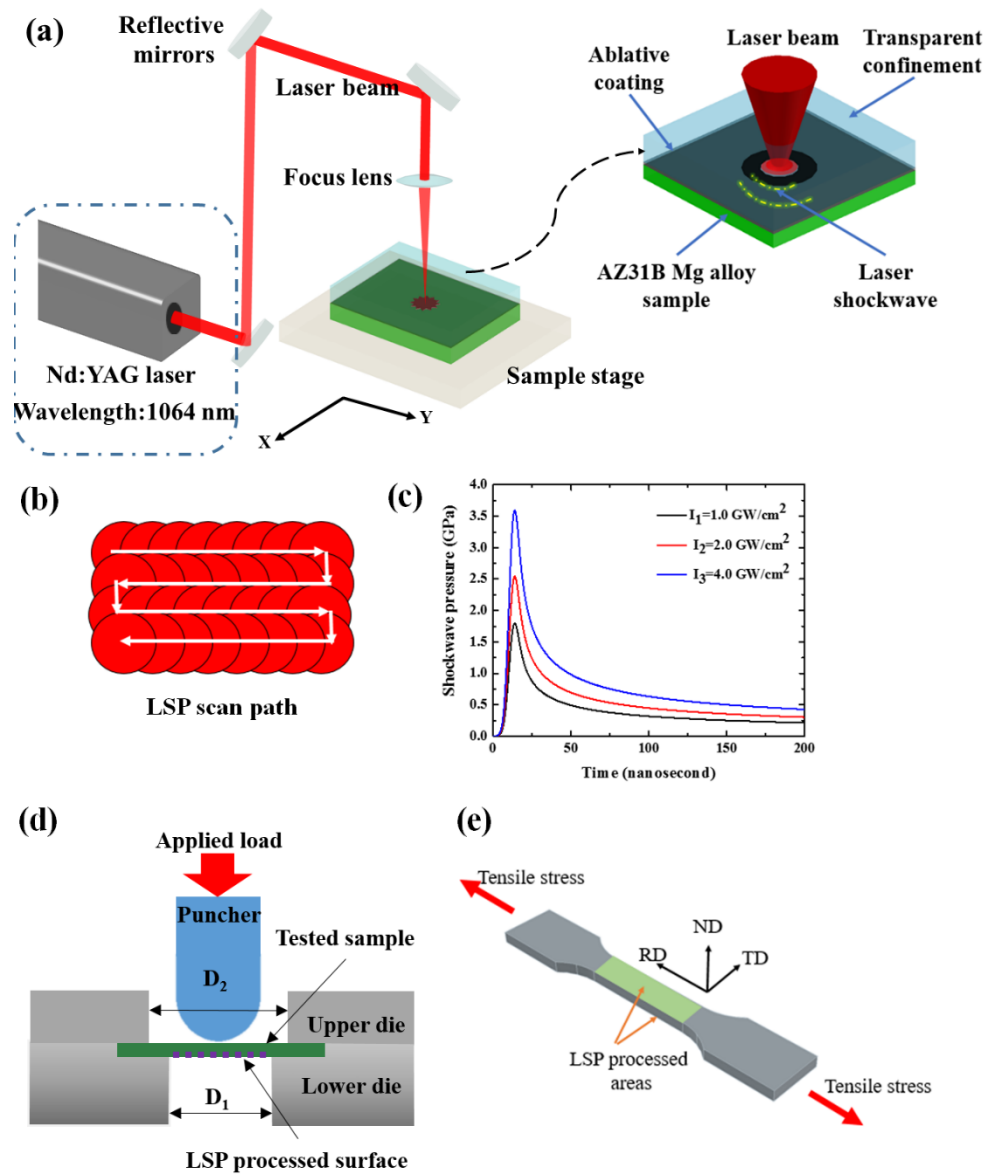
Figure 7.1. (a) Schematic setup of the LSP process. (b) LSP scan path. (c) The temporal evolution of laser shockwave pressure as affected by the laser intensity in LSP

experiments, estimated by Fabbro's model. Schematic configurations of the (d) Erichsen

test and (e) tensile test.

7.3. Results and discussion

7.3.1. Improved stretch-formability of Mg alloys by LSP

Results of the Erichsen tests are shown in Figure 7.2a-b. As observed in the load vs.

displacement curves (Figure 7.2a), LSP enhances stretch formability of Mg alloy sheet.

As compared to the unprocessed sample, a lower load is needed for processed samples to

reach the same displacement. For instance, to reach a deformation displacement of 1.0 mm,

the load for sample processed by LSP with a laser intensity of 1.0 GW/cm^2 is 310 N, which

is only 48% of the load used for unprocessed sample (650 N). In addition, the enhanced

stretch formability is confirmed by the side view of the samples after Erichsen tests (Figure

7.2b). It can be seen that the processed samples exhibit a higher value of LDH as compared

to the unprocessed one. For instance, the unprocessed sample has a LDH value of 1.67

mm, whereas for the sample processed by LSP with a laser intensity of 4.0 GW/cm^2, the

LDH value increases by 63% to 2.73 mm. Moreover, a higher laser intensity results in a

higher LDH value. The value of LDH increases from 2.21 to 2.73 mm as the laser intensity

increases from 1.0 to 4.0 GW/cm^2.

Tensile testing results are shown in Figure 7.2c. It is observed that the yield strength

and ultimate tensile strength (UTS) of LSP processed samples are lower than those of the

unprocessed one, while the fracture elongation (FE) of LSP processed samples are greater

than that of the unprocessed one. Moreover, both the UTS and FE increase with the

increase of laser intensity. For instance, as the laser intensity increases from 1.0 to 4.0

GW/cm^2, the UTS increases from 212 to 241 MPa, and the FE increases from 10.5% to 13.8%.
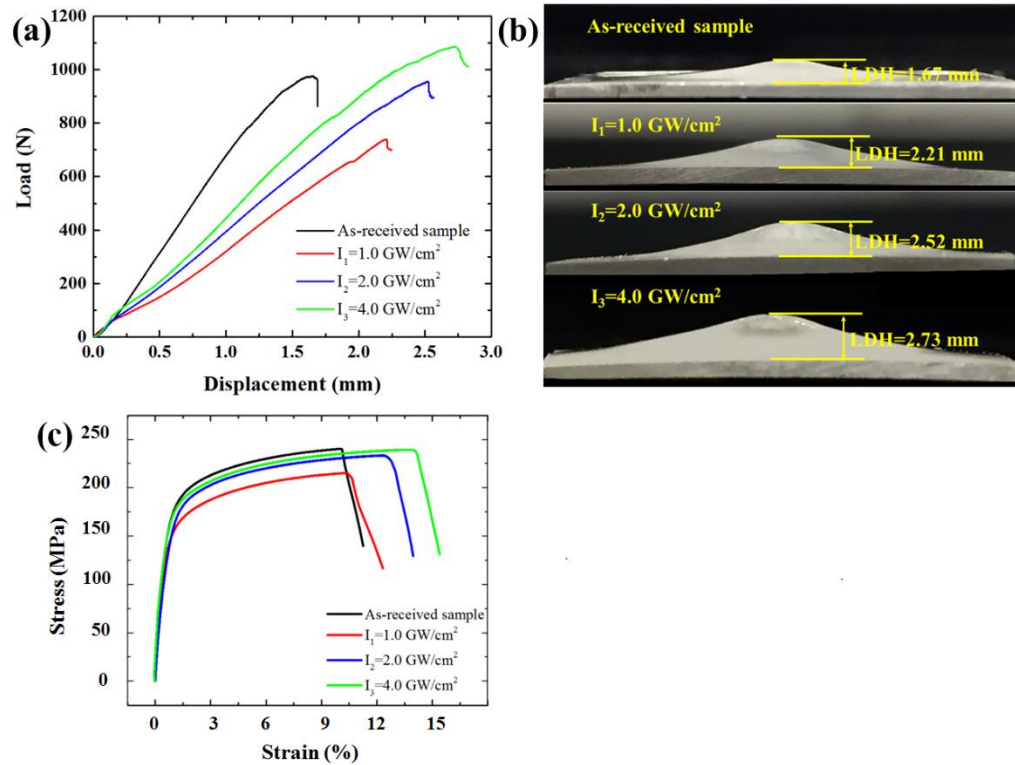
Figure 7.2. (a) Load vs. displacement curves of unprocessed and LSP processed Mg alloy samples in the Erichsen tests. (b) Side view of the Mg alloy samples after Erichsen tests. (c) Tensile stress-strain curves of unprocessed and LSP processed Mg alloy samples.

7.3.2. Texture evolution during LSP

To reveal the mechanism responsible for the enhanced formability of Mg alloys by LSP, EBSD analysis was performed. The inverse pole figure (IPF) maps, image quality maps, and pole figure maps of the surface of the unprocessed and processed samples are presented in Figure 7.3a-d. It can be seen that the unprocessed sample exhibits a strong basal texture together with a twin-free equiaxial grain structure (Figure 7.3a). After LSP, a high density

of twin lamellas, mostly identified as $\{10\bar{1}2\}\langle10\bar{1}1\rangle$ extension twins (Figure 7.3b-d), were generated. A higher laser intensity leads to a higher twin volume fraction (Figure 7.3b-d). As an evidence of texture weakening effect, the pole figure maps show that the $\{0002\}$ poles spread along the RD after LSP and this trend becomes more apparent as the laser intensity increases due to the increase of twin volume fraction. Note that, the appearance of high density $\{10\bar{1}2\}$ twins in this study seems abnormal since its activation is most favorable when a tensile stress is applied along the c-axis or a compressive stress is applied perpendicular to the c-axis of Mg crystals [30]. In this study where a compressive stress is applied along c-axis, the activation of $\{10\bar{1}2\}$ twins should be suppressed (Figure 7.3e). To address this paradox, single pulse LSP experiment with a laser intensity of 2.0 GW/cm^2 and a beam diameter of 2.0 mm was conducted on Mg alloy samples along ND. The microstructure of the processed surface was examined by OM (Figure 7.3f-g). A donut-like distribution of twins can be identified in Figure 7.3f, where the twinning zone is marked between the yellow and red dash lines. The twinned zone is located along the perimeter of laser processed area (Figure 7.3f), while few twins can be found in the center area with a diameter equal to the diameter of laser beam (Figure 7.3g). Therefore, in the continuous LSP experiment along ND where the sample surface is completely processed with a laser beam overlapping ratio of 75%, surface twinning with a high density can be achieved (as observed in Fig. 3d), leading to the texture weakening effect.
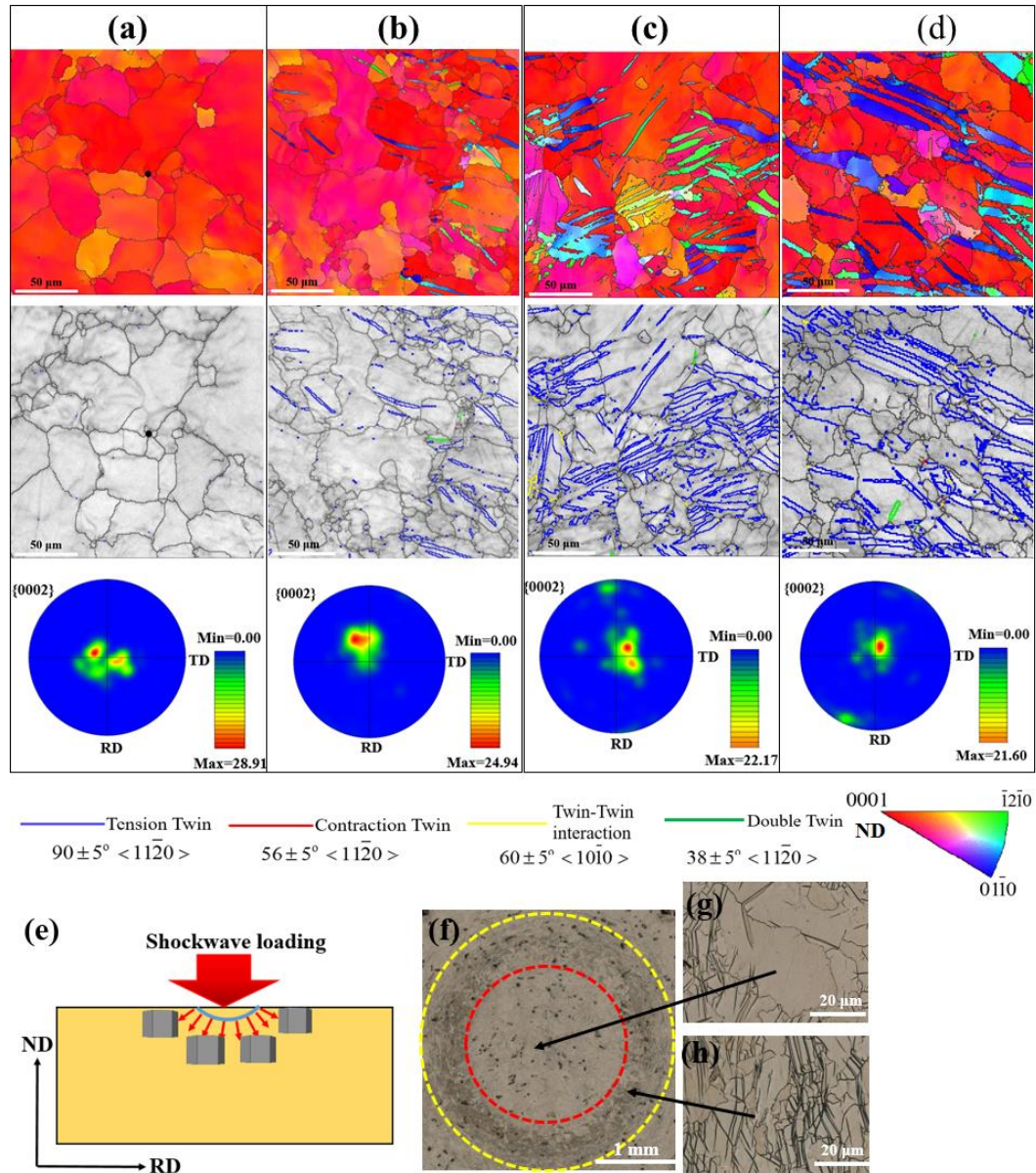
Figure 7.3. EBSD analysis of the surface microstructure (perpendicular to ND) of the Mg alloy samples: (a) As-received sample, and samples processed by LSP with a laser intensity of (b) 1.0 GW/cm^2, (c) 2.0 GW/cm^2, and (d) 4.0 GW/cm^2. (e) Initial texture of the as-received sample and schematic of stress distribution during single pulse LSP. Optical microcopy images of the surface processed by single pulse LSP with a laser intensity of 2.0 GW/cm^2: (f) LSP created a donut-shaped zone. (g) Central area with few twins. (h) Perimetric area with a high density of twins.

7.3.3. Grain refinement effect

In addition, the cross-sectional microstructure (RD-ND plane) at a depth of 300 μm before and after LSP was characterized using EBSD (Figure 7.4). The unprocessed sample (Figure 7.4a) possesses a relatively homogenous distribution of equiaxed grains with a grain size of 20-40 μm, while the processed sample (Figure 7.4b) exhibits a bimodal microstructure containing both coarse and fine grains. Grains with a size of a few microns can be found in Figure 7.4b-c, indicating that the grains were refined to a certain extent after LSP. IPF maps of some local areas with observable grain refinement are shown in Figure 7.4d-h.

The grain refinement of metallic materials by LSP has been reported [56, 155, 212]. It is normally observed in the layer of severe plastic deformation right beneath the processed surface with a thickness of less than 100 μm. However, Figure 7.4b-h demonstrate the grain refinement can occur at a depth around 500 μm in the LSP processed Mg alloys due to recrystallization. Twin lamellas can be identified in Fig. 4b and 4c. The image quality map (Figure 7.4c) shows the dominant twin boundaries are $90 \pm 5°\langle 11\bar{2}0 \rangle$ (blue lines) representing $\{10\bar{1}2\}\langle 10\bar{1}1 \rangle$ extension twins and $38 \pm 5°\langle 11\bar{2}0 \rangle$ (green lines) representing $\{10\bar{1}1\} + \{10\bar{1}2\}$ double twins. It is reported that $\{10\bar{1}2\}$ twins can serve as nucleation sites for dynamic recrystallization (DRX) during hot working [138]. Wang et al. [234] showed that deformation with a high strain rate promoted DRX of Mg alloys due to the elevated activities of deformation twinning. In LSP, the strain rate is as high as 10^6/s and the duration of laser shock loading is as short as 100 ns, the plastic work stored in a confined volume may trigger nucleation and growth of new grains. DRX can be proved

by the misorientation angle distribution of the grain boundaries as shown in Figure 7.4i. The peak intensity at a low misorientation angle of 5° is an indication of the extensive subgrain structures, whereas the misorientation peak at 30° is mainly attributed to the 30° <0001> misorientation relationship during the growth of DRXed grains [235, 236]. In Figure 7.4j, EBSD analysis was used to distinguish the deformed grains, sub-grains, and recrystallized grains, following the method used in [237-239]. Large amounts of subgrains with extensive low angle grain boundaries and several DRXed grains with an average grain size around 3 μm can be identified.
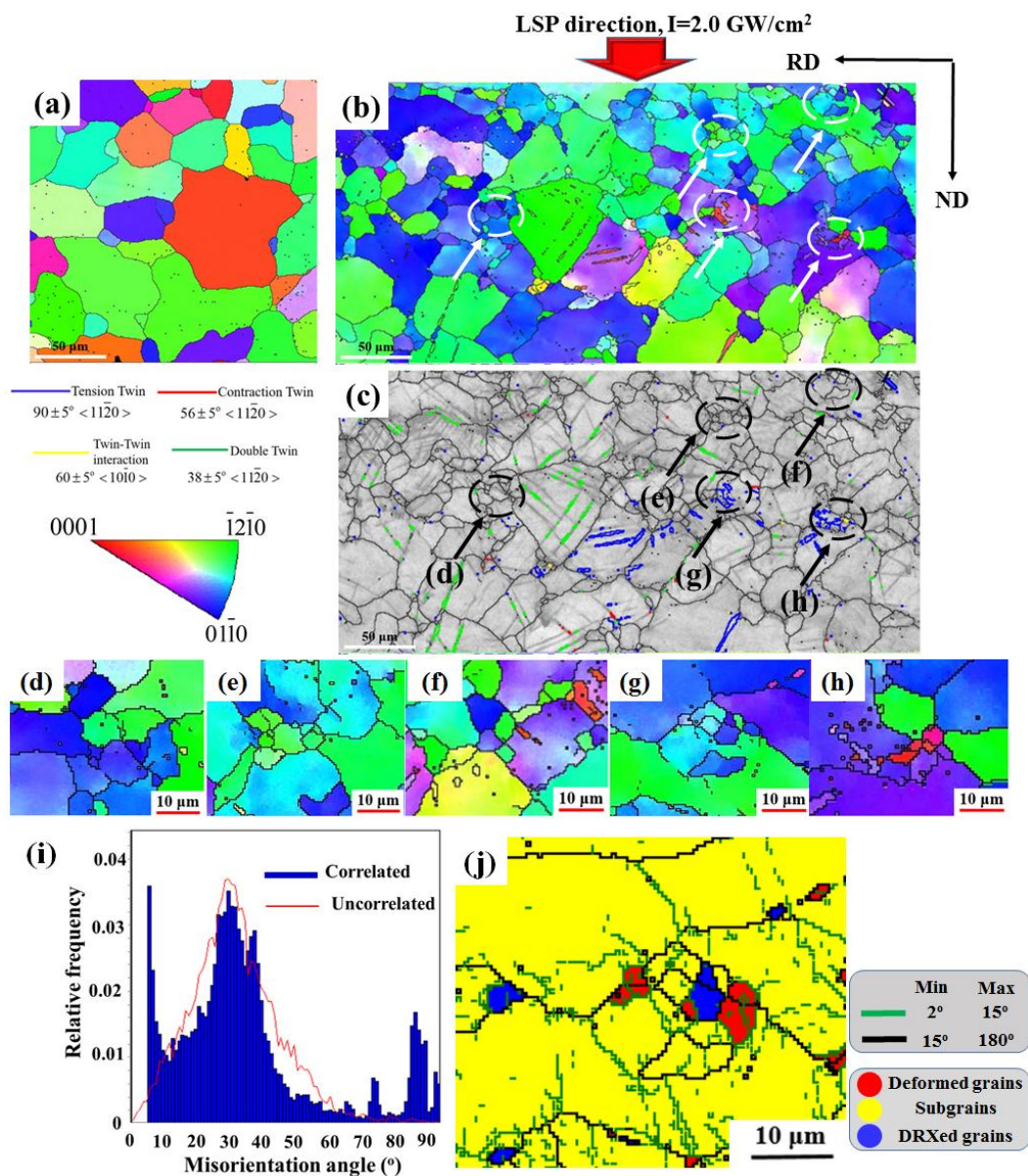
Figure 7.4. EBSD analysis of the cross-sectional microstructure (ND-RD plane) of the Mg alloy samples: (a) IPF map of the as-received sample; (b) IPF map and (c) image quality map of the sample processed by continuous LSP with a laser intensity of 2.0 GW/cm^2; (d)-(h) IPF maps of some local areas showing significant grain refinement. (i) Corresponding misorientation angle distribution for (b). (j) EBSD maps distinguishing the DRXed grains (blue area), subgrains (yellow area), and deformed grains (red area) for (g).

7.3.4. The mechanism of enhanced stretch formability of Mg alloys by LSP

Based on the microstructural analysis, the mechanism responsible for the improved formability of Mg alloys by LSP can be proposed. During the Erichsen test, biaxial tensile stress field is applied on sample sheet [240, 241]. The microstructure of the LSP processed samples is composed of a mixture of parent grains, twinned grains and refined grains. For the parent grains, the compressive strain along the thickness direction activates pyramidal $\langle c + a \rangle$ slip or contraction twinning, whose critical resolve shear stresses are higher than those of $\langle a \rangle$ slip (basal and prismatic) or extension twinning. Therefore, deformation of rolled Mg alloys with a strong basal texture along the thickness direction is difficult, leading to a poor stretch formability. In contrast, for the twinned grains with crystallographic orientation rotated by ~90°, "re-twinning" [230], or "de-twinning" [242] can be activated to accommodate the plastic strain, enabling an easier and more homogenous plastic deformation [243]. For polycrystalline materials, individual crystals deform only along specific crystallographic orientations, thus deformation compatibility among grains is often required to accommodate the macroscopic shape changes [244, 245]. In this regard, the weakened basal texture induced by pre-twinning contributes to the deformation compatibility and improves the stretch formability. Moreover, the refined grains induced by LSP could provide additional plastic deformation modes, i. e., grain boundary sliding (GBS), leading to the improved stretch formability [246]. GBS has been perceived as important approach to realize the superplasticity of metals. Despite that GBS often occurs at elevated temperatures, recent studies [247-249] indicate that it can be activated in Mg alloys at room temperature once the grain size is reduced to one micron or sub-micron, leading to significantly improved formability. In our study, plastic stain can

be accommodated through the above discussed mechanisms. As the laser intensity increases, more refined grains are generated, leading to the decrease of average grain size. As a result, according to the Hall-Petch relationship [250, 251], the grain boundary hardening effect leads to the increase of the stress required for plastic deformation. Therefore, both the loading forces in load-displacement curves (Fig. 2a) and strength levels in stress-strain curves (Fig. 2c) increase with the increase of laser intensity.

7.4. Summary

In this chapter, the enhanced room-temperature stretch formability of Mg alloy sheet by LSP is investigated. The results show the formability of Mg alloys can be increased by 63%. Based on the microstructural analysis, a combination of texture weakening by extension twinning and grain refinement induced by LSP may account for the improved stretch formability of the Mg alloy.

Chapter 8. Conclusions

In this dissertation, the microstructure evolution and enhanced mechanical properties of Mg alloys processed by LSP was investigated. LSP was performed on an AZ31B Mg alloys and the resultant microstructure was analyzed by OM, SEM and EBSD. A particular focus was put on the twinning behavior of Mg alloys during LSP. Surface micro-hardness test, tribological property test, tensile test, and stretch-formability test were carried out to evaluate the mechanical properties enhancement. The following conclusions can be reached:

(1) Deformation twinning, especially $\{10\bar{1}2\}\langle10\bar{1}\bar{1}\rangle$ tension twinning mode, plays an important role during the LSP processing of Mg alloys. A gradient twinning microstructure in which the density of twins decreases with depth was introduced to an AZ31B Mg alloy plate by LSP.

(2). A gradient hardness distribution well corresponds to the gradient twinning microstructure. The hardness of laser-processed samples decreases with an increase of depth from the saturation value of 74 VHN to the base value of 60 VHN. The LSP-induced strain hardening is attributed to the grain refinement and the texture change induced by nucleation and propagation of twinning structures.

(3). Anisotropic microstructural and mechanical response to LSP is observed. High density twins can be observed when LSP is along the RD, whereas some refined grains can be observed when LSP is along the ND. LSP treatment of AZ31B Mg alloys along ND and RD can both enhance the surface hardness.

(4). Twin-twin interactions profusely exist in Mg alloys as processed by LSP. Interfaces between different $\{10\bar{1}2\}$ twin variants shows that these interfaces present abnormal morphologies that cannot be accounted for by twinning dislocation theories. Patches of one variant can be completely surrounded by another variant. Such an abnormal behavior of twin-twin interaction can only be explained by non-twinning-dislocation theories that fundamentally differ from the classical twinning theory.

(5). The tribological performance of Mg alloys is improved by LSP processing. Both the COF and wear rate decrease with the increase of TVF. The improved tribo-performance of Mg alloys by LSP are attributed to the twinning-induced hardening effect, twin growth and saturation phenomenon, and twinning-induced surface crystallographic texture change during sliding.

(6). The room temperature stretch-formability of Mg alloys is improved by LSP. By optimizing the processing parameters, the limit dome height can be increased by 63%. Based on the microstructural analysis, a combination of texture weakening by extension twinning and grain refinement induced by LSP may account for the improved stretch formability of the Mg alloy.

References

[1] Peyre P, Fabbro R, Merrien P, Lieurade H. Laser shock processing of aluminium alloys. Application to high cycle fatigue behaviour. Materials Science and Engineering: A. 1996;210:102-13.

[2] Lu J, Luo K, Yang D, Cheng X, Hu J, Dai F, et al. Effects of laser peening on stress corrosion cracking (SCC) of ANSI 304 austenitic stainless steel. Corrosion Science. 2012;60:145-52.

[3] Sanchez-Santana U, Rubio-Gonzalez C, Gomez-Rosas G, Ocana J, Molpeceres C, Porro J, et al. Wear and friction of 6061-T6 aluminum alloy treated by laser shock processing. Wear. 2006;260:847-54.

[4] Fairand B, Wilcox B, Gallagher W, Williams D. Laser shock‐induced microstructural and mechanical property changes in 7075 aluminum. Journal of Applied Physics. 1972;43:3893-5.

[5] Zelahy JW. Method for repairing a turbomachinery blade tip. Google Patents; 1980.

[6] Faber G, Maggi C. Blade construction for axial-flow turbo-machines and method of protecting turbo-machine blades against stress corrosion cracking. Google Patents; 1974.

[7] Liao Y, Ye C, Cheng GJ. [INVITED] A review: Warm laser shock peening and related laser processing technique. Optics & Laser Technology. 2016;78:15-24.

[8] Liao Y, Suslov S, Ye C, Cheng GJ. The mechanisms of thermal engineered laser shock peening for enhanced fatigue performance. Acta Materialia. 2012;60:4997-5009.

[9] Shukla PP, Swanson PT, Page CJ. Laser shock peening and mechanical shot peening processes applicable for the surface treatment of technical grade ceramics: a review. Proceedings of the Institution of Mechanical Engineers, Part B: Journal of Engineering Manufacture. 2014;228:639-52.

[10] Nalla R, Altenberger I, Noster U, Liu G, Scholtes B, Ritchie R. On the influence of mechanical surface treatments—deep rolling and laser shock peening—on the fatigue behavior of Ti–6Al–4V at ambient and elevated temperatures. Materials Science and Engineering: A. 2003;355:216-30.

[11] Peyre P, Fabbro R. Laser shock processing: a review of the physics and applications. Optical and quantum electronics. 1995;27:1213-29.

[12] Xu Y, Du Z, Ruan L, Zhang W. Research status and development of laser shock peening. Journal of Laser Applications. 2016;28:022508.

[13] Ruschau JJ, John R, Thompson SR, Nicholas T. Fatigue crack nucleation and growth rate behavior of laser shock peened titanium. International Journal of Fatigue. 1999;21:S199-S209.

[14] Pollock TM. Weight loss with magnesium alloys. Science. 2010;328:986-7.

[15] Friedrich HE, Mordike BL. Magnesium technology: Springer; 2006.

[16] Frankel GS. Magnesium alloys: ready for the road. Nature materials. 2015;14:1189.

[17] Wu S, Ji Z, Zhang T. Microstructure and mechanical properties of AZ31B magnesium alloy recycled by solid-state process from different size chips. Journal of Materials Processing Technology. 2009;209:5319-24.

[18] Lee S, Ham HJ, Kwon SY, Kim SW, Suh CM. Thermal conductivity of magnesium alloys in the temperature range from− 125 C to 400 C. International Journal of Thermophysics. 2013;34:2343-50.

[19] Bettles C, Gibson M. Current wrought magnesium alloys: strengths and weaknesses. JOM Journal of the Minerals Metals and Materials Society. 2005;57:46-9.

[20] Polmear I. Magnesium alloys and applications. Materials Science and Technology. 1994;10:1-16.

[21] Mehta D, Masood S, Song W. Investigation of wear properties of magnesium and aluminum alloys for automotive applications. Journal of Materials Processing Technology. 2004;155:1526-31.

[22] Staiger MP, Pietak AM, Huadmai J, Dias G. Magnesium and its alloys as orthopedic biomaterials: a review. Biomaterials. 2006;27:1728-34.

[23] Chen L-Y, Xu J-Q, Choi H, Pozuelo M, Ma X, Bhowmick S, et al. Processing and properties of magnesium containing a dense uniform dispersion of nanoparticles. Nature. 2015;528:539.

[24] Ono N, Nowak R, Miura S. Effect of deformation temperature on Hall–Petch relationship registered for polycrystalline magnesium. Materials Letters. 2004;58:39-43.

[25] Agnew S. Plastic anisotropy of magnesium alloy AZ31B sheet. Essential Readings in Magnesium Technology: Springer; 2016. p. 351-6.

[26] Agnew SR, Duygulu Ö. Plastic anisotropy and the role of non-basal slip in magnesium alloy AZ31B. International Journal of Plasticity. 2005;21:1161-93.

[27] Wu Z, Curtin W. The origins of high hardening and low ductility in magnesium. Nature. 2015;526:62.

[28] Kim K-H, Jeon JB, Kim NJ, Lee B-J. Role of yttrium in activation of< c+ a> slip in magnesium: An atomistic approach. Scripta Materialia. 2015;108:104-8.

[29] Yoo M, Agnew S, Morris J, Ho K. Non-basal slip systems in HCP metals and alloys: source mechanisms. Materials Science and Engineering: A. 2001;319:87-92.

[30] Christian JW, Mahajan S. Deformation twinning. Progress in Materials Science. 1995;39:1-157.

[31] Barnett M. Twinning and the ductility of magnesium alloys: Part I:"Tension" twins. Materials Science and Engineering: A. 2007;464:1-7.

[32] Barnett M. Twinning and the ductility of magnesium alloys: Part II."Contraction" twins. Materials Science and Engineering: A. 2007;464:8-16.

[33] El Kadiri H, Barrett CD, Wang J, Tomé CN. Why are twins profuse in magnesium? Acta Materialia. 2015;85:354-61.

[34] Khosravani A, Fullwood D, Adams B, Rampton T, Miles M, Mishra R. Nucleation and propagation of twins in AZ31 magnesium alloy. Acta Materialia. 2015;100:202-14.

[35] Barnett M. Twinning and the ductility of magnesium alloys: Part I:"Tension" twins. Materials Science and Engineering: A. 2007;464:1-7.

[36] Jiang J, Godfrey A, Liu W, Liu Q. Identification and analysis of twinning variants during compression of a Mg–Al–Zn alloy. Scripta Materialia. 2008;58:122-5.

[37] Barnett M. Twinning and the ductility of magnesium alloys: Part II."Contraction" twins. Materials Science and Engineering: A. 2007;464:8-16.

[38] Yi S, Bohlen J, Heinemann F, Letzig D. Mechanical anisotropy and deep drawing behaviour of AZ31 and ZE10 magnesium alloy sheets. Acta Materialia. 2010;58:592-605.

[39] Graff S, Brocks W, Steglich D. Yielding of magnesium: From single crystal to polycrystalline aggregates. International Journal of Plasticity. 2007;23:1957-78.

[40] Park SH, Lee JH, Moon BG, You BS. Tension–compression yield asymmetry in as-cast magnesium alloy. Journal of Alloys and Compounds. 2014;617:277-80.

[41] Friedrich H, Schumann S. Research for a "new age of magnesium" in the automotive industry. Journal of Materials Processing Technology. 2001;117:276-81.

[42] Wu Z, Ahmad R, Yin B, Sandlöbes S, Curtin W. Mechanistic origin and prediction of enhanced ductility in magnesium alloys. Science. 2018;359:447-52.

[43] Trang T, Zhang J, Kim J, Zargaran A, Hwang J, Suh B-C, et al. Designing a magnesium alloy with high strength and high formability. Nature communications. 2018;9:2522.

[44] Wu G, Chan K-C, Zhu L, Sun L, Lu J. Dual-phase nanostructuring as a route to high-strength magnesium alloys. Nature. 2017;545:80.

[45] Stanford N, Barnett M. The origin of "rare earth" texture development in extruded Mg-based alloys and its effect on tensile ductility. Materials Science and Engineering: A. 2008;496:399-408.

[46] Mukai T, Yamanoi M, Watanabe H, Higashi K. Ductility enhancement in AZ31 magnesium alloy by controlling its grain structure. Scripta Materialia. 2001;45:89-94.

[47] Chen L, Yuan F, Jiang P, Xie J, Wu X. Mechanical properties and deformation mechanism of Mg-Al-Zn alloy with gradient microstructure in grain size and orientation. Materials Science and Engineering: A. 2017;694:98-109.

[48] Amanov A, Penkov OV, Pyun Y-S, Kim D-E. Effects of ultrasonic nanocrystalline surface modification on the tribological properties of AZ91D magnesium alloy. Tribology international. 2012;54:106-13.

[49] Homma T, Kunito N, Kamado S. Fabrication of extraordinary high-strength magnesium alloy by hot extrusion. Scripta Materialia. 2009;61:644-7.

[50] Chen W, Zhang W, Qiao Y, Miao Q, Wang E. Enhanced ductility in high-strength fine-grained magnesium and magnesium alloy sheets processed via multi-pass rolling with lowered temperature. Journal of Alloys and Compounds. 2016;665:13-20.

[51] Ding K, Ye L. Laser shock peening: performance and process simulation: Woodhead Publishing; 2006.

[52] Telang A, Gill A, Mannava S, Vasudevan VK, Qian D, Teysseyre SP. Effects of Laser Shock Peening on SCC Behavior Of Alloy 600. Idaho National Laboratory (INL); 2013.

[53] Montross CS, Wei T, Ye L, Clark G, Mai Y-W. Laser shock processing and its effects on microstructure and properties of metal alloys: a review. International Journal of Fatigue. 2002;24:1021-36.

[54] Zhang R, Hou X, Zhou X, Gao H, Mankoci S, Qin H, et al. Effects of Laser Shock Peening on the Wear and Degradation Behaviors of Magnesium Alloys. ASME 2016 11th International Manufacturing Science and Engineering Conference: American Society of Mechanical Engineers; 2016. p. V002T01A5-VT01A5.

[55] Caralapatti VK, Narayanswamy S. Effect of high repetition laser shock peening on biocompatibility and corrosion resistance of magnesium. Optics & Laser Technology. 2017;88:75-84.

[56] Ge M-Z, Xiang J-Y. Effect of laser shock peening on microstructure and fatigue crack growth rate of AZ31B magnesium alloy. Journal of Alloys and Compounds. 2016;680:544-52.

[57] Li X, Zhang Y, Chen J, Lu Y. Effect of laser shock processing on stress corrosion cracking behaviour of AZ31 magnesium alloy at slow strain rate. Materials Science and Technology. 2013;29:626-30.

[58] Ge M-Z, Xiang J-Y, Yang L, Wang J. Effect of laser shock peening on the stress corrosion cracking of AZ31B magnesium alloy in a simulated body fluid. Surface and Coatings Technology. 2017;310:157-65.

[59] Sealy M, Guo Y, Caslaru R, Sharkins J, Feldman D. Fatigue performance of biodegradable magnesium–calcium alloy processed by laser shock peening for orthopedic implants. International Journal of Fatigue. 2016;82:428-36.

[60] Liao Y, Suslov S, Ye C, Cheng GJ. The mechanisms of thermal engineered laser shock peening for enhanced fatigue performance. Acta Materialia. 2012;60:4997-5009.

[61] Ding H, Shin YC. Dislocation density-based modeling of subsurface grain refinement with laser-induced shock compression. Computational Materials Science. 2012;53:79-88.

[62] Claverie A, Deroy J, Boustie M, Avrillaud G, Chuvatin A, Mazanchenko E, et al. Experimental characterization of plasma formation and shockwave propagation induced by high power pulsed underwater electrical discharge. Review of Scientific Instruments. 2014;85:063701.

[63] Mao B, Siddaiah A, Menezes PL, Liao Y. Surface texturing by indirect laser shock surface patterning for manipulated friction coefficient. Journal of Materials Processing Technology. 2018;257:227-33.

[64] Siddaiah A, Mao B, Liao Y, Menezes PL. Surface characterization and tribological performance of laser shock peened steel surfaces. Surface and Coatings Technology. 2018;351:188-97.

[65] Ye C, Suslov S, Lin D, Cheng GJ. Deformation-induced martensite and nanotwins by cryogenic laser shock peening of AISI 304 stainless steel and the effects on mechanical properties. Philosophical Magazine. 2012;92:1369-89.

[66] Trdan U, Skarba M, Grum J. Laser shock peening effect on the dislocation transitions and grain refinement of Al–Mg–Si alloy. Materials Characterization. 2014;97:57-68.

[67] Fei X, Grummon DS, Ye C, Cheng GJ, Cheng Y-T. Surface form memory in NiTi shape memory alloys by laser shock indentation. Journal of Materials Science. 2012;47:2088-94.

[68] Halilovič M, Issa S, Wallin M, Hallberg H, Ristinmaa M. Prediction of the residual state in 304 austenitic steel after laser shock peening–Effects of plastic deformation and martensitic phase transformation. International Journal of Mechanical Sciences. 2016;111:24-34.

[69] Lu J, Luo K, Zhang Y, Cui C, Sun G, Zhou J, et al. Grain refinement of LY2 aluminum alloy induced by ultra-high plastic strain during multiple laser shock processing impacts. Acta Materialia. 2010;58:3984-94.

[70] Ye C, Suslov S, Fei X, Cheng GJ. Bimodal nanocrystallization of NiTi shape memory alloy by laser shock peening and post-deformation annealing. Acta Materialia. 2011;59:7219-27.

[71] Lu J, Luo K, Zhang Y, Sun G, Gu Y, Zhou J, et al. Grain refinement mechanism of multiple laser shock processing impacts on ANSI 304 stainless steel. Acta Materialia. 2010;58:5354-62.

[72] Zhang Y, Lu J, Ren X, Yao H, Yao H. Effect of laser shock processing on the mechanical properties and fatigue lives of the turbojet engine blades manufactured by LY2 aluminum alloy. Materials & Design. 2009;30:1697-703.

[73] Lu J, Zhang L, Feng A, Jiang Y, Cheng G. Effects of laser shock processing on mechanical properties of Fe–Ni alloy. Materials & Design. 2009;30:3673-8.

[74] Kumar MA, Kanjarla A, Niezgoda S, Lebensohn R, Tomé C. Numerical study of the stress state of a deformation twin in magnesium. Acta Materialia. 2015;84:349-58.

[75] Robson J, Stanford N, Barnett M. Effect of precipitate shape on slip and twinning in magnesium alloys. Acta Materialia. 2011;59:1945-56.

[76] Nayyeri G, Poole W, Sinclair C, Zaefferer S. Measurement of the critical resolved shear stress for basal slip in magnesium alloys using instrumented indentation. Scripta Materialia. 2018;156:37-41.

[77] Bhattacharya B, Niewczas M. Work-hardening behaviour of Mg single crystals oriented for basal slip. Philosophical Magazine. 2011;91:2227-47.

[78] Chapuis A, Driver JH. Temperature dependency of slip and twinning in plane strain compressed magnesium single crystals. Acta Materialia. 2011;59:1986-94.

[79] Burke E, Hibbard W. Plastic deformation of magnesium single crystals. JOM Journal of the Minerals Metals and Materials Society. 1952;4:295-303.

[80] Obara T, Yoshinga H, Morozumi S. $\{11\bar{2}2\}<\bar{1}123>$ Slip system in magnesium. Acta Metallurgica. 1973;21:845-53.

[81] Bilby BA, Crocker A. The theory of the crystallography of deformation twinning. Proceedings of the Royal Society of London Series A Mathematical and Physical Sciences. 1965;288:240-55.

[82] Herrera-Solaz V, Hidalgo-Manrique P, Pérez-Prado MT, Letzig D, Llorca J, Segurado J. Effect of rare earth additions on the critical resolved shear stresses of magnesium alloys. Materials Letters. 2014;128:199-203.

[83] Thompson N, Millard D. XXXVIII. Twin formation, in cadmium. The London, Edinburgh, and Dublin Philosophical Magazine and Journal of Science. 1952;43:422-40.

[84] Li B, El Kadiri H, Zhang X, Mathaudhu S, Ma Q. Structural Origin of Reversible Twinning, Non-Schmid Effect, Incoherent Twin Boundaries and Texture in Hexagonal Close-Packed Metals. Magnesium Technology 2012: Springer; 2012. p. 105-10.

[85] Zhang X, Li B, Wu X, Zhu Y, Ma Q, Liu Q, et al. Twin boundaries showing very large deviations from the twinning plane. Scripta Materialia. 2012;67:862-5.

[86] Gharghouri M, Weatherly G, Embury J. The interaction of twins and precipitates in a Mg-7.7 at.% Al alloy. Philosophical Magazine A. 1998;78:1137-49.

[87] Barnett M, Keshavarz Z, Beer A, Ma X. Non-Schmid behaviour during secondary twinning in a polycrystalline magnesium alloy. Acta Materialia. 2008;56:5-15.

[88] Cáceres C, Sumitomo T, Veidt M. Pseudoelastic behaviour of cast magnesium AZ91 alloy under cyclic loading–unloading. Acta Materialia. 2003;51:6211-8.

[89] Li B, Ma E. Atomic shuffling dominated mechanism for deformation twinning in magnesium. Physical Review Letters. 2009;103:035503.

[90] Li B, Zhang X. Twinning with zero twinning shear. Scripta Materialia. 2016;125:73-9.

[91] Nguyen N-T, Seo OS, Lee CA, Lee M-G, Kim J-h, Kim HY. Mechanical behavior of AZ31B Mg alloy sheets under monotonic and cyclic loadings at room and moderately elevated temperatures. Materials. 2014;7:1271-95.

[92] Yukutake E, Kaneko J, Sugamata M. Anisotropy and non-uniformity in plastic behavior of AZ31 magnesium alloy plates. Materials Transactions. 2003;44:452-7.

[93] Barrett CD, Imandoust A, Oppedal AL, Inal K, Tschopp MA, El Kadiri H. Effect of grain boundaries on texture formation during dynamic recrystallization of magnesium alloys. Acta Materialia. 2017;128:270-83.

[94] Zhang X, Cheng Y. Tensile anisotropy of AZ91 magnesium alloy by equal channel angular processing. Journal of Alloys and Compounds. 2015;622:1105-9.

[95] Park SH, Kim S-H, Yu H, Kim HS, You BS. Anisotropic compressive behavior of extruded Mg alloy plates with different width–thickness ratios. Materials Science and Engineering: A. 2016;675:11-8.

[96] Park SH, Hong S-G, Bang W, Lee CS. Effect of anisotropy on the low-cycle fatigue behavior of rolled AZ31 magnesium alloy. Materials Science and Engineering: A. 2010;527:417-23.

[97] Ahn K, Seo M-H. Effect of anisotropy and differential work hardening on the failure prediction of AZ31B magnesium sheet at room temperature. International Journal of Solids and Structures. 2018;138:181-92.

[98] Wang Y, Culbertson D, Jiang Y. An experimental study of anisotropic fatigue behavior of rolled AZ31B magnesium alloy. Materials & Design. 2020;186:108266.

[99] Mao B, Zhang X, Menezes PL, Liao Y. Anisotropic microstructure evolution of an AZ31B magnesium alloy subjected to dry sliding and its effects on friction and wear performance. Materialia. 2019;8:100444.

[100] Zhang X, Mao B, Siddaiah A, Menezes PL, Liao Y. Direct laser shock surface patterning of an AZ31B magnesium alloy: Microstructure evolution and friction performance. Journal of Materials Processing Technology. 2020;275:116333.

[101] Foley D, Al-Maharbi M, Hartwig K, Karaman I, Kecskes L, Mathaudhu S. Grain refinement vs. crystallographic texture: Mechanical anisotropy in a magnesium alloy. Scripta Materialia. 2011;64:193-6.

[102] Xiong Y, Jiang, Y. Cyclic deformation and fatigue of rolled AZ80 magnesium alloy along different material orientations. Materials Science and Engineering A. 2016;677:58-67.

[103] Guo X, Chapuis A, Wu P, Agnew S. On twinning and anisotropy in rolled Mg alloy AZ31 under uniaxial compression. International Journal of Solids and Structures. 2015;64:42-50.

[104] Blau PJ, Walukas M. Sliding friction and wear of magnesium alloy AZ91D produced by two different methods. Tribology international. 2000;33:573-9.

[105] Zeng R, Dietzel W, Witte F, Hort N, Blawert C. Progress and challenge for magnesium alloys as biomaterials. Advanced Engineering Materials. 2008;10:B3-B14.

[106] Taltavull C, Torres B, Lopez A, Rams J. Dry sliding wear behavior of AM60B magnesium alloy. Wear. 2013;301:615-25.

[107] Yu L, Cao J, Cheng Y. An improvement of the wear and corrosion resistances of AZ31 magnesium alloy by plasma electrolytic oxidation in a silicate–hexametaphosphate electrolyte with the suspension of SiC nanoparticles. Surface and Coatings Technology. 2015;276:266-78.

[108] Yang Y, Wu H. Improving the wear resistance of AZ91D magnesium alloys by laser cladding with Al–Si powders. Materials Letters. 2009;63:19-21.

[109] Sun H, Shi Y-N, Zhang M-X. Wear behaviour of AZ91D magnesium alloy with a nanocrystalline surface layer. Surface and Coatings Technology. 2008;202:2859-64.

[110] Doege E, Dröder K. Sheet metal forming of magnesium wrought alloys—formability and process technology. Journal of Materials Processing Technology. 2001;115:14-9.

[111] Chino Y, Kado M, Mabuchi M. Enhancement of tensile ductility and stretch formability of magnesium by addition of 0.2 wt%(0.035 at%) Ce. Materials Science and Engineering: A. 2008;494:343-9.

[112] Wu D, Chen R, Han E. Excellent room-temperature ductility and formability of rolled Mg–Gd–Zn alloy sheets. Journal of Alloys and Compounds. 2011;509:2856-63.

[113] Chino Y, Sassa K, Mabuchi M. Texture and stretch formability of a rolled Mg–Zn alloy containing dilute content of Y. Materials Science and Engineering: A. 2009;513:394-400.

[114] Masoudpanah S, Mahmudi R. Effects of rare-earth elements and Ca additions on the microstructure and mechanical properties of AZ31 magnesium alloy processed by ECAP. Materials Science and Engineering: A. 2009;526:22-30.

[115] Stanford N, Atwell D, Beer A, Davies C, Barnett M. Effect of microalloying with rare-earth elements on the texture of extruded magnesium-based alloys. Scripta Materialia. 2008;59:772-5.

[116] Hantzsche K, Bohlen J, Wendt J, Kainer K, Yi S, Letzig D. Effect of rare earth additions on microstructure and texture development of magnesium alloy sheets. Scripta Materialia. 2010;63:725-30.

[117] Sandlöbes S, Friák M, Korte-Kerzel S, Pei Z, Neugebauer J, Raabe D. A rare-earth free magnesium alloy with improved intrinsic ductility. Scientific Reports. 2017;7:10458.

[118] Song B, Xin R, Liao A, Yu W, Liu Q. Enhancing stretch formability of rolled Mg sheets by pre-inducing contraction twins and recrystallization annealing. Materials Science and Engineering: A. 2015;627:369-73.

[119] Huang X, Suzuki K, Chino Y, Mabuchi M. Improvement of stretch formability of Mg–3Al–1Zn alloy sheet by high temperature rolling at finishing pass. Journal of Alloys and Compounds. 2011;509:7579-84.

[120] Huang X, Suzuki K, Watazu A, Shigematsu I, Saito N. Improvement of formability of Mg–Al–Zn alloy sheet at low temperatures using differential speed rolling. Journal of Alloys and Compounds. 2009;470:263-8.

[121] Li X, Wang F, Li X, Tang G, Zhu J. Improvement of formability of Mg–3Al–1Zn alloy strip by electroplastic-differential speed rolling. Materials Science and Engineering: A. 2014;618:500-4.

[122] Huo Q, Yang X, Sun H, Li B, Qin J, Wang J, et al. Enhancement of tensile ductility and stretch formability of AZ31 magnesium alloy sheet processed by cross-wavy bending. Journal of Alloys and Compounds. 2013;581:230-5.

[123] Suh J, Victoria-Hernández J, Letzig D, Golle R, Volk W. Enhanced mechanical behavior and reduced mechanical anisotropy of AZ31 Mg alloy sheet processed by ECAP. Materials Science and Engineering: A. 2016;650:523-9.

[124] Miller VM, Berman TD, Beyerlein IJ, Jones JW, Pollock TM. Prediction of the plastic anisotropy of magnesium alloys with synthetic textures and implications for the effect of texture on formability. Materials Science and Engineering: A. 2016;675:345-60.

[125] Zeng Z, Nie J-F, Xu S-W, H. J. Davies C, Birbilis N. Super-formable pure magnesium at room temperature. Nature Communications. 2017;8:972.

[126] Zeng Z, Nie J-F, Xu S-W, Davies C, Birbilis N. Super-formable pure magnesium at room temperature. Nature communications. 2017;8:972.

[127] Cottam R, Robson J, Lorimer G, Davis B. Dynamic recrystallization of Mg and Mg–Y alloys: crystallographic texture development. Materials Science and Engineering: A. 2008;485:375-82.

[128] Mohri T, Mabuchi M, Nakamura M, Asahina T, Iwasaki H, Aizawa T, et al. Microstructural evolution and superplasticity of rolled Mg-9Al-1Zn. Materials Science and Engineering: A. 2000;290:139-44.

[129] Al-Samman T, Gottstein G. Dynamic recrystallization during high temperature deformation of magnesium. Materials Science and Engineering: A. 2008;490:411-20.

[130] Watanabe H, Tsutsui H, Mukai T, Ishikawa K, Okanda Y, Kohzu M, et al. Grain size control of commercial wrought Mg-Al-Zn alloys utilizing dynamic recrystallization. Materials transactions. 2001;42:1200-5.

[131] Kaibyshev R, Shipilova K, Musin F, Motohashi Y. Continuous dynamic recrystallization in an Al–Li–Mg–Sc alloy during equal-channel angular extrusion. Materials Science and Engineering: A. 2005;396:341-51.

[132] Del Valle J, Ruano O. Influence of texture on dynamic recrystallization and deformation mechanisms in rolled or ECAPed AZ31 magnesium alloy. Materials Science and Engineering: A. 2008;487:473-80.

[133] Fatemi-Varzaneh S, Zarei-Hanzaki A, Cabrera J, Calvillo P. EBSD characterization of repetitive grain refinement in AZ31 magnesium alloy. Materials Chemistry and Physics. 2015;149:339-43.

[134] Zhu S, Yan H, Liao X, Moody S, Sha G, Wu Y, et al. Mechanisms for enhanced plasticity in magnesium alloys. Acta Materialia. 2015;82:344-55.

[135] Martin É, Jonas JJ. Evolution of microstructure and microtexture during the hot deformation of Mg–3% Al. Acta Materialia. 2010;58:4253-66.

[136] Galiyev A, Kaibyshev R, Gottstein G. Correlation of plastic deformation and dynamic recrystallization in magnesium alloy ZK60. Acta Materialia. 2001;49:1199-207.

[137] Sun D, Chang C, Kao P. Microstructural aspects of grain boundary bulge in a dynamically recrystallized Mg-Al-Zn alloy. Metallurgical and Materials Transactions A. 2010;41:1864-70.

[138] Ma Q, Li B, Marin E, Horstemeyer S. Twinning-induced dynamic recrystallization in a magnesium alloy extruded at 450 C. Scripta Materialia. 2011;65:823-6.

[139] Biswas S, Dhinwal SS, Suwas S. Room-temperature equal channel angular extrusion of pure magnesium. Acta Materialia. 2010;58:3247-61.

[140] Zuo D, Li T, Liang W, Wen X, Yang F. Microstructures and mechanical behavior of magnesium processed by ECAP at ice-water temperature. Journal of Physics D: Applied Physics. 2018;51:185302.

[141] Wang L, Mostaed E, Cao X, Huang G, Fabrizi A, Bonollo F, et al. Effects of texture and grain size on mechanical properties of AZ80 magnesium alloys at lower temperatures. Materials & Design. 2016;89:1-8.

[142] Chen M-S, Yuan W-Q, Li H-B, Zou Z-H. Modeling and simulation of dynamic recrystallization behaviors of magnesium alloy AZ31B using cellular automaton method. Computational Materials Science. 2017;136:163-72.

[143] Gao P, Zhu S, An X, Xu S, Ruan D, Chen C, et al. Effect of sample orientation and initial microstructures on the dynamic recrystallization of a Magnesium alloy. Materials Science and Engineering: A. 2017;691:150-4.

[144] Fatemi-Varzaneh S, Zarei-Hanzaki A, Beladi H. Dynamic recrystallization in AZ31 magnesium alloy. Materials Science and Engineering: A. 2007;456:52-7.

[145] Ge M-Z, Xiang J-Y, Fan Z, Lu Y, Lei W. Effect of laser energy on microstructure of Mg-3Al-1Zn alloy treated by LSP. Journal of Alloys and Compounds. 2018;734:266-74.

[146] Luo K, Liu B, Wu L, Yan Z, Lu J. Tensile properties, residual stress distribution and grain arrangement as a function of sheet thickness of Mg–Al–Mn alloy subjected to two-sided and simultaneous LSP impacts. Applied Surface Science. 2016;369:366-76.

[147] Zhang F, Hao M, Wang F, Tan C, Yu X, Ma H, et al. Role of {10–12} twinning and detwinning in the shock-hardening behavior of rolled Mg–3Al–1Zn alloy. Scripta Materialia. 2012;67:951-4.

[148] Mao B, Liao Y, Li B. Gradient twinning microstructure generated by laser shock peening in an AZ31B magnesium alloy. Applied Surface Science. 2018;457:342-51.

[149] Fabbro R, Fournier J, Ballard P, Devaux D, Virmont J. Physical study of laser‐produced plasma in confined geometry. Journal of Applied Physics. 1990;68:775-84.

[150] Marsh SP. LASL shock Hugoniot data: Univ of California Press; 1980.

[151] Cao Y. Ablation and plasma effects during nanosecond laser matter interaction in air and water: PURDUE UNIVERSITY; 2015.

[152] Lloyd J, Clayton J, Becker R, McDowell D. Simulation of shock wave propagation in single crystal and polycrystalline aluminum. International Journal of Plasticity. 2014;60:118-44.

[153] Zhang Z, Gogos G. Theory of shock wave propagation during laser ablation. Physical Review B. 2004;69:235403.

[154] Zhang W, Yao YL. Micro scale laser shock processing of metallic components. Transactions-American Society of Mechanical Engineers Journal of Manufacturing Science and Engineering. 2002;124:369-78.

[155] Ren X, Yang X, Zhou W, Huang J, Ren Y, Wang C, et al. Thermal stability of surface nano-crystallization layer in AZ91D magnesium alloy induced by laser shock peening. Surface and Coatings Technology. 2017.

[156] Hong S-G, Park SH, Lee CS. Role of {10–12} twinning characteristics in the deformation behavior of a polycrystalline magnesium alloy. Acta Materialia. 2010;58:5873-85.

[157] Nie X, He W, Zhou L, Li Q, Wang X. Experiment investigation of laser shock peening on TC6 titanium alloy to improve high cycle fatigue performance. Materials Science and Engineering: A. 2014;594:161-7.

[158] Zhou L, Li Y, He W, He G, Nie X, Chen D, et al. Deforming TC6 titanium alloys at ultrahigh strain rates during multiple laser shock peening. Materials Science and Engineering: A. 2013;578:181-6.

[159] Doherty R, Hughes D, Humphreys F, Jonas J, Jensen DJ, Kassner M, et al. Current issues in recrystallization: a review. Materials Science and Engineering: A. 1997;238:219-74.

[160] Máthis K, Csiszár G, Čapek J, Gubicza J, Clausen B, Lukáš P, et al. Effect of the loading mode on the evolution of the deformation mechanisms in randomly textured magnesium polycrystals–Comparison of experimental and modeling results. International Journal of Plasticity. 2015;72:127-50.

[161] Tomé C, Lebensohn RA, Kocks U. A model for texture development dominated by deformation twinning: application to zirconium alloys. Acta metallurgica et materialia. 1991;39:2667-80.

[162] Fan H, Aubry S, Arsenlis A, El-Awady JA. The role of twinning deformation on the hardening response of polycrystalline magnesium from discrete dislocation dynamics simulations. Acta Materialia. 2015;92:126-39.

[163] Ghaderi A, Barnett MR. Sensitivity of deformation twinning to grain size in titanium and magnesium. Acta Materialia. 2011;59:7824-39.

[164] Mao B, Liao Y. Understanding the Laser-Matter Interaction and Plasma Dynamics in Nanosecond Pulsed Laser Shock Processing: A First Principle Study. International Manufacturing Science and Engineering Conference: American Society of Mechanical Engineers; 2019. p. V002T03A3.

[165] Knezevic M, Levinson A, Harris R, Mishra RK, Doherty RD, Kalidindi SR. Deformation twinning in AZ31: influence on strain hardening and texture evolution. Acta Materialia. 2010;58:6230-42.

[166] Dudamell N, Ulacia I, Gálvez F, Yi S, Bohlen J, Letzig D, et al. Twinning and grain subdivision during dynamic deformation of a Mg AZ31 sheet alloy at room temperature. Acta Materialia. 2011;59:6949-62.

[167] Tucker MT, Horstemeyer MF, Gullett PM, El Kadiri H, Whittington WR. Anisotropic effects on the strain rate dependence of a wrought magnesium alloy. Scripta Materialia. 2009;60:182-5.

[168] Stanford N, Sotoudeh K, Bate P. Deformation mechanisms and plastic anisotropy in magnesium alloy AZ31. Acta Materialia. 2011;59:4866-74.

[169] Niewczas M. Lattice correspondence during twinning in hexagonal close-packed crystals. Acta Materialia. 2010;58:5848-57.

[170] El Kadiri H, Kapil J, Oppedal A, Hector Jr L, Agnew SR, Cherkaoui M, et al. The effect of twin–twin interactions on the nucleation and propagation of $\{101^-2\}$ twinning in magnesium. Acta Materialia. 2013;61:3549-63.

[171] Shi D, Liu T, Hou D, Chen H, Pan F, Chen H. The effect of twin–twin interaction in Mg3Al1Zn alloy during compression. Journal of Alloys and Compounds. 2016;685:428-35.

[172] Mokdad F, Chen D, Li D. Single and double twin nucleation, growth, and interaction in an extruded magnesium alloy. Materials & Design. 2017;119:376-96.

[173] Morrow B, Cerreta E, McCabe R, Tomé C. Toward understanding twin–twin interactions in hcp metals: utilizing multiscale techniques to characterize deformation mechanisms in magnesium. Materials Science and Engineering: A. 2014;613:365-71.

[174] Yu Q, Wang J, Jiang Y, McCabe RJ, Li N, Tomé CN. Twin–twin interactions in magnesium. Acta Materialia. 2014;77:28-42.

[175] Chen H, Liu T, Xiang S, Liang Y. Abnormal migration of twin boundaries in rolled AZ31 alloy containing intersecting $\{101^-2\}$ extension twins. Journal of Alloys and Compounds. 2017;690:376-80.

[176] Gong M, Xu S, Jiang Y, Liu Y, Wang J. Structural Characteristics of $\{1^-012\}$ Non-cozone Twin-Twin Interactions in Magnesium. Acta Materialia. 2018.

[177] Dudamell N, Hidalgo-Manrique P, Chakkedath A, Chen Z, Boehlert C, Gálvez F, et al. Influence of strain rate on the twin and slip activity of a magnesium alloy containing neodymium. Materials Science and Engineering: A. 2013;583:220-31.

[178] Hazeli K, Kannan V, Kingstedt O, Ravichandran G, Ramesh K. Deformation twin nucleation and twin variant selection in single crystal magnesium as a function of strain rate. arXiv preprint arXiv:180110252. 2018.

[179] Wang M, Lu L, Li C, Xiao X, Zhou X, Zhu J, et al. Deformation and spallation of a magnesium alloy under high strain rate loading. Materials Science and Engineering: A. 2016;661:126-31.

[180] Ecault R, Berthe L, Touchard F, Boustie M, Lescoute E, Sollier A, et al. Experimental and numerical investigations of shock and shear wave propagation induced by femtosecond laser irradiation in epoxy resins. Journal of Physics D: Applied Physics. 2015;48:095501.

[181] Mao B, Liao Y, Li B. Twinning Behavior in Magnesium Alloys Processed by Laser Shock Peening. International Manufacturing Science and Engineering Conference: American Society of Mechanical Engineers; 2019. p. V002T03A69.

[182] Mao B, Liao Y, Li B. Abnormal twin-twin interaction in an Mg-3Al-1Zn magnesium alloy processed by laser shock peening. Scripta Materialia. 2019;165:89-93.

[183] Zeng X, Mao X, Mao SS, Wen S-B, Greif R, Russo RE. Laser-induced shockwave propagation from ablation in a cavity. Applied Physics Letters. 2006;88:061502.

[184] Song S, Gray III G. Structural interpretation of the nucleation and growth of deformation twins in Zr and Ti—I. Application of the coincidence site lattice (CSL) theory to twinning problems in hcp structures. Acta metallurgica et materialia. 1995;43:2325-37.

[185] Li B, Sui M, Li B, Ma E, Mao S. Reversible twinning in pure aluminum. Physical Review Letters. 2009;102:205504.

[186] Partridge P, Roberts E. The formation and behaviour of incoherent twin boundaries in hexagonal metals. Acta Metallurgica. 1964;12:1205-10.

[187] Molnár P, Jäger A, Lejček P. Twin nucleation at grain boundaries in Mg–3 wt.% Al–1 wt.% Zn alloy processed by equal channel angular pressing. Scripta Materialia. 2012;67:467-70.

[188] Wang J, Yadav S, Hirth J, Tomé C, Beyerlein I. Pure-shuffle nucleation of deformation twins in hexagonal-close-packed metals. Materials Research Letters. 2013;1:126-32.

[189] Cui Y, Li Y, Sun S, Bian H, Huang H, Wang Z, et al. Enhanced damping capacity of magnesium alloys by tensile twin boundaries. Scripta Materialia. 2015;101:8-11.

[190] Y Liu NL, S Shao, M Gong, J Wang, RJ McCabe, Y Jiang, CN Tomé. Characterizing the boundary lateral to the shear direction of deformation twins in magnesium. Nature communications. 2016;7.

[191] Zhang X, Li B, Sun Q. On the $101\bar{2}$ "twinning shear" measured from line deflection. Scripta Materialia. 2019;159:133-6.

[192] Jeong J, Alfreider M, Konetschnik R, Kiener D, Oh SH. In-situ TEM observation of $\{101\bar{2}\}$ twin-dominated deformation of Mg pillars: Twinning mechanism, size effects and rate dependency. Acta Materialia. 2018;158:407-21.

[193] Serra A, Bacon D. A new model for {10 1 2} twin growth in hcp metals. Philosophical Magazine A. 1996;73:333-43.

[194] Serra A, Bacon D. Computer simulation of twin boundaries in the hcp metals. Philosophical Magazine A. 1986;54:793-804.

[195] Li B, Ma E, Ramesh K. Dislocation configurations in an extruded ZK60 magnesium alloy. Metallurgical and Materials Transactions A. 2008;39:2607-14.

[196] Mokdad F, Chen D, Li D. Twin-twin interactions and contraction twin formation in an extruded magnesium alloy subjected to an alteration of compressive direction. Journal of Alloys and Compounds. 2018;737:549-60.

[197] Ogawa Y, Ando D, Sutou Y, Koike J. A lightweight shape-memory magnesium alloy. Science. 2016;353:368-70.

[198] Chen H, Alpas A. Sliding wear map for the magnesium alloy Mg-9Al-0.9 Zn (AZ91). Wear. 2000;246:106-16.

[199] Cai C, LingHui S, XingHao D, BaoLin W. Enhanced mechanical property of AZ31B magnesium alloy processed by multi-directional forging method. Materials Characterization. 2017.

[200] Zhang H, Huang G, Wang L, Roven HJ, Pan F. Enhanced mechanical properties of AZ31 magnesium alloy sheets processed by three-directional rolling. Journal of Alloys and Compounds. 2013;575:408-13.

[201] Mao B, Siddaiah A, Liao Y, Menezes PL. Laser surface texturing and related techniques for enhancing tribological performance of engineering materials: A review. Journal of Manufacturing Processes. 2020;53:153-73.

[202] An J, Li R, Lu Y, Chen C, Xu Y, Chen X, et al. Dry sliding wear behavior of magnesium alloys. Wear. 2008;265:97-104.

[203] Ramanathan S. Dry sliding wear behavior of as-cast ZE41A magnesium alloy. Materials & Design. 2010;31:1930-6.

[204] Taltavull C, Rodrigo P, Torres B, López A, Rams J. Dry sliding wear behavior of AM50B magnesium alloy. Materials & Design. 2014;56:549-56.

[205] Itoi T, Gonda K, Hirohashi M. Relationship of wear properties to basal-plane texture of worn surface of Mg alloys. Wear. 2011;270:606-12.

[206] Liu Y, Jin B, Li D-J, Zeng X-Q, Lu J. Wear behavior of nanocrystalline structured magnesium alloy induced by surface mechanical attrition treatment. Surface and Coatings Technology. 2015;261:219-26.

[207] Wang S, Yang Z, Zhao Y, Wei M. Sliding wear characteristics of AZ91D alloy at ambient temperatures of 25–200 C. Tribology letters. 2010;38:39-45.

[208] Liang C, Li C, Lv X, An J. Correlation between friction-induced microstructural evolution, strain hardening in subsurface and tribological properties of AZ31 magnesium alloy. Wear. 2014;312:29-39.

[209] Guo N, Song B, Guo C, Xin R, Liu Q. Improving tensile and compressive properties of magnesium alloy rods via a simple pre-torsion deformation. Materials & Design. 2015;83:270-5.

[210] Song B, Guo N, Liu T, Yang Q. Improvement of formability and mechanical properties of magnesium alloys via pre-twinning: A review. Materials & Design (1980-2015). 2014;62:352-60.

[211] Mao B, Siddaiah A, Zhang X, Li B, Menezes PL, Liao Y. The influence of surface pre-twinning on the friction and wear performance of an AZ31B Mg alloy. Applied Surface Science. 2019;480:998-1007.

[212] Ren X, Huang J, Zhou W, Xu S, Liu F. Surface nano-crystallization of AZ91D magnesium alloy induced by laser shock processing. Materials & Design. 2015;86:421-6.

[213] Lou S, Li Y, Zhou L, Nie X, He G, He W. Surface nanocrystallization of metallic alloys with different stacking fault energy induced by laser shock processing. Materials & Design. 2016;104:320-6.

[214] Livescu V, Cady CM, Cerreta EK, Henrie BL, Gray GT. The high strain rate deformation behavior of high purity magnesium and AZ31B magnesium alloy. Essential Readings in Magnesium Technology: Springer; 2016. p. 375-80.

[215] Menezes PL, Kailas SV. Influence of surface texture and roughness parameters on friction and transfer layer formation during sliding of aluminium pin on steel plate. Wear. 2009;267:1534-49.

[216] Menezes PL, Kailas SV. Influence of surface texture on coefficient of friction and transfer layer formation during sliding of pure magnesium pin on 080 M40 (EN8) steel plate. Wear. 2006;261:578-91.

[217] Sahin M, Cetinarslan CS, Akata HE. Effect of surface roughness on friction coefficients during upsetting processes for different materials. Materials & design. 2007;28:633-40.

[218] Zhang Y, Wang K, Han Z, Liu G. Dry sliding wear behavior of copper with nano-scaled twins. Wear. 2007;262:1463-70.

[219] Wu P, Guo X, Qiao H, Agnew S, Lloyd D, Embury J. On the rapid hardening and exhaustion of twinning in magnesium alloy. Acta Materialia. 2017;122:369-77.

[220] Jahedi M, McWilliams BA, Moy P, Knezevic M. Deformation twinning in rolled WE43-T5 rare earth magnesium alloy: Influence on strain hardening and texture evolution. Acta Materialia. 2017;131:221-32.

[221] Mert F. Dry sliding wear behaviour of as-cast AZ31B magnesium alloy. Mechanics. 2017;23:728-34.

[222] Mao B, Siddaiah A, Menezes PL, Liao Y. A Novel Laser Shock Surface Patterning Process Toward Tribological Applications. International Manufacturing Science and Engineering Conference: American Society of Mechanical Engineers; 2019. p. V002T03A90.

[223] Siddaiah A, Mao B, Liao Y, Menezes PL. Effect of laser shock peening on the wear-corrosion synergistic behavior of AZ31B magnesium alloys. Journal of tribology. 2019:1-22.

[224] Archard J. Contact and rubbing of flat surfaces. Journal of Applied Physics. 1953;24:981-8.

[225] Tang Y, El-Awady JA. Formation and slip of pyramidal dislocations in hexagonal close-packed magnesium single crystals. Acta Materialia. 2014;71:319-32.

[226] Yoshinaga H, Horiuchi R. Deformation mechanisms in magnesium single crystals compressed in the direction parallel to hexagonal axis. Transactions of the Japan Institute of Metals. 1963;4:1-8.

[227] Mokhtar M. The effect of hardness on the frictional behaviour of metals. Wear. 1982;78:297-304.

[228] Challen J, Oxley P. An explanation of the different regimes of friction and wear using asperity deformation models. Wear. 1979;53:229-43.

[229] Zhang R, Zhou X, Gao H, Mankoci S, Liu Y, Sang X, et al. The effects of laser shock peening on the mechanical properties and biomedical behavior of AZ31B magnesium alloy. Surface and Coatings Technology. 2018;339:48-56.

[230] He W, Zeng Q, Yu H, Xin Y, Luan B, Liu Q. Improving the room temperature stretch formability of a Mg alloy thin sheet by pre-twinning. Materials Science and Engineering: A. 2016;655:1-8.

[231] Mao B, Li B, Lin D, Liao Y. Enhanced room temperature stretch formability of AZ31B magnesium alloy sheet by laser shock peening. Materials Science and Engineering: A. 2019;756:219-25.

[232] Zhang X, Mao B, Histed R, Liao Y. Modeling for Chemical-Etching Enhanced Pulsed Laser Ablation. International Manufacturing Science and Engineering Conference: American Society of Mechanical Engineers; 2019. p. V001T02A4.

[233] Fabbro R, Peyre P, Berthe L, Scherpereel X. Physics and applications of laser-shock processing. Journal of Laser Applications. 1998;10:265-79.

[234] Wang T, Jonas JJ, Yue S. Dynamic Recrystallization Behavior of a Coarse-Grained Mg-2Zn-2Nd Magnesium Alloy. Metallurgical and Materials Transactions A. 2017;48:594-600.

[235] Nadella RK, Samajdar I, Gottstein G. Static recrystallisation and textural changes in warm rolled pure magnesium. Magnesium: Proceedings of the 6th International Conference Magnesium Alloys and Their Applications: Wiley Online Library; 2003. p. 1052-7.

[236] Al-Samman T, Molodov KD, Molodov DA, Gottstein G, Suwas S. Softening and dynamic recrystallization in magnesium single crystals during c-axis compression. Acta Materialia. 2012;60:537-45.

[237] Jiang M, Xu C, Yan H, Lu S, Nakata T, Lao C, et al. Correlation between dynamic recrystallization and formation of rare earth texture in a Mg-Zn-Gd magnesium alloy during extrusion. Scientific Reports. 2018;8:16800.

[238] Liu Q, Song J, Pan F, She J, Zhang S, Peng P. The edge crack, texture evolution, and mechanical properties of Mg-1Al-1Sn-Mn alloy sheets prepared using on-line heating rolling. Metals. 2018;8:860.

[239] Pan F, Zeng B, Jiang B, Zhang M, Dong H. Enhanced mechanical properties of AZ31B magnesium alloy thin sheets processed by on-line heating rolling. Journal of Alloys and Compounds. 2017;693:414-20.

[240] Hyun C, Kim M, Choi S-H, Shin K. Crystal plasticity FEM study of twinning and slip in a Mg single crystal by Erichsen test. Acta Materialia. 2018;156:342-55.

[241] Mao B, Liao Y. Modeling of lüders elongation and work hardening behaviors of ferrite-pearlite dual phase steels under tension. Mechanics of Materials. 2019;129:222-9.

[242] Park SH, Hong S-G, Lee CS. Enhanced stretch formability of rolled Mg–3Al–1Zn alloy at room temperature by initial {10–12} twins. Materials Science and Engineering: A. 2013;578:271-6.

[243] Mao B, Zhang X, Liao Y, Li B. Improving Room Temperature-Stretch Formability of Magnesium Alloys by Laser Shock Peening. International Manufacturing Science and Engineering Conference: American Society of Mechanical Engineers 2019. p. V002T03A72.

[244] Koike J, Ohyama R, Kobayashi T, Suzuki M, Maruyama K. Grain-boundary sliding in AZ31 magnesium alloys at room temperature to 523 K. Materials Transactions. 2003;44:445-51.

[245] Orozco-Caballero A, Lunt D, Robson JD, da Fonseca JQ. How magnesium accommodates local deformation incompatibility: A high-resolution digital image correlation study. Acta Materialia. 2017;133:367-79.

[246] Kim W-J, Chung S, Chung C, Kum D. Superplasticity in thin magnesium alloy sheets and deformation mechanism maps for magnesium alloys at elevated temperatures. Acta Materialia. 2001;49:3337-45.

[247] Somekawa H, Singh A. Superior room temperature ductility of magnesium dilute binary alloy via grain boundary sliding. Scripta Materialia. 2018;150:26-30.

[248] Somekawa H, Basha DA, Singh A. Room temperature grain boundary sliding behavior of fine-grained Mg-Mn alloys. Materials Science and Engineering: A. 2018.

[249] Somekawa H, Kinoshita A, Washio K, Kato A. Enhancement of room temperature stretch formability via grain boundary sliding in magnesium alloy. Materials Science and Engineering: A. 2016;676:427-33.

[250] Yuan W, Panigrahi S, Su J-Q, Mishra R. Influence of grain size and texture on Hall–Petch relationship for a magnesium alloy. Scripta Materialia. 2011;65:994-7.

[251] Del Valle J, Carreño F, Ruano OA. Influence of texture and grain size on work hardening and ductility in magnesium-based alloys processed by ECAP and rolling. Acta Materialia. 2006;54:4247-59.

Journal Publications during Ph.D. study

1.   **Bo Mao**, Yiliang Liao, and Bin Li. "Abnormal twin-twin interaction in an Mg-3Al-1Zn magnesium alloy processed by laser shock peening." Scripta Materialia 165 (2019): 89-93.

2.   **Bo Mao**, Xing Zhang, Pradeep L. Menezes, and Yiliang Liao. "Anisotropic microstructure evolution of an AZ31B magnesium alloy subjected to dry sliding and its effects on friction and wear performance." Materialia 8 (2019): 100444.

3.   **Bo Mao**, Arpith Siddaiah, Xing Zhang, Bin Li, Pradeep L. Menezes, and Yiliang Liao. "The influence of surface pre-twinning on the friction and wear performance of an AZ31B Mg alloy." Applied Surface Science 480 (2019): 998-1007.

4.   **Bo Mao**, Yiliang Liao, and Bin Li. "Gradient twinning microstructure generated by laser shock peening in an AZ31B magnesium alloy." Applied Surface Science 457 (2018): 342-351.

5.   **Bo Mao**, Arpith Siddaiah, Pradeep L. Menezes, and Yiliang Liao. "Surface texturing by indirect laser shock surface patterning for manipulated friction coefficient." Journal of Materials Processing Technology 257 (2018): 227-233.

6.   **Bo Mao**, Bin Li, Dong Lin, and Yiliang Liao. "Enhanced room temperature stretch formability of AZ31B magnesium alloy sheet by laser shock peening." Materials Science and Engineering: A 756 (2019): 219-225.

7.   **Bo Mao** and Yiliang Liao. "Modeling of lüders elongation and work hardening behaviors of ferrite-pearlite dual phase steels under tension." Mechanics of Materials 129 (2019): 222-229.

8.   **Bo Mao**, Arpith Siddaiah, Yiliang Liao, and Pradeep L. Menezes. "Laser Surface Texturing and Related Techniques for Enhancing Tribological Performance of Engineering Materials: A Review." Journal of Manufacturing Processes 53 (2020) 153:173.

9.   Arpith Siddaiah, **Bo Mao**, Yiliang Liao, and Pradeep L. Menezes. "Surface characterization and tribological performance of laser shock peened steel surfaces." Surface and Coatings Technology 351 (2018): 188-197.

10.   Xing Zhang, **Bo Mao**, Arpith Siddaiah, Pradeep L. Menezes, and Yiliang Liao. "Direct laser shock surface patterning of an AZ31B magnesium alloy: Microstructure evolution and friction performance." Journal of Materials Processing Technology 275 (2020): 116333.

11.   Arpith Siddaiah, **Bo Mao**, Yiliang Liao, and Pradeep L. Menezes. "Effect of Laser Shock Peening on the Wear–Corrosion Synergistic Behavior of an AZ31B Magnesium Alloy." Journal of Tribology 142, no. 4 (2020).

12.   Xing Zhang, **Bo Mao**, Yiliang Liao, and Yufeng Zheng. "Selective laser melting of graphene oxide–reinforced Ti–48Al–2Cr–2Nb: Improved manufacturability and mechanical strength." Journal of Materials Research (2020):1-8.

13.   Xing Zhang, Christopher J. Yocom, **Bo Mao**, and Yiliang Liao. "Microstructure evolution during selective laser melting of metallic materials: A review." Journal of Laser Applications 31, no. 3 (2019): 031201.